Photocatalytic Reduction of CO₂ by Metal-Free-Based Materials: Recent Advances and Future Perspective

Huidong Shen, Tim Peppel,* Jennifer Strunk, and Zhenyu Sun*

Photocatalytic CO₂ reduction to produce valuable chemicals and fuels using solar energy provides an appealing route to alleviate global energy and environmental problems. Searching for photocatalysts with high activity and selectivity for CO₂ conversion is the key to achieving this goal. Among the various proposed photocatalysts, metal-free materials, such as graphene, nitrides, carbides, and conjugated organic polymers, have gained extensive research interest for photocatalytic CO₂ reduction, due to their earth abundance, cost-effectiveness, good electrical conductivity, and environmental friendliness. They exhibit prominent catalytic activity, impressive selectivity, and long durability for the conversion of CO₂ to solar fuels. Herein, the recent progress on metal-free photocatalysis of CO₂ reduction is systematically reviewed. Opportunities and challenges on modification of nonmetallic catalysts to enhance CO₂ transformation are presented. Theoretical calculations on possible reduction mechanisms and pathways as well as the potential in situ and operando techniques for mechanistic understanding are also summarized and discussed. Based on the aforementioned discussions, suitable future research directions and perspectives for the design and development of potential nonmetallic photocatalysts for efficient CO₂ reduction are provided.

1. Introduction

With the fast growth of population and industrialization, the demand for global energy has been increasing dramatically. It has been estimated that the global energy consumption will

increase by 28% in 2040.[1] Nearly 80% of the global energy demands are met by the burning of nonrenewable fossil fuels (coal, petroleum, natural gas, etc.).[2] The heavy dependence upon fossil fuels not only accelerates the depletion of the limited energy resources but also leads to a tremendous growth of carbon dioxide (CO₂) emissions in the atmosphere. Since the Industrial Revolution in 1750, the atmospheric level of CO₂ has rapidly risen from 280 ppm in 1750 to 415 ppm in 2019 (**Figure 1**).[4] It is the first time in human history that our planetary atmosphere has had more than 415 ppm CO₂.[4] This ever-growing anthropogenic CO₂ emissions are regarded as the main cause of the greenhouse gas effect (e.g., global warming, ice melting, and rise in sea level) and other environmental problems.[5–8] There exists a strong correlation between annual CO₂ concentration and air surface temperature of the earth and sea level from 1990 to 2100.[3,9,10] It is therefore imperative to lower the atmospheric CO₂ concentration.[11–13]

Currently, three main approaches can be adopted to reduce the amounts of CO₂ in the atmosphere, which includes 1) direct lowering of CO₂ emissions; 2) CO₂ capture and storage (CCS); and 3) CO₂ utilization and transformation.[14–16] Despite attempts to boost utilization efficiency of conventional fossil fuels, to substantially decrease CO₂ emissions is unrealistic due to the increasing energy requirements for high-quality life. The CCS strategy suffers from drawbacks such as leakage risk and compression and transportation cost, limiting its broad implementation.[17] Compared with CCS and direct reduction of CO₂ emissions, conversion into useful chemicals and fuels is more appealing, which can also ameliorate energy shortages and environmental issues. So far, several technologies have been utilized for transformation of CO₂ into hydrocarbon fuels or valuable compounds, including thermochemical,[18,19] biological,[20] photoelectrocatalytic,[21,22] electrocatalytic,[23–25] and photocatalytic reduction reactions.[26–30] Despite significant progress has been made, a number of challenges still exist. In particular, the design and fabrication of catalysts for selective and efficient conversion of CO₂ remains a focus of research interest in energy and environmental sciences.

Photochemical reduction of CO₂ with H₂O using solar light and semiconductor photocatalysts mimicking the natural photosynthesis process in plants can realize the potential scalable

H. Shen, Prof. Z. Sun
State Key Laboratory of Organic-Inorganic Composites
Beijing University of Chemical Technology
Beijing 100029, P. R. China
E-mail: sunzy@mail.buct.edu.cn

Dr. T. Peppel, Prof. J. Strunk
Leibniz Institute for Catalysis (LIKAT)
Heterogeneous Photocatalysis
Albert-Einstein-Str. 29a, Rostock 18059, Germany
E-mail: tim.peppel@catalysis.de

ⓘ The ORCID identification number(s) for the author(s) of this article can be found under https://doi.org/10.1002/solr.201900546.

production of so-called solar fuels (CH_3OH, C_2H_5OH, and hydrocarbons) at a satisfactory purity.[11,31,32] This protocol has been considered as one of the most promising, compelling, and challenging protocols to solve both global energy and environmental problems without releasing CO_2, associated with the following advantages: 1) the process can be achieved using inexhaustible and environmental-friendly solar energy; 2) the hydrocarbon fuels could be generated from water and CO_2 as the initial reactants; 3) it is mostly performed at ambient conditions (room temperature and atmospheric pressure); 4) this technology can convert the inert molecule into renewable solar fuels without inducing secondary pollution.[33,34] Therefore, photocatalytic CO_2 reduction would be likely killing two birds with one stone for solving the global energy and environmental problems simultaneously.

It is widely accepted that the design of appropriate photocatalysts plays a very important role in photocatalytic CO_2 conversion. Since the pioneering breakthrough on photocatalytic CO_2 conversion to HCOOH and CH_3OH using semiconductors by Inoue et al. in 1979,[35] a large number of attempts have been devoted to designing and developing active and robust photocatalysts to reduce CO_2. A variety of materials, such as titanium dioxides (TiO_2),[36–39] metal chalcogenides (ZnTe,[40] ZnS,[41] CdS,[42] MoS_2,[43] etc.), Bi-based semiconductors (Bi_2MoO_6,[44,45] Bi_2WO_6,[46] $BiVO_4$,[47] etc.), layered double hydroxides (LDHs),[48–50] inorganic perovskite halides ($CsPbBr_3$),[51–53] MXenes (Ti_3C_2),[54,55] and metal–organic frameworks (MOFs),[56–58] have been widely utilized as efficient catalysts. Although ever-growing metal-based catalysts have been applied for photocatalytic CO_2 conversion, a number of obvious drawbacks still exist, including their high prices, poor durability, low selectivity, and susceptibility to gas poisoning, which might preclude metal-based catalysts from large-scale applications.[59–61] Furthermore, the huge demand for most used metal-based catalysts results in the substantial decrease in global supplies. From the viewpoint of sustainability, it is urgent and meaningful to develop alternative metal-free catalysts.[62] Metal-free materials have the great potential as an alternative to metal-based catalysts due to their earth abundance, cost-effectiveness, high electronic conductivity, and environmental friendliness.[63–65] In addition, they exhibit prominent catalytic activity, remarkable selectivity, and reasonable durability for the transformation of CO_2 to solar fuels.

Although there are reviews on metal-free photocatalytic CO_2 conversion, only carbon-based materials, such as graphitic carbon nitride (g-C_3N_4), graphene and its derivatives are discussed.[66–70] A systematically comprehensive overview of nonmetallic catalysts in this field is still lacking. Here we provide such a review with major focus on the latest progress on metal-free photocatalysis of CO_2 reduction, including boron-containing materials (e.g., boron nitride (BN) and boron carbon nitride (BCN)), phosphorus-based materials (black phosphorus [BP] and red phosphorus), silicon carbide (SiC), covalent organic frameworks (COFs), and conjugated organic polymers (COPs), in addition to graphene and g-C_3N_4. Discussions are mainly concentrated on four aspects: 1) fundamentals of CO_2 reduction; 2) strategies to improve metal-free photocatalysis; 3) development of advanced in situ characterization techniques; 4) future prospects and challenges in photocatalytic CO_2 reduction by nonmetallic catalysts.

Huidong Shen obtained his master's degree in chemical technology from Yan'an University in 2017. Following this, he worked as assistant of Dean at Research Institute of Comprehensive Energy Industrial Technology. He is currently pursuing his Ph.D. at the College of Chemical Engineering, Beijing University of Chemical Technology (China) under the supervision of Prof. Zhenyu Sun. His current research focuses on controlled synthesis of Bi-based composite materials for photochemical reduction reactions.

Tim Peppel received his doctorate in inorganic chemistry from the University of Rostock (Germany) in 2010. In 2007, he was a visiting scholar at the North Carolina State University (NCSU) in Raleigh (USA) in the Department of Solid-State Chemistry. After a postdoctoral stay at the Leibniz Institute for Catalysis (LIKAT) in Rostock from 2011 until 2016 in the department of Heterogeneous Catalytic Processes (Inorganic Functional Materials), he became a senior scientist in the Department of Heterogeneous Photocatalysis at LIKAT in January 2017. His research interests include magnetic ionic liquids, oxygen storage materials as well as advanced materials for photocatalytic CO_2 reduction.
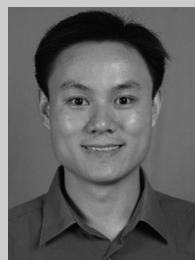
Zhenyu Sun completed his Ph.D. at the Institute of Chemistry Chinese Academy of Sciences in 2006. He carried out postdoctoral research at Trinity College Dublin (Ireland, 2006–2008), Ruhr University, Bochum (Germany, 2011–2014), and the University of Oxford (UK, 2014–2015). He is currently a full professor at the College of Chemical Engineering at Beijing University of Chemical Technology (China). His current research focuses on energy conversion reactions using 2D materials.

2. Theoretical Foundation of Photocatalytic CO_2 Reduction on Semiconductors

2.1. Basic Principles of CO_2 Photoreduction

Semiconductor materials are known to have a band structure with conduction band (CB) and valence band (VB).[71,72] Bandgap energy (E_g) is defined as the potential difference between the CB and VB (**Figure 2**a).[74] The bandgap and the CB/VB potential value determine the capability of a semiconductor to adsorb light and its photoreaction thermodynamics.[34] As shown in Figure 2b, photocatalytic CO_2 conversion usually
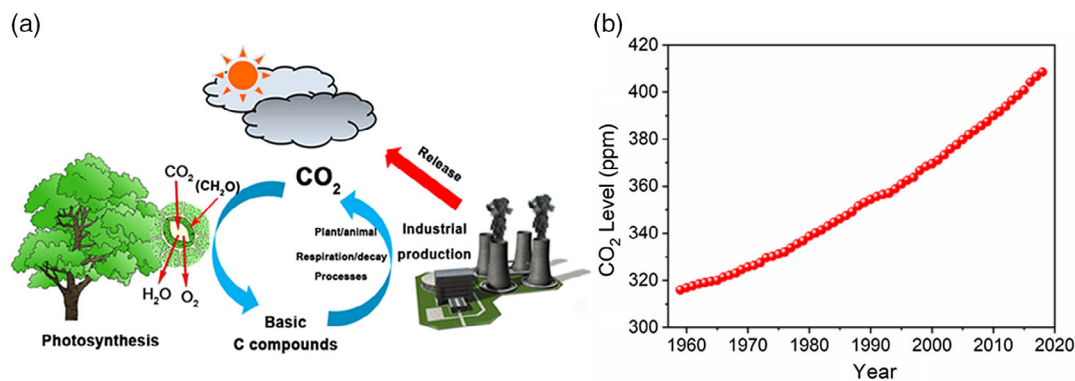
Figure 1. a) Illustration of an anthropogenic carbon cycle. b) Annual CO_2 levels between 1959 and 2018.[3]
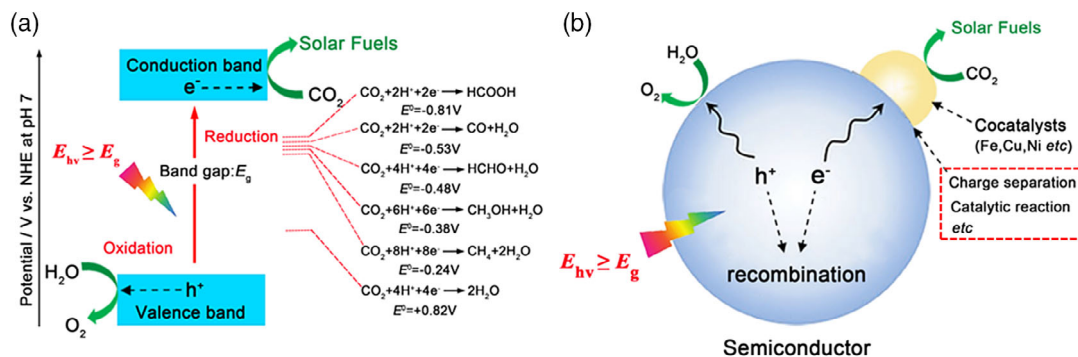

Figure 2. a) Schematic energy diagram for CO_2 reduction and H_2O oxidation on a semiconductor. b) Schematic of the overall photocatalytic reaction process, illustrating factors that may impact photocatalytic performance.[73]

involves three fundamental steps: 1) formation of electron–hole pairs upon absorption of photons ($E_{hv} \geq E_g$), 2) separation and transportation of charge carriers to the surface of a photocatalyst, 3) redox reaction between surface-adsorbed species and electron–hole pairs.[73,75] The process of photoreduction of CO_2 can be conducted in both gas phase and in solutions.[71]

CO_2 is highly thermodynamic and stable with a much higher C=O double-bond energy (750 kJ mol^{-1}) compared with C—H (411 kJ mol^{-1}), C—O (327 kJ mol^{-1}), and C—C (336 kJ mol^{-1}) single bonds.[71,76] Therefore, photoconversion of CO_2 into hydrocarbons usually requires high-energy inputs to activate the C=O bonds and transform them into, for example, C—H bonds. It has been reported that photogenerated electrons with a suitable reduction potential level can offer driving forces to reduce CO_2. The photocatalytic CO_2 reduction occurs via multi-step reaction pathways involving the participation of 2, 6, 8, or 12 electrons and protons.[77,78] Diverse products can be generated including C_1 compounds such as CO, CH_4, HCOOH, CH_3OH, HCHO, and C_2 molecules such as CH_2CH_2, C_2H_5OH, and CH_3COOH.[79] Some reactions associated with the CO_2 photoreduction, along with the corresponding reduction potentials (E^0) are listed in **Table 1** (Equation (2)–(11); CO_2 theoretical reduction potentials are provided relative to normal hydrogen electrode (NHE), at pH 7.0 in water).[80]

As shown in Table 1, the direct one-electron reduction of CO_2 is extremely difficult because of the strongly negative formal redox potential of up to −1.85 V.[81] Almost none of

Table 1. Electrochemical reactions involved in aqueous CO_2 reduction and proton reduction with their corresponding reduction potentials E^0 (V vs NHE at pH 7.0).

Entry	Equation	Product	E^0 (V)
1	$CO_2 + e^- \rightarrow CO_2^-$	Carbonate anion radical	−1.85
2	$CO_2 + 2\,H^+ + 2e^- \rightarrow HCOOH$	Formic acid	−0.61
3	$CO_2 + 2\,H^+ + 2e^- \rightarrow CO + H_2O$	Carbon monoxide	−0.53
4	$CO_2 + 4\,H^+ + 4e^- \rightarrow HCHO + H_2O$	Formaldehyde	−0.48
5	$CO_2 + 4\,H^+ + 4e^- \rightarrow C + 2H_2O$	Carbon	−0.20
6	$CO_2 + 6\,H^+ + 6e^- \rightarrow CH_3OH + H_2O$	Methanol	−0.38
7	$CO_2 + 8\,H^+ + 8e^- \rightarrow CH_4 + 2H_2O$	Methane	−0.24
8	$2CO_2 + 12\,H^+ + 12e^- \rightarrow C_2H_4 + 4H_2O$	Ethylene	−0.34
9	$2CO_2 + 12\,H^+ + 12e^- \rightarrow C_2H_5OH + 3H_2O$	Ethanol	−0.33
10	$2CO_2 + 14\,H^+ + 14e^- \rightarrow C_2H_6 + 4H_2O$	Ethane	−0.27
11	$3CO_2 + 18\,H^+ + 18e^- \rightarrow C_3H_7OH + 5H_2O$	Propanol	−0.32
12	$2\,H^+ + 2e^- \rightarrow H_2$	Hydrogen	−0.42

the photocatalysts so far have sufficient capabilities to drive such single-electron transfer (ET) processes. In contrast, the proton-assisted multi-electron/proton reduction is an alternative and more favorable route because of the significantly lower reduction potential required for CO_2 reduction. With this in mind, to design high-efficiency photocatalysts for CO_2 reduction, one

should consider several points: 1) multiple electrons and protons must easily generate and migrate from the semiconductor to CO_2; 2) photogenerated electrons at the CB edge should be more negative than the theoretical reduction potentials of both CO_2 and its reduced species; 3) reactants such as H_2O, CO_2, or carbonates in solution need to reach and be adsorbed on the active sites of a photocatalyst, and the product molecules such as CH_3OH and HCOOH need to diffuse away and desorb from the catalyst surface after the reduction; 4) the photoinduced holes on the VB of a photocatalyst need to be readily depleted by additional sacrificing reagents or H_2O.[34]

2.2. Adsorption and Activation of CO_2

CO_2 adsorption on a catalyst surface usually occurs along with its activation.[82,83] The activation of adsorbed CO_2 molecules is a crucial and very challenging step for CO_2 reduction. CO_2 adsorption and activation significantly affect subsequent reduction steps and suppression of the competing hydrogen evolution reaction (HER). The adsorption interaction with surface atoms is believed to result in a partially charged species $CO_2^{\delta-}$.[84] The possible adsorbed structures of CO_2 mainly include oxygen coordination, carbon coordination, and mixed coordination (**Figure 3**).[85] For oxygen coordination, each of the oxygen atoms in CO_2 can donate lone pairs of electrons to surface Lewis acid centers (Figure 3a). For carbon coordination, the carbon atom in CO_2 could also behave as a Lewis acid and acquire electrons from Lewis base sites, resulting in a carbonate-like structure (Figure 3b). In contrast, for mixed coordination, both oxygen atoms and carbon atoms in CO_2 act as an electron donor and acceptor at the same time, as shown in Figure 3c.

The evolution of adsorbed CO_2 species on the catalyst surface is recognized to be the rate-determining and selectivity-controlling step during photocatalytic CO_2 reduction. It requires a dramatic reorganizational energy to transform the linear CO_2 molecule into bent radical anion CO_2^-, which is determined by surface area, surface defect, and surface atomic construction.[86]
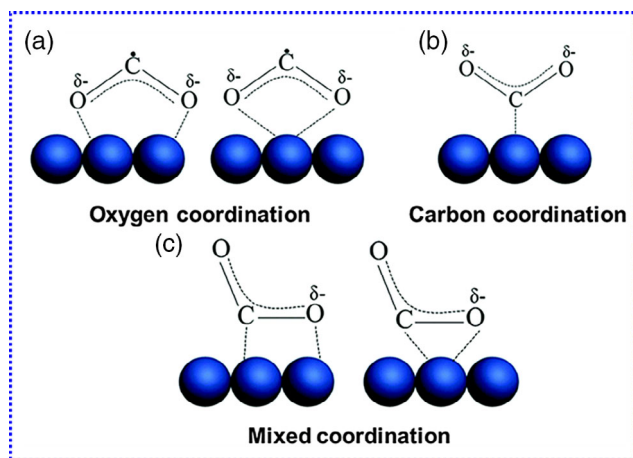
Creation of a higher surface area of a photocatalyst can accelerate mass transfer, improve CO_2 adsorption, and offer more catalytically active centers for CO_2 reduction. As such, a variety of nanostructured materials were developed to afford large surface areas, including zero-dimensional (0D) nanoparticles (NPs),[87] one-dimensional (1D) nanorods/nanotubes/nanowires,[88–90] two-dimensional (2D) nanosheets,[91,92] or three-dimensional (3D) hierarchical micro/nanostructures.[93] Alternatively, some porous and hollow materials with multichannels and large surface-to-volume ratios were also designed as photocatalysts for CO_2 conversion.[94]

Tuning surface defects of stoichiometric photocatalysts is another strategy to facilitate CO_2 adsorption and activation.[95,96] The surface defects (such as oxygen vacancies) are claimed to be the most reactive sites on the surfaces of semiconductors, which could profoundly alter the electronic and chemical properties of the catalysts.[33,97] The local charge density of photocatalyst is enhanced at surface defects, which favors strong interaction with CO_2 molecules, lowers the bond energy of CO_2 molecules, and accelerates the transport of photogenerated electrons to reactants.[98,99]

2.3. Proposed Reaction Pathways of CO_2 Reduction

CO_2 reduction is a complicated redox reaction process and involves simultaneous transfer of multiple electrons/protons, cleavage of C=O bond, and formation of C—H bond.[100] Different distributions of final products can be acquired dependent on reaction conditions. The intertwining of photooxidation and photoreduction reactions also complicates the CO_2 reduction process. CO_2 photoreduction is affected by many factors, including the composition and structure of photocatalyst, operation conditions (pH, temperature, pressure, reductant), and cocatalyst if any. Relevant analyses on these complexities have been provided in recent reviews.[7,85]

Three possible mechanisms are proposed for the photoreduction of CO_2. The CO_2 reduction can proceed via a formaldehyde route.[101] In this fast hydrogenation path, a proton usually first reacts with a $CO_2^{\bullet-}$ to yield HCOOH, followed by dehydration of the dihydroylmethyl intermediates to produce HCHO. HCHO is further reduced to generate CH_3OH and then CH_4. In the carbene pathway, a proton attacks a $CO_2^{\bullet-}$ to form CO by breaking the C—O bond.[102] Through a concerted electron and proton transfer, CO is reduced to a carbon residue which is then reduced to form a $C^{\bullet}$. By further accepting protons, the carbon radical can be subseqently reduced to $CH^{\bullet}$, $CH_3^{\bullet}$, and CH_4.[103] Reaction of $CH_3^{\bullet}$ and an $OH^{\bullet}$ leads to the formation of CH_3OH. These two routes encompass only reduction steps that involve the transfer of electrons and hydrogen atoms to produce different radical and nonradical intermediates. However, in an alternative glyoxal pathway, both reduction and oxidation steps are involved, following the sequence $CO_2^{\bullet-}$, $HC^{\bullet}O$, HOCCOH, $HOCH_2COH$, $HOCCH_2^{\bullet}$, $HOCCH_3$, $CH_3OC^{\bullet}$, $CH_3^{\bullet}$, and CH_4.[80,104] It should be pointed out that the reaction pathway is closely related to the adsorption mode of $CO_2^{\bullet-}$ on the surface of a photocatalyst. The exact reaction mechanism over nonmetallic semiconductors needs further elucidation.

Figure 3. a–c) Three adsorbed $CO_2^{\delta-}$ structures. Reproduced with permission.[85] Copyright 2016, Royal Society of Chemistry.

2.4. Competition of H$_2$ Evolution

Water seems to be an ideal reducing reagent for CO$_2$ photocatalysis because it can act as both electron donor and hydrogen source. However, proton reduction usually takes place, which is an undesirable parasitic reaction when performing CO$_2$ reduction in water. Compared with CO$_2$ reduction, proton reduction is a relatively more facile process in both thermodynamics and kinetics.[5,34] In thermodynamics, the theoretical proton reduction potential ($E^0 = 0$ V vs NHE) is more positive than CO$_2$ reduction potentials to CO, HCOOH, and HCHO. In kinetics, proton reduction to H$_2$ solely requires two electrons, which can occur much easier than the CO$_2$ reduction demanding multiple electrons (more than two electrons). Therefore, to boost CO$_2$ reduction efficiency, one must suppress electrons and holes to inhibit H$_2$ evolution prior to being transported to CO$_2$.[105]

2.5. Oxidation Half-Reaction

In parallel with CO$_2$ reduction, the oxidation of water to generate O$_2$ or hydroxyl radicals (OH$^\bullet$) occurs as the other half reaction, which consumes photoinduced holes to extend the existence of photoexcited electrons.[80,106] Sacrificial agents to donate electrons such as alcohols or amines are usually used. The oxidation potential of water to O$_2$ is $+0.81$ V (vs NHE), being less positive than the potential of the VB of most semiconductors, making the oxidation thermodynamically possible. However, the evolved strongly oxidizing OH$^\bullet$ or O$_2$ adsorbed on the semiconductor catalyst likely oxidizes CO$_2$-reduced intermediates and interrupts the process of CO$_2$ reduction. Therefore, to promote water oxidation and consequently CO$_2$ reduction, the removal of accumulated oxidation intermediates as well as enhancing hole mobility offers a feasible route.[107]

2.6. Product Confirmation and Selectivity

CO$_2$ reduction tends to produce different compounds, whereas their amounts and purity are usually rather low because of the insufficient conversion of CO$_2$. The identification and quantification of the products is crucial. The gaseous and liquid phase products can be detected and quantified by gas chromatography (GC) and high-performance liquid chromatography (HPLC), respectively.[108] However, the radical intermediates during the CO$_2$ reduction process have unpaired electrons and are hence unstable. They recombine at different stages, leading to distinct pathways and final products.[109] As such, in addition to GC, MS, and GC–MS, isotopic labeling, density functional theory (DFT) calculations, and in situ/operando techniques, as will be discussed in the following section, have also been used to explore reaction mechanism and pathways.[110] CO$_2$ reduction always competes with HER and can generate multiple compounds dependent on the number of electrons transferred. Product selectivity is thus an important metric. The selectivity of CO$_2$ reduction can be determined by the electrons transferred for CO$_2$ reduction divided by the overall electrons transferred for both CO$_2$ reduction and proton reduction. Further, the selectivity of a specific CO$_2$ reduction product can be calculated

by the corresponding electrons transferred multiplied by its formation rate divided by the sum of the other respective electrons transferred multiplied by their corresponding formation rate.[107]

3. Metal-Free Photocatalysts for CO$_2$ Reduction

Recent years have witnessed the rapid growth of metal-free catalysts for CO$_2$ photoconversion. A timely and comprehensive review on this expanding area is thus highly desirable. In this section, we elaborate metal-free photocatalysts reported to date for the CO$_2$ reduction, including graphene, g-C$_3$N$_4$, h-BN, BP, SiC, COFs, COPs, and other metal-free materials.

3.1. Graphene and Its Derivatives

As a one-atom-thick sp^2-bonded carbon 2D nanosheet with honeycomb rings, graphene has gained considerable research interest due to its unique structure and exceptional properties, such as large specific surface area, remarkable electron mobility, high transparency, excellent thermal chemical stability as well as flexibility.[111–113] Graphene has become an appealing candidate for construction of efficient photocatalysts for a range of reactions.[114–118] The use of graphene-derived photocatalysts for CO$_2$ reduction was first reported by Liang et al. in 2011.[119] Graphene can serve as an electron acceptor and transporter, greatly facilitating electron–hole separation and prolongation of charge carrier lifetimes.[120,121] The photoexcited electrons accumulate on the surface of graphene-based photocatalysts, favoring multielectron reactions. Graphene can also enhance photostability, increase light absorption, and promote the formation of small particles and their uniform dispersion.[67] Further attempts have been made to integrate graphene with semiconductors to improve photocatalytic activity.

Graphene oxide (GO) has been directly used in photocatalytic CO$_2$ reduction. Typically, GO has abundant hydroxyl, epoxy, carboxyl, and carbonyl groups.[122] The bandgap of GO was demonstrated to be modulated from 0.2 to 4.2 eV by changing the ratio of sp^2 and sp^3 hybridized atoms.[70,80] The band structure can also be tailored by manipulation of the fraction of –OH and –O moieties in GO.[123] The reduction potential of photogenerated electrons in the GO's CB was determined to be -0.79 V (vs NHE), being more negative compared with the potential of CO$_2$/CH$_3$OH (-0.38 V vs NHE), whereas the oxidation potential of photogenerated hole in the GO's VB was determined to be 4.00 V (vs NHE), being more positive compared with the potential of H$_2$O/O$_2$ (0.82 V vs NHE).[124] As such, GO was reported to be able to catalyze the photochemical reduction of CO$_2$ to CH$_3$OH,[124] delivering a CH$_3$OH yield rate of 0.172 μmol g$_{cat}^{-1}$ h^{-1}, six times as high as that of commercial P25 (TiO$_2$, Degussa) dispersions. As an extension, the same group decorated GO with copper nanoparticles (Cu-NPs) to adjust the work function of GO, thus promoting charge separation (CS) at the GO–Cu interface.[125] The solar fuel (CH$_3$OH, CH$_3$CHO) formation rate was substantially improved to be 6.84 μmol g^{-1} h^{-1} (10 wt% Cu), being over 60 and 240 times higher than that of GO and P25, respectively.

3.2. g-C$_3$N$_4$-Based Photocatalysts

g-C$_3$N$_4$, a layered nonmetallic semiconductor, is a polymeric material constructed from triazine (C$_3$N$_3$) or tri-s-triazine/heptazine (C$_6$N$_7$) rings and is often considered as sp^2-hybridized nitrogen-substituted graphene.[126,127] g-C$_3$N$_4$ has a narrow bandgap of about 2.7 eV and thus could be actively responsive to visible light ($\lambda_{2.7\,eV} = 459$ nm).[128–130] It exhibits a suitable negative CB position (≈ 1.1 V vs NHE) that meets the thermodynamic requirements of photocatalytic CO$_2$ reduction reactions.[131–134] DFT calculations revealed that the VB of g-C$_3$N$_4$ is a combination of the highest occupied molecular orbital (HOMO) levels of tri-s-triazine monomer originating from nitrogen p$_z$ orbitals, and the CB (lowest unoccupied molecular orbital (LUMO) of the monomer) mainly comprises carbon p$_z$ orbitals.[129,135] A recent study showed that increase in crystallinity of g-C$_3$N$_4$ significantly improved its photocatalytic performance, which was associated with the reduction of defects (speculated as carrier recombination centers).[133] Nevertheless, bulk g-C$_3$N$_4$ has shortcomings of insufficient visible light utilization, low exposed surface area, and rapid recombination of photoinduced electron/hole pairs.[136–138] The rational design and exploration of nanostructured g-C$_3$N$_4$-based photocatalysts with better CS/transfer efficiency has attracted intensive research interest.

3.3. BN-Based Photocatalysts

Hexagonal boron nitride (h-BN), an inorganic analog of graphene, has stimulated much attention due to its exceptional thermal conductivity (600 W m^{-1} K^{-1}) and large surface area (3300 m^2 g^{-1}).[139,140] The material is composed of a 1:1 ratio of alternating B and N atoms in a 2D honeycomb lattice. Although h-BN has a broad bandgap (5.2–5.5 eV), tuning of its morphology enables one to largely tailor its bandgap.[141] For example, porous h-BN was demonstrated to exhibit CB and VB positions at −1.16 and 3.05 V (vs NHE, pH 0), respectively, suitable for CO$_2$ photoreduction with 100% CO conversion.[141] Heterostructuring with graphene could reduce the bandgap of h-BN, rendering visible-light photocatalytic performance. The heterostructure facilitated an outstanding CO$_2$ photoconversion rate, eight-fold that of the physical mixture of graphene and h-BN. A large turnover frequency of 4.0 mmol benzylamine per gram per hour was obtained, outperforming many previously reported metal-free photocatalysts.[142] Introducing carbon into the lattice of h-BN (h-BCN) is also able to alter its band structure (**Figure 4**),[143] affording a bandgap of 2.64 eV with CB and VB positions at ≈−0.56 and 2.08 V, respectively, thus enabling photocatalytic CO$_2$ reduction to CO.[144]

3.4. Silicon Carbide

SiC is a semiconductor with high chemical and thermal stability.[145] The compound displays a broad bandgap (2.4–3.2 eV) and a high reduction potential (−1.40 V), making SiC a potential candidate for photocatalytic CO$_2$ reduction.[146] β-SiC with a hollow spherical 3D structure was demonstrated to remarkably accelerate photocatalytic reduction of CO$_2$ into CH$_4$. The CH$_4$ production rate was attained to be 16.8 μmol g^{-1} h^{-1} (or 376.4 μL g^{-1} h^{-1}), surpassing many reported metal oxide photocatalysts.[147]

3.5. Black Phosphorus-Based Photocatalysts

Black phosphorus (BP), an allotrope of phosphorus,[148] exhibits high charge mobility of 1000 cm^2 V^{-1} s^{-1} at ambient temperature and 6000 cm^2 V^{-1} s^{-1} at lower temperatures, which is much higher than 2D transition-metal dichalcogenides (TMDs) (≈ 300 cm^2 V^{-1} s^{-1}).[149] In particular, BP has an adjustable direct bandgap, which can be tuned from 0.3 to 2.0 eV as its layers decreased from bulk to monolayer, thereby holding a wide response in the solar light spectrum including near-infrared light.[150–152] A hybrid consisting of BP quantum dots (QDs) and g-C$_3$N$_4$ was capable of catalyzing photochemical conversion of CO$_2$ to CO with higher production rate (6.54 μmol g^{-1} h^{-1}) than pure g-C$_3$N$_4$ (2.65 μmol g^{-1} h^{-1}).[153]

3.6. COFs and COPs

COFs are a type of emerging porous materials, composed by light elements, including H, O, C, N, B, and Si, which are ingeniously created by linking organic building units through covalent bonds.[154–156] COFs bear advantages of high specific surface area, large and tunable porosity, and good thermal stability.[157,158] Notably, the framework structure and functionality of COFs can be tailored by manipulating the symmetry, size, and nature of building units.[159,160] Porphyrin–tetrathiafulvalene COFs could selectively catalyze photoconversion of CO$_2$ to CO with a formation yield of 12.33 μmol and selectivity of ≈100%.[161] In addition to large specific surface areas (564.6 m^2 g^{-1}) of the COFs in favor of photocatalytic performance, the effective ET from tetrathiafulvalene to porphyrin via covalent bonds resulted in separated electrons and holes available for corresponding CO$_2$ reduction and H$_2$O oxidation. 2D-COFs with ordered π-array structures, 1D nanopores, and efficient electron mobility offer an ideal channel for separation, diffusion, and migration of photoexcited carrier charges.[162] As such, COFs are proposed to be promising metal-free materials for photocatalytic CO$_2$ reduction.[163–165]

COPs are the analog of COFs with similar attractive properties. The heteroatom-rich (N, O, P) covalent organic polymer (NOP–COP) was reported to have a CB flat band position of −0.81 V (vs Ag/AgCl), being more negative than the reduction potential of CO$_2$ to CH$_4$ (−0.46 V vs Ag/AgCl), making it useful for CO$_2$ photocatalysis.[166] CH$_4$ was obtained as the only carbonaceous product with a generation rate of 22.5 μmol g$_{cat}^{-1}$ h^{-1} and selectivity >90%.

3.7. Other Metal-Free Materials

Biological materials have recently spurred great interest due to their multiple scales and hierarchical morphologies. A treated rape pollen (TRP) was applied for visible-light-driven photocatalytic CO$_2$ reductions, which exhibits a CO production rate of 488.4 μmol h^{-1} g^{-1} and a selectivity of 98.3% as well as a quantum efficiency of exceeding 6.7% at 420 nm
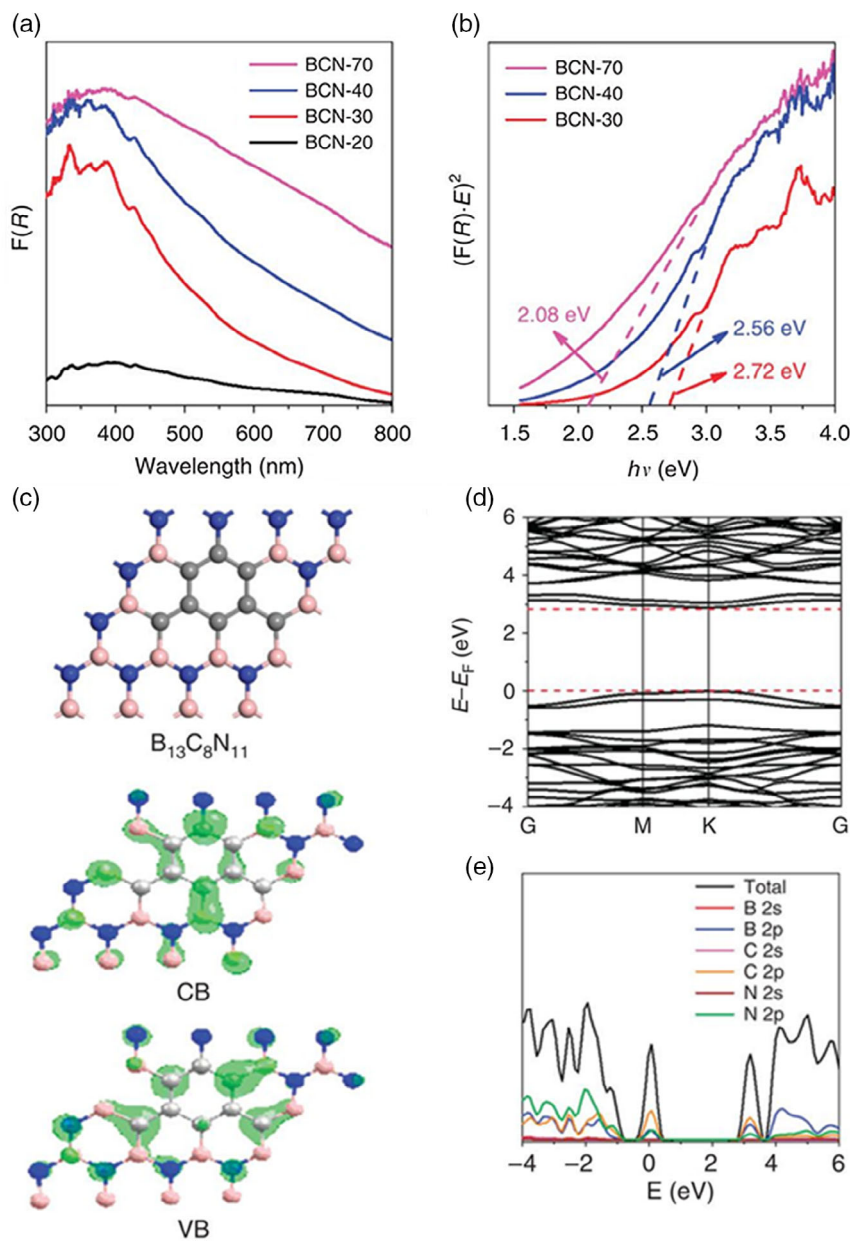
Figure 4. a) UV–DRS spectra of BCN and b) the corresponding plot to determine the band gap. c) The calculated optimized structure of $B_{13}C_8N_{11}$ with the respective VB/CB. d) Calculated energy band, and e) corresponding total and ion-decomposed density of state (DOS). Reproduced with permission.[143] Copyright 2015, Springer Nature.

without using cocatalyst or sacrificial agent.[167] Furthermore, the CO production rate achieved over the TRP catalyst is approximately 29.4 and 25.6 times as high as that of conventional photocatalysts of g-C_3N_4 (16.6 µmol h^{-1} g^{-1}) and P25 TiO$_2$ (19.1 µmol h^{-1} g^{-1}). The catalyst also showed impressive working stability.[167]

Boron has recently stimulated intense attention because of its unique structure, attractive properties, and a great potential as a photocatalyst for various reactions. Ye and co-workers synthesized elemental boron particles and explored for the first time their activity for photothermal conversion of CO_2.[110]

Elemental boron was found to be able to catalyze efficient aqueous reduction of CO_2 into CO and CH_4 under light illumination (without using sacrificial agents and cocatalysts). This was attributed to its efficient absorption in the UV/vis and up to IR regime, which results in local photothermal effect, thus facilitating CO_2 activation. Meanwhile, localized self-hydrolysis of boron was initiated to generate H_2 as proton origin and electron donor for CO_2 reduction. Boron oxides were also produced, which can promote CO_2 adsorption. As a consequence, boron materials are potential candidates for photocatalytic CO_2 reduction.

4. Strategies to Boost the Photocatalytic CO_2 Reduction over Metal-Free Catalysts

Despite recent advances in metal-free photocatalysis of CO_2 reduction, the overall solar energy conversion efficiency is limited because of poor light-harvesting capacity, rapid recombination of photoexcited carriers, and competitive proton reduction to hydrogen.[168] Therefore, it is imperative to explore effective approaches to further increase visible light absorption of metal-free matertials and optimize their CO_2 photoreduction performance. To this end, strategies such as doping, morphology control, defect introduction, surface modification, and heterojunction construction have been developed (**Figure 5**). In the following, we provide basic understanding and discussions on these approaches to facilitate further improvement in CO_2 reduction activity.

4.1. Doping

Elemental doping offers a protocol to strikingly modulate the optical and electronic structure of materials. The types and concentrations of doped elements significantly affect the properties of catalysts. **Table 2** lists recent results on photocatalytic CO_2 reduction by elemental doped nonmetallic-based materials. It shows that elemental doping can profoundly tailor the local surface microstructure and electronic properties of metal-free photocatalysts to enhance CO_2 reduction.

4.1.1. Nonmetal Atom Doping

Nonmetal doping has been frequently used to boost the photocatalytic activity by extending light response range and

Figure 5. Strategies employed for improving the photocatalytic CO_2 reduction over metal-free materials.

promoting carrier separation.[171,179,180] For example, incorporation of O into g-C_3N_4 nanotubes (OCN-Tube) could optimize the band structure of g-C_3N_4, leading to a smaller bandgap, higher CO_2 binding and uptake capacity, and improved carrier separation efficiency (**Figure 6**).[169] The obtained hierarchical OCN-Tube showed improved visible-light photocatalytic activity, affording a CH_3OH formation rate of 0.88 µmol g^{-1} h^{-1}, largely ourperforming bulk g-C_3N_4, which only gave a CH_3OH yield rate of 0.17 µmol g^{-1} h^{-1}. Similarly, doping of g-C_3N_4 with phosphorus could downshift the positions of both CB and VB and narrow its bandgap.[170] The P-doped g-C_3N_4 nanotubes (P-g-C_3N_4) delivered 3 to 14 times higher production of CO and CH_4, respectively, relative to pure g-C_3N_4. The formation ratio of CO/CH_4 substantially decreased from 6.0 (for g-C_3N_4) to 1.3, suggesting a superior CH_4 selectivity over P-g-C_3N_4.

Introducing fluorine into BCN was reported to remarkably accelerate migration-separation efficiency of photoinduced charge carriers.[172] As a result, the CO yield was improved by three times under visible light illumination.

In addition to single-element doping, multi-element codoping was also used to adjust the CO_2 photoreduction behavior.[173,174] Simultaneously incorporating oxygen and carbon gradually lowered the bandgap energy of g-C_3N_4 from 2.79 to 2.52 eV,[174] enabling a high CO selectivity with CO yield of up to 55.2 µmol g^{-1}. Such enhancement was attributed to the codoping with oxygen and carbon atoms, accelerating electron extraction and migration, and improving visible light absorption capability.

4.1.2. Metal Atom Doping

Metal atom doping can result in impurity levels in the bandgap structure of a semiconductor, which can act as electron traps under excited state. As an example, incorporation of Eu(III) into g-C_3N_4 was shown to improve CH_4 production from CO_2 photoreduction, about 2.2 times that of pure g-C_3N_4.[177] This increase in photocatalytic activity was proposed to result from Eu(III) species which could act as Lewis acids to trap photogenerated electrons, facilitating the transport of photoexcited carrier charges. Modification of covalent organic frameworks by transition metal ions (COF–M (M = Co/Ni/Zn)) was demonstrated to favor the evolution of CO or HCOOH products.[178] A yield rate of 1.02×10^3 µmol h^{-1} g^{-1} for CO formation was achieved over COF–Co, whereas a HCOOH formation rate of 152.5 µmol h^{-1} g^{-1} was attained over COF–Zn. Metal and nonmetal codoping is able to further improve CO_2 photoreduction performance. In this respect, amino-rich g-C_3N_4 photocatalyst incorporated with both K and carbon defects (K-AUCN) exhibited improved CO_2 fixation and activation (due to enriched basic amino groups), and efficient separation and transport of photoinduced charge carriers (arising from K incorporation and induced carbon defects) (**Figure 7**).[176] The K-AUCN provided over fivefold increase in CO_2 conversion compared with original g-C_3N_4. This points to the fact that elemental doping is a useful scheme to tune the optical and electronic properties, and energy band structure of nonmetallic photocatalysts, thereby enhancing their CO_2 reduction performance.

Table 2. Summary of the recent results on the photocatalytic reduction of CO_2 by elemental doped nonmetallic-based materials.

Photocatalyst	Synthetic method [Precursor]	Reaction medium	Illumination [Performance]	Ref.
O-doped g-C_3N_4 (Hierarchical porous nanotubes)	Thermal oxidation exfoliation and curling-condensation method (550 °C, 2 h and 600 °C, 4 h) ($C_3N_6H_6$)	$NaHCO_3$ and H_2SO_4	$\lambda \geq 420$ nm (350 W Xe); CH_3OH: 0.88 µmol g^{-1} h^{-1}; Stability: decrease	[169]
P-doped g-C_3N_4 (nanotubes)	Thermal reaction method (550 °C, 4 h) ($C_3N_6H_6$, $NaH_2PO_2\cdot H_2O$)	$NaHCO_3$ and H_2SO_4	Simulated sunlight (300 W Xe); CO: 2.37 µmol g^{-1} h^{-1}	[170]
S-doped g-C_3N_4	Thermal reaction method (520 °C, 2 h) ($C_3N_6H_6$ or CH_4N_2S)	$NaHCO_3$ and HCl	Simulated sunlight (300 W Xe); CH_3OH: 0.37 µmol g^{-1} h^{-1} (Pt 1 wt%)	[171]
F-doped Boron carbon nitride (BCN)	Thermal treating method (1250 °C, 5 h and 400 °C, 3 h) (B_2O_3, CH_4N_2O, $C_6H_{12}O_6$, and KF)	Water	$\lambda \geq 420$ nm (300 W Xe, 525 mW cm^{-2}); CO: 155 µmol g^{-1} h^{-1}; AQY@420 nm: 0.07%; Stability: >5 h	[172]
B and K codoped C_3N_4	Thermal reaction method (550 °C, 2 h) ($C_2H_4N_4$, KBH_4, and KNO_3)	Water	Simulated sunlight (300 W Xe, 430 mW cm^{-2}); CH_4: 1.19 µmol g^{-1} h^{-1}; Stability: >15 h	[173]
O and C codoped g-C_3N_4 (nanosheets)	In situ soft-chemical method (400 °C, 1 h and 550 °C, 4 h) ($C_3N_6H_6$ and $C_6H_{12}O_6$)	Water	$\lambda > 420$ nm (300 W Xe); CO: 4.6 µmol g^{-1} h^{-1}; Stability: >12 h	[174]
Mo-doped g-C_3N_4	Pyrolysis method (550 °C, 4 h) (($NH_4)_6Mo_7O_{24}\cdot 4H_2O$ and $C_3N_6H_6$)	Water vapor	UV-visible (300 W Hg lamp); CO: 111 µmol g^{-1} h^{-1}	[175]
K-doped polymerized g-C_3N_4	Thermal reaction and chemical activation method (550 °C, 2 h and 500 °C, 4 h) (CH_4N_2O and KOH)	Water vapor	Simulated sunlight (Xe lamp, Newport 6700, USA) CO: 9.86 µmol g^{-1} h^{-1}; Stability: decrease	[176]
Eu-doped g-C_3N_4	Thermal reaction method (550 °C, 4 h and 380 °C, 2 h) (CH_4N_2O and $Eu(NO_3)_3\cdot 6H_2O$)	Water	Simulated sunlight (300 W Xe); CH_4: 22.8 µmol g^{-1} h^{-1}; AQY@420 nm: 1.6%	[177]
Zn-doped COF (2,6-diaminoanthraquinone – 2,4,6-triformylphloroglucinol)	Hydrothermal reaction (120 °C, 72 h) (2,6-diaminoanthraquinone, 2,4,6-triformylphloroglucinol, *N,N*-dimethylacetamide, 1,3,5-trimethylbenzene and $Zn(OAc)_2\cdot 2H_2O$)	Water	$\lambda \geq 420$ nm (300 W Xe); CO: 152.5 µmol g^{-1} h^{-1}; Stability: decrease	[178]

4.2. Morphology Control

The morphology of semiconductor materials can greatly influence their photocatalytic performance. Nanostructuring by controlling particle size, shapes, geometrical features, and surface textures[141,181–183] promotes carrier transportation and migration, and may also increase surface reactivity of semiconductors.[184] A number of metal-free catalysts with distinct morphologies have been synthesized and investigated for photochemical CO_2 reduction. Recent results on photocatalytic CO_2 reduction using nonmetallic-based materials with various morphologies are provided in **Table 3**.

Bulk layered g-C_3N_4 has been exfoliated into 2D nanosheets via a controllable process in an NH_3 atmosphere.[185] Nanosheets with about 3 nm thickness were obtained, which are likely 9–10 layers of conjugated planes of g-C_3N_4. The 2D g-C_3N_4 nanosheets exhibit large specific surface areas, high density of surface active sites, and shortened carrier migration distance (from the interior to the surface of g-C_3N_4). These advantages enhanced CS efficiency and boosted photocatalytic activity toward CO_2 reduction. Alternatively, construction of a tubular structure[186] such as interconnected nanotubes with hierarchical pores[169] can endow photocatalysts with larger surface-to-volume ratio, higher light utilization efficiency, and enhanced diffusion kinetics, as a result of more exposed active sites and light reflection/scattering channels.

Combining heteroatom doping and creation of porous tubular structure allows one to further improve photocatalytic activity. Such concept has been proved by the formation of porous nitrogen-enriched g-C_3N_4 nanotubes (TCN(NH_3)) featuring with Lewis basicity and high surface area (**Figure 8**a–d), which facilitated CO_2 adsorption and enhanced photocatalytic CO_2 reduction.[89]
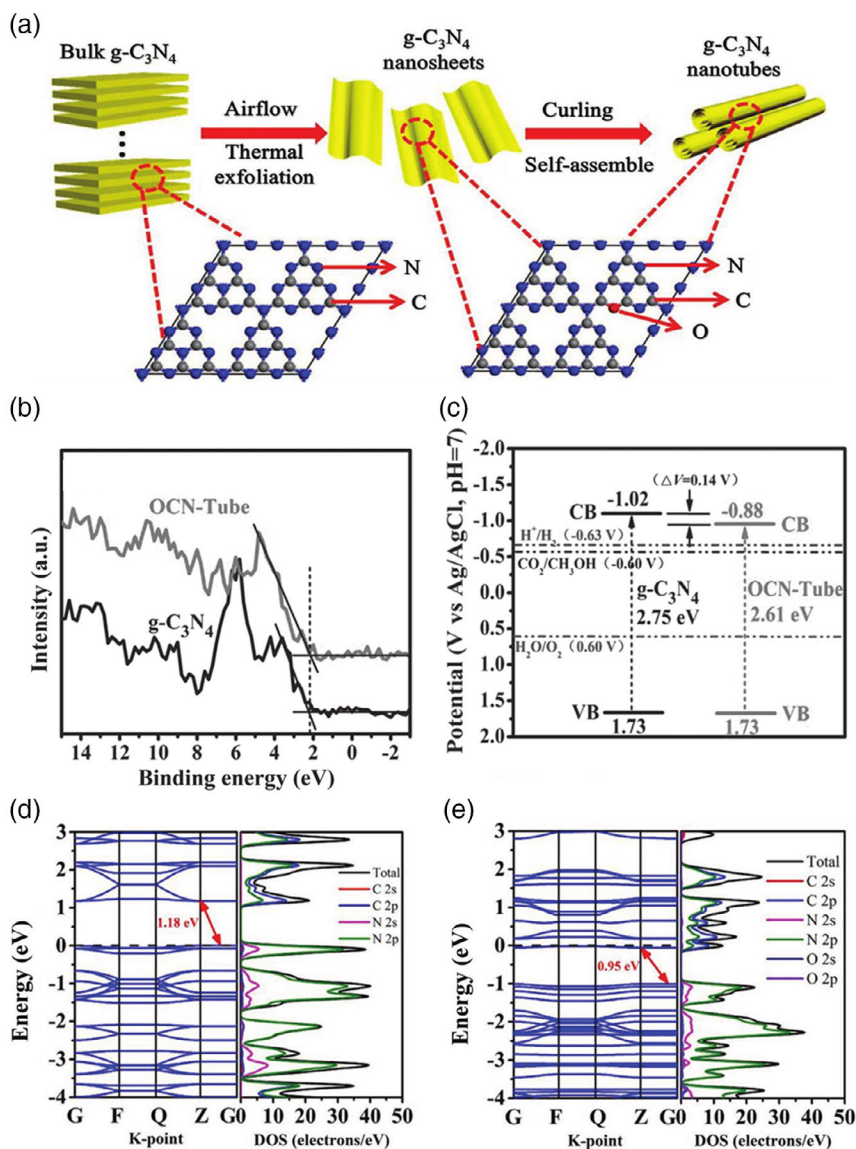
Figure 6. a) Schematic of the synthesis of hierarchical O-doped g-C_3N_4 nanotubes (OCN-Tube). b) XPS VB spectra. c) Band alignments of bulk g-C_3N_4 and OCN-Tube (vs Ag/AgCl, pH 7). Calculated band structures and DOS of d) bulk g-C_3N_4 and e) OCN-Tube models. Reproduced with permission.[169] Copyright 2017, Wiley-VCH.

3D spherical β-SiC with a hollow morphology was prepared. This catalyst has a peculiar electronic structure and large surface area and can effectively catalyze the reduction CO_2 to CH_4 and other hydrocarbon major products.[147] The evolution mechanism of SiC hollow spheres was speculated to include five steps, as shown in Figure 8e–i.

4.3. Vacancy Introduction

It has been recognized that introducing vacancies is another effective way to tailor the electronic structure of photocatalysts.[189,190] The vacancies on the surface of a catalyst can affect the visible light absorption, charge carrier transport and separation, and also behave as active centers for CO_2 adsorption and

activation.[191] Several anion vacancies-tuned metal-free photocatalysts including carbon vacancies and nitrogen vacancies have been applied for CO_2 reduction.[192,193] Recent results on the photocatalytic CO_2 reduction by nonmetallic-based materials with anion vacancies are presented in **Table 4**.

Introduction of C vacancies into g-C_3N_4 has been accomplished by annealing in an NH_3 atmosphere, which enabled over two times increase in CO formation rate as compared with original g-C_3N_4.[193] It was inferred that the enriched C vacancies not only enhanced CO_2 adsorption and activation but also upshifted the CB and improved electron/hole pair concentration and lifetimes. In addition, the creation of C vacancies reduced exciton-effects and promoted charge carrier generation, leading to improved CO_2 conversion.
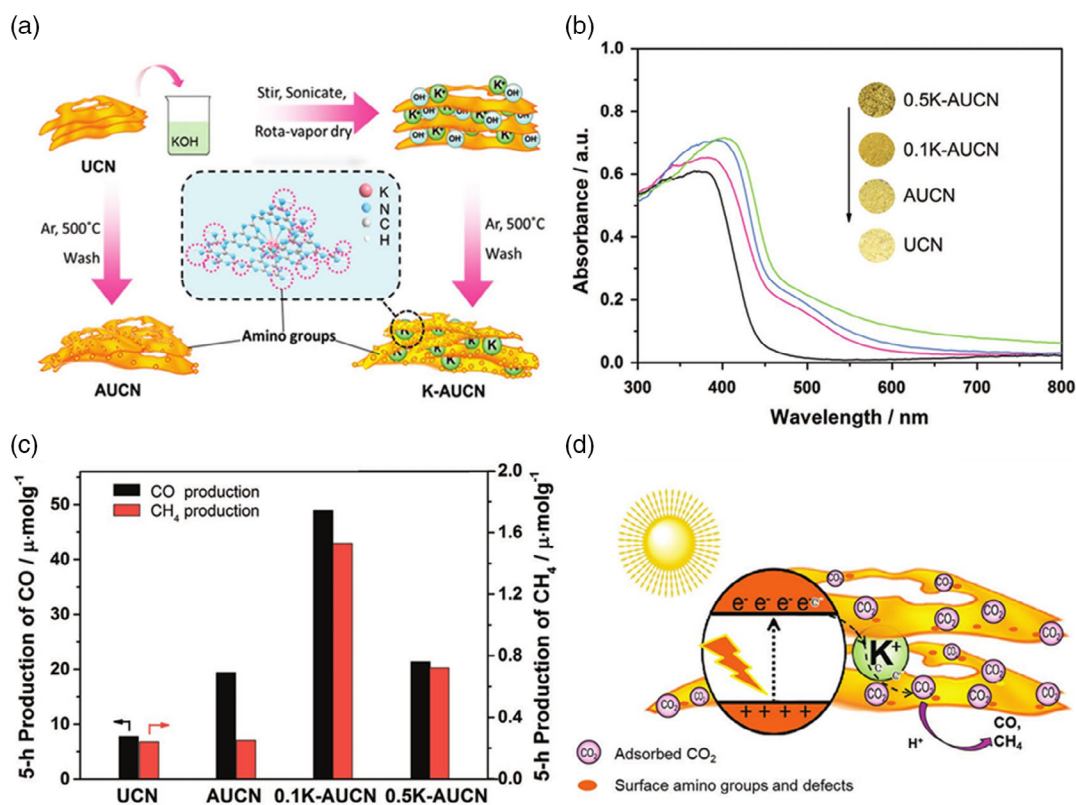
Figure 7. a) Schematic of the formation of K-incorporated amino-rich carbon nitride (K-AUCN) and AUCN. b) UV–vis DRS spectra. c) 5 h productions of CO and CH_4 in photocatalytic CO_2 reduction over UCN, AUCN, 0.1 K-AUCN, and 0.5 K-AUCN. d) Schematic illustration of K-AUCN promoted photocatalytic CO_2 reduction. Reproduced with permission.[176] Copyright 2017, Wiley-VCH.

Table 3. Summary of the recent results on the photocatalytic reduction of CO_2 by nonmetallic-based materials with various morphologies.

| Photocatalyst (Morphology)	Synthetic method [Precursor]	Reaction medium	Illumination [Performance]	Ref.
g-C_3N_4 (Ultra-thin nanosheet)	Thermal oxidation exfoliation method (550 °C, 3 h and 580 °C, 3 h) ($C_2H_4N_4$)	H_2SO_4 and $NaHCO_3$	Simulated sunlight (300 W Xe); CH_3OH: 1.87 µmol g^{-1} h^{-1}	[185]
g-C_3N_4 (Hexagonal tubular)	Hydrothermal method (180 °C, 12 h) ($C_3N_6H_6$)	Water	$\lambda \geq 420$ nm (300 W Xe); CO: 2.93 µmol g^{-1} h^{-1}; Stability: decrease	[186]
g-C_3N_4 (Nanotubes)	Supramolecular self-assembly ($C_3N_6H_6$ and $H_3NO \cdot HCl$)	Water vapor	$\lambda \geq 420$ nm (300 W Xe); CO: 103.6 µmol g^{-1} h^{-1}; Stability: decrease	[89]
g-C_3N_4 (Hierarchical 3D porous)	Thermal polymerization method (550 °C, 3 h) (CH_4N_2O)	H_2SO_4 and $NaHCO_3$	Simulated sunlight (300 W Xe); CH_4: 11.2 µmol g^{-1} h^{-1}; Stability: >9 h	[187]
P-CN (Nanocages)	Thermal-polymerization method (550 °C, nitrogen atmosphere, 2 h) ($C_3N_6H_6$ and $C_3H_3N_3O_3$)	H_2SO_4 and $NaHCO_3$	$\lambda > 420$ nm (350 W Xe, AM 1.5 filter); CO: 1.26 µmol g^{-1} h^{-1}; Stability: decrease	[188]
BN (Porous)	Thermal treating method (1050 °C, 3.5 h) (H_3BO_3, CH_4N_2O, and $C_3H_6N_6$)	Water vapor	$\lambda \geq 400$ nm (300 W Xe); CO: 1.16 µmol g^{-1} h^{-1}; Stability: decrease	[141]
SiC (Hollow sphere)	Sol-gel method (550 °C, 5 h) (PEO-PPO-PEO, $C_6H_{12}O_6$, $C_8H_{20}O_4Si$, and HCl)	Water	Simulated sunlight (300 W Xe); CH_4: 16.8 µmol g^{-1} h^{-1}	[147]

1900546 (11 of 41)
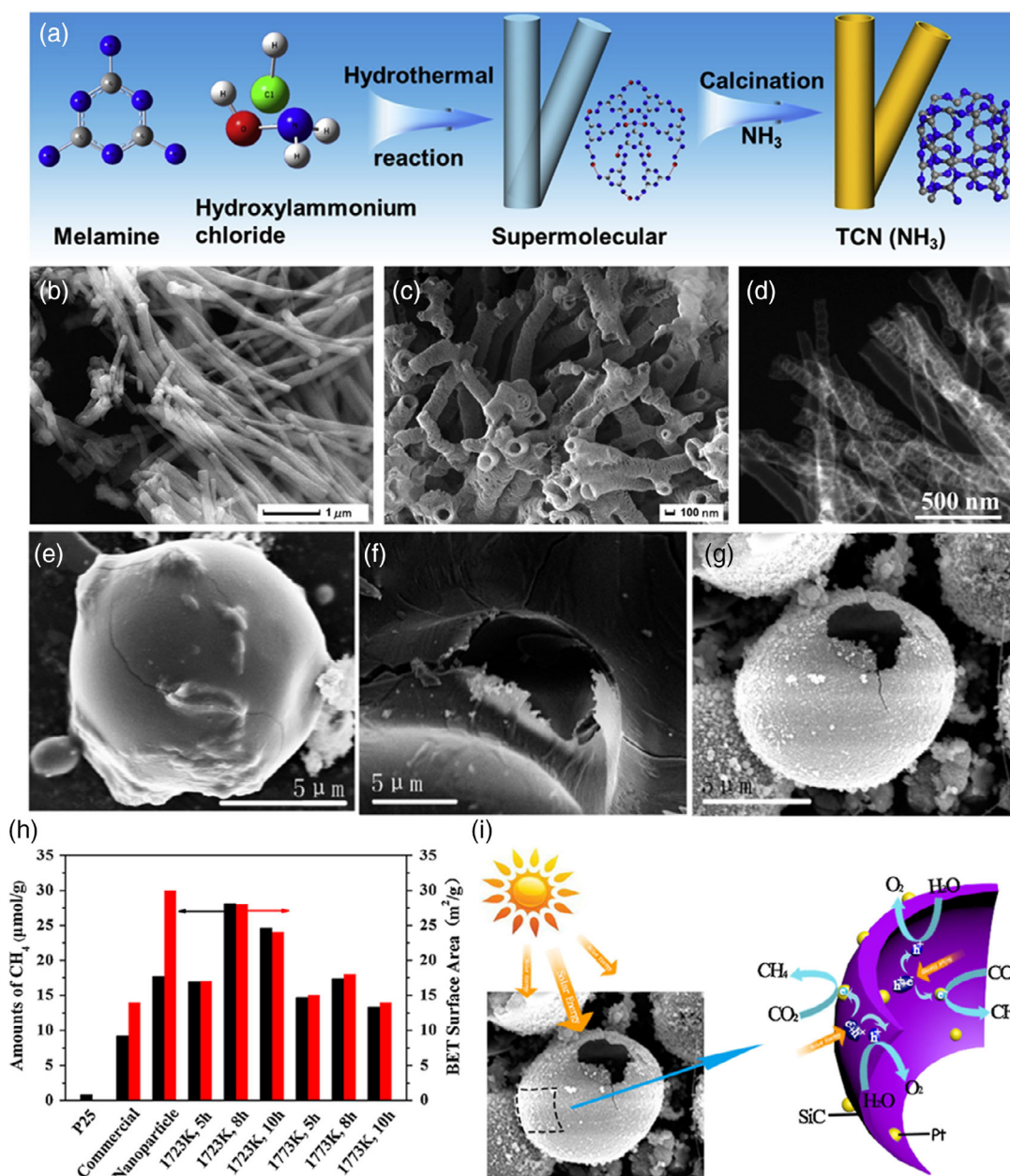
Figure 8. a) Schematic of the synthesis of TCN(NH$_3$). b,c) Scanning electron microscopy (SEM) and d) Transmission electron microscopy (TEM) images of TCN(NH$_3$). Reproduced with permission.[89] Copyright 2019, Elsevier. SEM images of e) SiC sample after carbothermic reduction at 1723 K for 8 h in Ar and f) SiC sample after calcined at 873 K for 5 h in O$_2$, and g) as-prepared SiC. h) Relationship between Brunauer–Emmett–Teller surface area and CH$_4$ formation rate of SiC samples under simulated solar light illumination for 4 h. i) Schematic of the charge transfer in Pt/SiC hollow spheres for CO$_2$ reduction with H$_2$O to CH$_4$. Reproduced with permission.[147] Copyright 2017, Elsevier.

Surface vacancies can simultaneously modulate visible light absorption, charge carrier transport and separation, and CO$_2$ activation. For instance, both experimental and theoretical results demonstrated that nitrogen vacancies in g-C$_3$N$_4$ induced midgap states below the CB edge, resulting in extension of the visible light response range (up to 598 nm).[192] Suitable midgap states trapped photoinduced electrons to accelerate the transport and separation of charge carriers. Indeed, the defective g-C$_3$N$_4$ nanosheets with an optimized nitrogen vacancy content exhibited

enhanced CO$_2$ reduction to CO, with yield rate four times higher than that of bulk g-C$_3$N$_4$.

Apart from creation of surface carbon or nitrogen vacancies, introduction of new elements or species on the semiconductor surface enables optimization of its visible light absorption, accelerates charge carrier transport and separation, and tunes CO$_2$ reduction selectivity.[194] As expected, generation of surface defects of cyano and carboxyl groups in g-C$_3$N$_4$ dramatically improved visible light absorption, enhanced surface charge

Table 4. Summary of the recent results on the photocatalytic reduction of CO_2 by nonmetallic-based materials with anion vacancies.

Photocatalyst (Vacancy type)	Synthetic method [Precursor]	Reaction medium	Illumination [Performance]	Ref.
g-C_3N_4 (Nitrogen)	Thermal treating- hydrogenate method (550 °C, 4 h) ($C_3N_6H_6$)	Water	$\lambda \geq 420$ nm (300 W Xe); CO: 124.2 µmol g^{-1} h^{-1}	[192]
C_3N_4 (Nitrogen)	Thermal reaction method (550 °C, 2 h) ($C_2H_4N_4$, KBH_4 and KNO_3)	Water	Simulated sunlight (300 W Xe, 430 mW cm^{-2}); CH_4: 1.19 µmol g^{-1} h^{-1}; Stability: >15 h	[173]
g-C_3N_4 (Nitrogen)	Therm alpolymerization method (550 °C, 3 h) ($C_2H_4N_4$ and $C_4H_6O_6$)	Water	$\lambda \geq 400$ nm (300 W Xe); CO: 56.9 µmol g^{-1} h^{-1}	[191]
g-C_3N_4 (Carbon)	Thermal reaction method (550 °C, 2 h and 510 °C in NH_3 atmosphere) (CH_4N_2O)	Water vapor	Simulated sunlight (300 W Xe, 300 mW cm^{-2}); CO: 4.18 µmol g^{-1} h^{-1}	[193]
g-C_3N_4 (Surface defect)	Solvothermal- calcination method (180 °C, 48 h and 550 °C, 3 h) (CH_6ClN_3, $C_2H_4N_4$, and $C_3H_6N_6$)	H_2SO_4 and $NaHCO_3$	Simulated sunlight (300 W Xe, AM 1.5 filter); CH_4: 12.07 µmol g^{-1} h^{-1}	[194]

accumulation and electron–hole separation, and also prolonged charge carrier lifetimes (**Figure 9**).[194] Such defect-rich g-C_3N_4 exhibited good activity for gas-phase CO_2 photoreduction into hydrocarbons with reasonable production rate (12.07 µmol h^{-1} g^{-1}) and selectivity (91.5%), outperforming most previously reported g-C_3N_4 photocatalysts.

4.4. Surface Modification

4.4.1. Surface Functional Groups

Surface modification of a photocatalyst with functional species allows one to tune reaction activity and selectivity.[195] Virtually, modification with amines can significantly increase CO_2 adsorption capacity to boost CO_2 reduction, considering that CO_2 is a Lewis acid.[196] Huang et al. showed that amine-functionalized g-C_3N_4 remarkably improved the CH_4 production rate of up to 0.34 µmol g^{-1} h^{-1}.[197] Such enhancement in activity was attributed to the substantially improved CO_2 chemisorption. Coincorporation with elements and basic groups can further optimize photocatalytic CO_2 reduction performance.[170] For example, the visible light absorption and bandgap structure of g-C_3N_4 can be effectively adjusted by simultaneously incorporating P element and cyano groups (—C≡N) into the semiconductor framework, enabling a 1.58 times enhanced CO_2 reduction efficiency compared with pure g-C_3N_4.[198]

4.4.2. Cocatalysts

Loading with suitable cocatalysts can boost the total photocatalytic efficiency of semiconductors by promoting surface CS, activating surface reactive sites, lowering activation energy, increasing selectivity of specific products, and improving photochemical stability.[199,200] The cocatalysts that have been utilized to improve the CO_2 photoreduction performance of metal-free materials involve precious metals (e.g., Pt, Au, Pd), non-noble metals and/or their metal oxides (e.g., Cu, Co, Mg, Bi, Ni,

NiO, MnO_x, CuO_x), alloys (e.g., Cu/Mo), and nonmetallic materials (e.g., graphene, carbon quantum dots [CQDs]). Recent results on photocatalytic CO_2 reduction by nonmetallic-based materials with cocatalysts are summarized in **Table 5**.

Metal-Based Cocatalysts: Due to their Fermi level which is lower than the bottom of the CB of semiconductors, metals and/or their oxidized species are potential cocatalysts to form Schottky barriers at the metal-semiconductor interface, and accelerate carrier separation, multi-electron migration, and CO_2 reduction rates.[83] In particular, noble metal cocatalysts exhibiting localized surface plasma resonance (SPR) properties have been considered as one of the effective electron traps to promote CS. Furthermore, due to SPR effects, the plasmonic noble metal NPs can serve as an alternative type of sensitizer, which could extend the visible light response range and improve photocatalytic performance.[201]

Nonnoble metals have been shown to be effective alternative cocatalysts for photocatalytic CO_2 reduction.[88,208] For example, decoration of g-C_3N_4 with Bi boosted the CO_2 conversion to yield CO and CH_4.[213] This enhancement can be attributed to the formation of a Schottky junction between g-C_3N_4 and Bi, thus facilitating charge carrier separation and electron accumulation in g-C_3N_4. The results likely provide basic prerequisites for initiation of multi-electron reactions.

Recent studies demonstrated that single atomtic sites could serve as efficient cocatalysts to tailor the photocatalytic properties.[213,214] Their distinct electronic structure and low-coordinated state render single atoms to be extremely active and selective for many reactions. This can be reflected by the finding that modification of g-C_3N_4 with single cobalt sites imparted impressive photocatalytic performance and product selectivity for CO_2 reduction.[213] Another interesting result from Zou and co-workers showed that COF coordinated with single Ni sites (Ni-TpBpy) provided a collaborative catalysis for selective photochemical CO_2 reduction.[214] The Ni-TpBpy generated 4057 µmol g^{-1} of CO in a 5 h reaction with a CO selectivity of 96% (**Figure 10**). Based on a combination of experimental tests
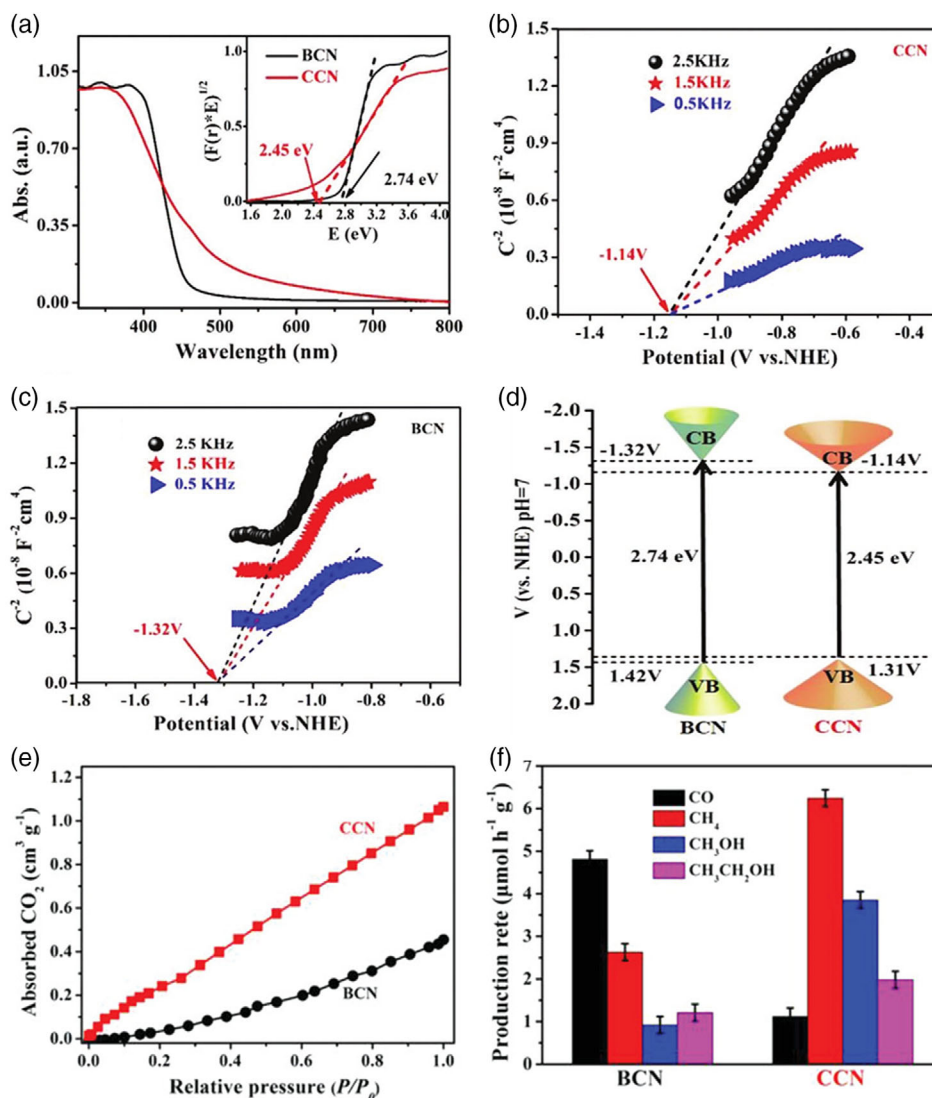
Figure 9. a) UV–vis diffuse reflectance spectra (Inset shows the calculation of bandgaps of CNs). b,c) Mott–Schottky plots. d) Band structure alignment of BCN and CCN. e) CO_2 adsorption isotherms of CCN and BCN. f) Photocatalytic CO_2 reduction properties of CCN and BCN at a humidity of 86%. Reproduced with permission.[194] Copyright 2019, WILEY-VCH.

and theoretical calculations, the high performance was proposed to stem from a synergy between single Ni atoms and TpBpy. TpBpy acted as a host for Ni sites and also facilitated CO_2 adsorption and activation. The COF structure also inhibited the parasitic H_2 evolution reaction.

Metal-Free Cocatalysts: Nonmetallic materials including graphene and CQDs also showed efficiency in promoting CO_2 conversion.[221,224–226] A 2.3-fold enhancement in visible-light photoactivity for CO_2 reduction has been achieved over graphene/g-C_3N_4 nanocomposites compared with pure g-C_3N_4.[221] The improved performance was supposed to originate from effective separation of charge carriers promoted by graphene. The use of CQDs to modify g-C_3N_4 could improve adsorption of nonpolar CO_2 and enhance the reaction kinetics to generate CH_4 (**Figure 11**).[225] In contrast to g-C_3N_4 that only generated CO and H_2, CQDs/g-C_3N_4 produced six times higher CO and

comparable CH_4 without detectable H_2 under the same condition.

Metal Complex Cocatalysts: Metal complexes have been used as a photosensitizer and/or cocatalyst, which can function as light absorption center or active sites to capture electrons.[227,228] Therefore, metal complexes can be incorporated into metal-free materials to sufficiently improve their optical and photocatalytic activities.[229–231] **Table 6** shows the recent results on photocatalytic CO_2 reduction by nonmetallic-based materials with metal complex cocatalysts. A range of Ru complexes have been reported to be such promoters for C_3N_4 to catalyze CO_2 reduction in organic systems.[232–235] The immobilized metal complex served as an electron acceptor and also provided active sites for CO_2 reduction. The photocatalytic properties were found to largely depend on the structure of the metal complexes (**Figure 12**). Importantly, HCOOH (80%) was produced as main product

Table 5. Summary of the recent results on the photocatalytic reduction of CO_2 by nonmetallic-based materials with cocatalysts.

Photocatalyst (Cocatalyst)	Synthetic method [Precursor]	Reaction medium	Illumination [Performance]	Ref.
C_3N_4 (Pd 5.8%)	Thermal reaction and solvothermal method (550 °C, 4 h and 150 °C, 2 h) ($C_3N_6H_6$, K_2PdCl_4, $Na_2C_2O_4$, and PVP)	Water	$\lambda > 400$ nm (300 W Xe); C_2H_5OH: 2.18 μmol g^{-1} h^{-1}	[201]
g-C_3N_4 (Pd 0.39%)	Thermal treatment and electrostatic assembly method (500 °C, 2 h) (CH_4N_2O, Na_2PdCl_4, PVP)	H_2SO_4 and $NaHCO_3$	Simulated sunlight (300 W Xe); C_2H_5OH: 3.17 μmol g^{-1} h^{-1}	[202]
g-C_3N_4 (Pd)	Thermal reaction and solvothermal method (550 °C, 3 h and 150 °C, 2 h) (CH_4N_2O, K_2PdCl_4, $Na_2C_2O_4$ and PVP)	Water	$780 > \lambda > 420$ nm (300 W Xe); CO: 4.3 μmol g^{-1} h^{-1}; Stability: decrease	[203]
g-C_3N_4 (Pt 2 wt%)	Thermal reaction and chemical reduction method (550 °C, 2.5 h and 150 °C, 2 h) (CH_4N_2O and $H_2PtCl_6 \cdot 6H_2O$)	Water	Simulated sunlight (300 W Xe); CH_4: 1.3 μmol g^{-1} h^{-1}	[204]
g-C_3N_4 (Au)	Thermal reaction and conant temperature bath-reduction (550 °C, 4 h; 500 °C, 2 h; 80 °C, 2 h) (CH_4N_2O, $HAuCl_4$ and KBH_4)	NaOH	UV light (8 W Hg lamp); CO: 77.5 μmol g^{-1}; Stability: decrease	[205]
P-doped g-C_3N_4 (Au)	Thermal reaction and in situ photo-reduction method (550 °C, 4 h) ($C_2H_4N_4$, phosphorus, and $HAuCl_4$)	Water	Simulated sunlight (300 W Xe); CH_4: 24 μmol	[206]
g-C_3N_4 (Co(bpy)$_3^{2+}$)	Thermal reaction and chemical reduction method (550 °C, 4 h) ($C_3N_6H_6$, $NaBH_4$, and Co(bpy)$_3^{2+}$)	Water	$\lambda \geq 420$ nm (300 W Xe); CO: 7.6 μmol; Stability: decrease	[207]
g-C_3N_4 (Cu)	Sonicated assisted wet-impregnation method (550 °C, 2 h) ($C_3N_6H_6$ and Cu(NO$_3$)$_2 \cdot 3H_2O$)	Water	$\lambda \geq 420$ nm (300 W Xe); CO: 142 μmol g^{-1} h^{-1}	[88]
g-C_3N_4 (Cu 6%)	Thermal reaction and microwave hydrothermal method (550 °C, 4 h) ($C_2H_4N_4$ and Cu(NO$_3$)$_2 \cdot 3H_2O$)	Water	Simulated sunlight (300 W Xe); CO: 9.89 μmol g^{-1} h^{-1}	[208]
g-C_3N_4 (Mg)	In-situ hydrothermal deposition method (520 °C, 3 h and 180 °C, 12 h) (CH_4N_2O and Mg(NO$_3$)$_2 \cdot 6H_2O$)	Water	Simulated sunlight (350 W Xe); CH_4: 2.85 μmol g^{-1} h^{-1}	[209]
g-C_3N_4 (Bi)	Thermal polymerization and hydrothermal method (550 °C, 2 h and 160 °C, 12 h) (CH_4N_2O, PVP, and Bi(NO$_3$)$_3 \cdot 5H_2O$)	Water	$\lambda \geq 420$ nm (300 W Xe); CO: 1.66 μmol g^{-1} h^{-1}	[210]
g-C_3N_4 (Mo)	Thermal polycondensation method (550 °C, 4 h) ($C_3H_6N_6$ and (NH$_4$)$_6$Mo$_7$O$_{24} \cdot 4H_2O$)	Water	$\lambda \geq 420$ nm (300 W Xe); CO: 18 μmol g^{-1} h^{-1}	[211]
g-C_3N_4 (Se)	Thermal polycondensation method (550 °C, 1 h) (CH_4N_2O and $C_{12}H_{10}Se_2$)	Water	Simulated sunlight (300 W Xe); CO: 200 μmol g^{-1} h^{-1}; Stability: decrease	[212]
C_3N_4 (Co)	Thermal polymerization and deposition method (600 °C, 4 h and 80 °C, 2 h) (CH_4N_2O, $CoCl_2$, and $C_6H_{15}N$)	Water	$\lambda > 420$ nm (halogen lamp, 200 mW cm^{-2}); CO: 64 μmol g^{-1} h^{-1}; Stability: decrease	[213]
2,2′-bipyridine-based COF (Ni)	Chelation of bypyridine binding units method (Triformylphloroglucinol, 5,5′-diamino-2,2′-bipyridine, and Ni(ClO$_4$)$_2 \cdot 6H_2O$)	Water	$\lambda \geq 420$ nm (300 W Xe); CO: 812.4 μmol g^{-1} h^{-1}; AQY@420 nm: 0.3%; Stability: decrease	[214]

Table 5. Continued.

Photocatalyst (Cocatalyst)	Synthetic method [Precursor]	Reaction medium	Illumination [Performance]	Ref.
B-P codoped g-C$_3$N$_4$ (SnO$_2$)	Thermal polymerization and hydrothermal method (550 °C, 4 h and 500 °C, 2 h) (C$_2$H$_4$N$_4$, SnCl$_4$·5H$_2$O, and NaOH)	NaOH	$\lambda \geq 420$ nm (300 W Xe); CH$_4$: 3.6 µmol g^{-1} h^{-1}	[215]
g-C$_3$N$_4$ (MoO$_2$)	Self-assembly method (550 °C, 2 h and 180 °C, 12 h) (CH$_4$N$_2$O and (NH$_4$)$_6$Mo$_6$O$_{24}$)	NaHCO$_3$ and H$_2$SO$_4$	Simulated sunlight (300 W Xe); CO: 2.0 µmol g^{-1} h^{-1}; Stability: >9 h	[216]
g-C$_3$N$_4$ (CuO$_x$)	Thermal polycondensation method (520 °C, 4 h) (C$_3$H$_6$N$_6$ and Cu(NO$_3$)$_2$)	Water	Simulated sunlight (300 W Xe); CO: 1.2 µmol g^{-1} h^{-1}; Stability: >16 h	[217]
g-C$_3$N$_4$ (Single TiO)	Thermal polycondensation method (550 °C, 4 h) (TiCl$_4$, NH$_4$Cl, and C$_2$H$_4$N$_4$)	Water	$\lambda \geq 420$ nm (300 W Xe); CO: 283.9 µmol g^{-1} h^{-1}	[218]
g-C$_3$N$_4$ (Ni/NiO)	Thermal polymerization and photoreduction method (500 °C, 3 h) (CH$_4$N$_2$S, Ni(NO$_3$)$_2$·6H$_2$O, and C$_2$H$_7$NO)	Water	Simulated sunlight (300 W Xe); CO: 27.9 µmol g^{-1} h^{-1}	[219]
g-C$_3$N$_4$ (Pd$_9$Cu$_1$H$_x$)	Thermal polymerization and hydrothermal method (160 °C, 16 h) (C$_3$N$_4$, PVP, KBr, K$_2$PdCl$_4$, CuCl$_2$·2H$_2$O, and C$_3$H$_7$NO)	Water	780 nm > λ > 420 nm (300 W Xe); CH$_4$: 1.2 µmol g^{-1} h^{-1}; Stability: decrease	[220]
g-C$_3$N$_4$ (Graphene)	Impregnation thermal reduction strategy (520 °C, 2.5 h and 520 °C, 4 h) (GO and CH$_4$N$_2$O)	Water	$\lambda \geq 420$ nm (300 W Xe, 8.5 mW cm^{-2}); CH$_4$: 5.87 µmol g^{-1}	[221]
g-C$_3$N$_4$ (RGO)	Thermal polymerization and hydrothermal method (550 °C, 2 h and 190 °C, 2 h) (CH$_4$N$_2$O and GO)	Na$_2$CO$_3$	$\lambda \geq 420$ nm (100 W halogen); HCHO: 10.3 µmol g^{-1} h^{-1}; AQY: 22.3%; Stability: decrease	[222]
SiC (RGO)	Vapor-solid reaction (1400 °C, 3 h and 700 °C, 1 h) (GO and Si)	Water	Simulated sunlight (300 W Xe, 0.85 mW cm^{-2}); CH$_4$: 58.17 µmol g^{-1} h^{-1}; Stability: >12 h	[223]
g-C$_3$N$_4$ (Carbon nanodots)	Thermal polymerization and hydrothermal method (520 °C, 2.5 h and 120 °C, 4 h) (CH$_4$N$_2$O and C$_6$H$_{12}$O$_6$)	Water vapor	λ > 400 nm (500 W halogen, AM 1.5); CO: 58.82 µmol g^{-1}; AQE: 0.076%; Stability: decrease	[224]
g-C$_3$N$_4$ (Carbon quantum dots)	Thermal polymerization and hydrothermal method (520 °C, 2 h and 200 °C, 12 h) (CH$_4$N$_2$O and C$_6$H$_{12}$O$_6$)	Water vapor	λ > 400 nm (300 W halogen); CO: 118 µmol g^{-1}; Stability: >25 h	[225]

along with small amounts of CO and H$_2$ using the Ru complex/ C$_3$N$_4$ photocatalyst, whereas only H$_2$ was obtained over pure C$_3$N$_4$. It was inferred that the photoexcited electrons were delivered from C$_3$N$_4$ to Ru complex while holes left in the VB would react with electron-donating agent such as triethanolamine (TEOA), which accelerated separation of photoinduced charge carriers, leading to enhanced photocatalytic CO$_2$ reduction.

In addition to Ru complexes, Fe quaterpyridine complexes were also shown to be capable of facilitating efficient photocatalytic CO$_2$ reduction selectively to CO over mesoporous C$_3$N$_4$ under visible light illumination ($\lambda \geq 400$ nm).[240] A selectivity of up to 97% for CO formation with a turnover number of 155 and an apparent quantum yield of about 4.2% was achieved. Even better results were obtained when using Fe tetra (4-carboxylphenyl) porphyrin chloride (FeTCPP) molecular cocatalyst anchored on g-C$_3$N$_4$, delivering a yield of 6.52 mmol g^{-1} in 6 h and selectivity of 98% for CO formation. Such enhanced activity was closely associated with the strong ET from the g-C$_3$N$_4$ nanosheets to FeTCPP (**Figure 13**a).[239] Similar enhancement effects have been observed for polymeric cobalt phthalocyanine cocatalyst (CoPPc) decorated on mesoporous C$_3$N$_4$ for CO$_2$
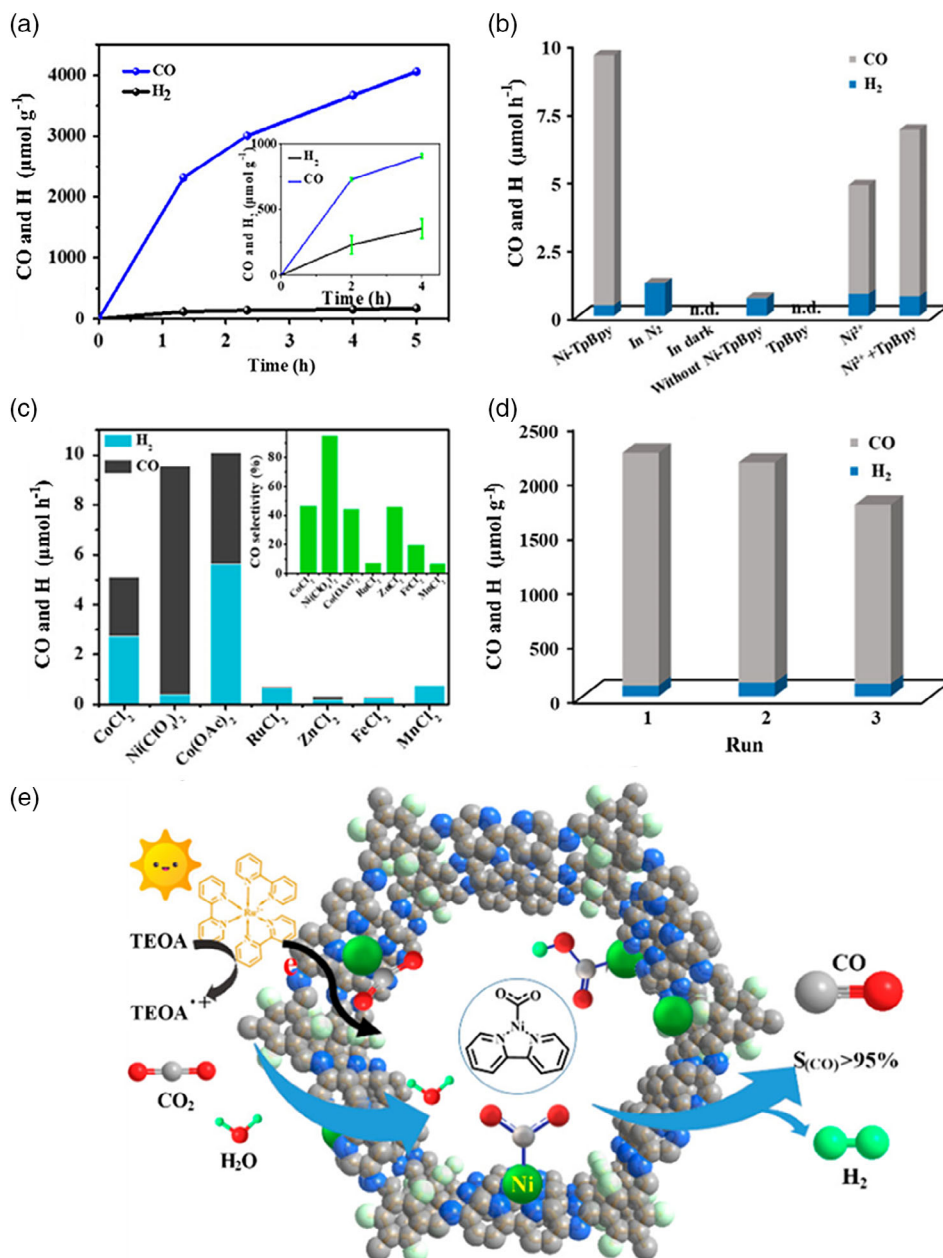
Figure 10. a) Photocatalytic evolutions of CO and H_2 by Ni-TpBpy under 1 and 0.1 atm (diluted with Ar, inset). b, c) CO and H_2 yields at different conditions in a 2 h reaction. d) Stability tests of Ni-TpBpy for photoreduction of CO_2. e) Schematic diagram photocatalytic CO_2 reduction over Ni-TpBpy. Reproduced with permission.[214] Copyright 2019, American Chemical Society.

reduction.[241] The catalytic system retained a cobalt-based turnover number of 90 for CO generation over 60 h (**Figure 13b**).

Re(bpy)(CO)$_3$Cl is another effective complex cocatalyst, which has been incorporated into a 2D COF structure.[164] The resulting hybrid photocatalysts can reduce CO_2 to CO under visible light irradiation with remarkable selectivity (98%), surpassing its comparable Re counterpart. The system was observed to undergo facile intramolecular charge transfer (ICT) through ET from photoexcited COF to Re moieties. Three key intermediate species were proposed to be responsible for CS, induction period, and rate determining step in CO_2 reduction (**Figure 14**).

4.5. Heterojunction Construction

Coupling metal-free materials with other semiconductors to form a heterojunction provides another effective strategy to promote charge carrier transfer and separation through the interfaces between the semiconductors with matching band potentials. **Table 7** gives recent results on the photocatalytic reduction of CO_2 by nonmetallic material-based heterojunctions. In terms of band position of the two semiconductors, three categories can be classified as shown in **Figure 15**.[278] Among them, the type II heterostructure, which is called staggered bandgap,
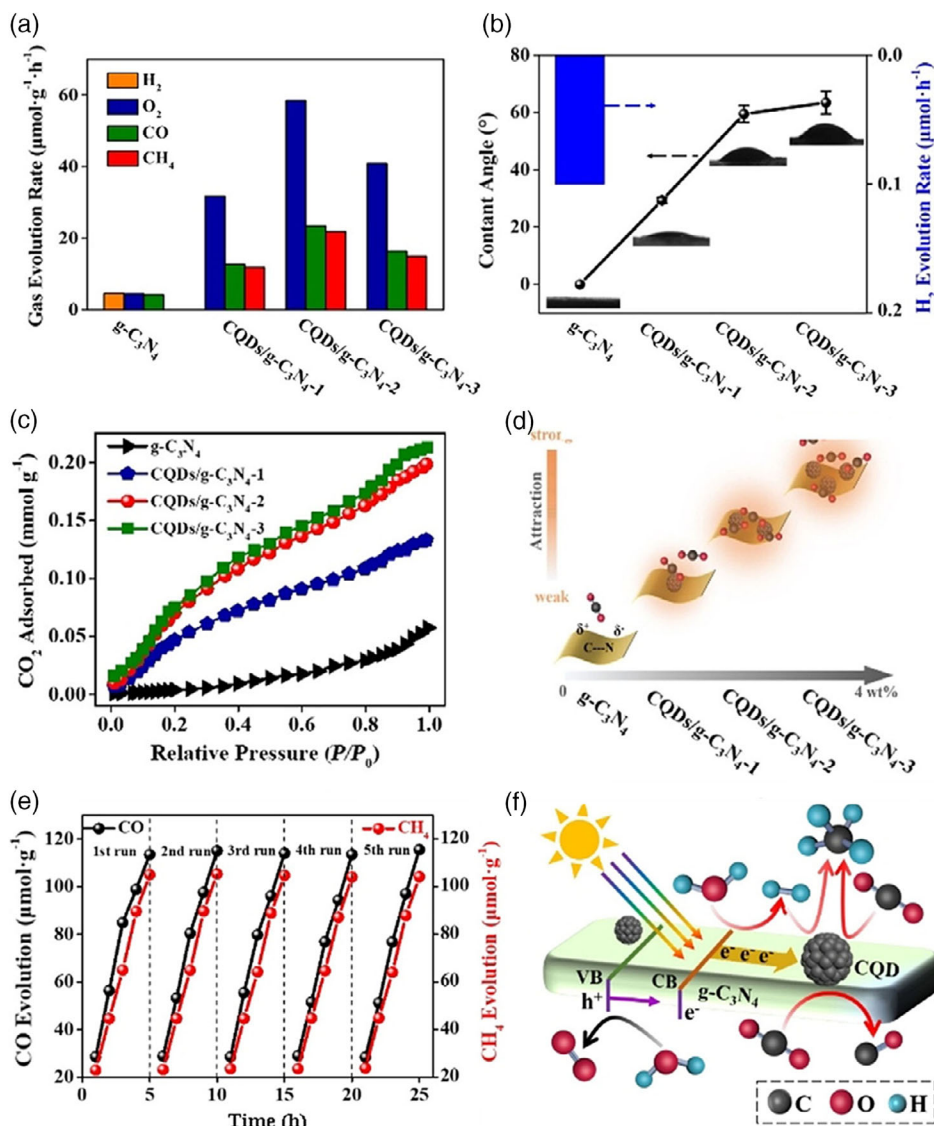
Figure 11. a) CH$_4$, CO, O$_2$, and H$_2$ photogeneration rates of different samples under visible-light irradiation ($\lambda > 400$ nm). b) Contact angle and H$_2$ generation rates of g-C$_3$N$_4$ and CQDs/g-C$_3$N$_4$. The inserts are the contact angle images for droplets water on different samples. c) CQDs doping content dependent CO$_2$ adsorption at room temperature for g-C$_3$N$_4$. d) Corresponding schematic diagrams of their surface attraction for CO$_2$. e) Cycling measurements of CO and CH$_4$ photoevolution of 2% CQDs/g-C$_3$N$_4$ under visible-light irradiation ($\lambda > 400$ nm). f) Schematic illustration of the photocatalytic process for CO$_2$ reduction on CQDs/g-C$_3$N$_4$. Reproduced with permission.[225] Copyright 2018, WILEY-VCH.

is the most desirable one because it favors efficient charge carrier separation, thus affording improved activity. As such, the type II heterostructure in CO$_2$ photocatalytic reduction is highlighted.

Assembly of CdS NPs on BCN[144] with suitable band alignment enabled the formation of a type II heterostructure. The hybrid catalyst provided a tenfold increase in CO$_2$ reduction performance, exhibiting a CO yield rate of 250 μmol h^{-1} g^{-1}. Coupling of 0D CdSe QDs and 2D polymeric C$_3$N$_4$ (p-C$_3$N$_4$) nanosheets to create a type II heterojunction (p-CNCS) was observed to enhance charge carrier separation and reduce their diffusion length (**Figure 16**).[257] Controlling the size of CdSe allowed one to improve CH$_3$OH generation through inhibition of H$_2$ evolution by adjusting E_{CB} to an appropriate level,

that is, below $E(H^+/H_2)$, whereas above $E(CO_2/CH_3OH)$ (Figure 16c–f). The relationship between band energy tuned by modulating CdSe size and photocatalytic performance were also further explored.

The polyoxometalates [Co$_4$]@g-C$_3$N$_4$ hybrid with staggered band alignment enabled visible-light-driven photocatalytic CO$_2$ reduction, delivering a yield of 107 μmol g^{-1} h^{-1} with reasonable selectivity (94%) for CO generation.[258] The presence of Co$_4$ was found to facilitate surface charge transfer in g-C$_3$N$_4$ and also enhance its surface catalytic oxidative capaability.

Integrating nanosheets of NiAl–LDH with positive charge and g-C$_3$N$_4$ with negative charge permitted the yield of a 2D/2D hybrid heterojunction.[268] This kind of heterojunction displayed

Table 6. Summary of the recent results on the photocatalytic reduction of CO_2 by nonmetallic-based materials with metal complex cocatalysts.

| Photocatalyst (Cocatalyst)	Synthetic method [Precursor]	Reaction medium	Illumination [Performance]	Ref.
g-C_3N_4 (Ru complex)	Thermal polymerization and adsorption method (550 °C, 4 h)	$NaNO_2$	$\lambda > 400$ nm (400 W Hg); HCOOH: 1854 nmol	[232]
	(CH_2N_2, NH_4HF_2, and trans(Cl)-[Ru{4,4'-($CH_2PO_3H_2$)2-2,2'-bipyridine})			
C_3N_4 (Ru(II) complex)	Thermal polymerization and adsorption method (550 °C, 4 h)	$NaNO_2$	$\lambda > 400$ nm (400 W Hg); CO: 455 nmol	[233]
	(CH_2N_2, NH_4HF_2, and trans(Cl)-[Ru{4,4'-($CH_2PO_3H_2$)2-2,2'-bipyridine})			
C_3N_4 (Ru complex)	Thermal polymerization and adsorption method (550 °C, 4 h)	$NaNO_2$	$\lambda > 400$ nm (400 W Hg); HCOOH: 8.8 nmol	[234]
	(CH_2N_2, NH_4HF_2, and trans(Cl)-[Ru {4,4'-($CH_2PO_3H_2$)2-2,2'-bipyridine})			
C_3N_4 (Ru(II) complex)	Thermal polymerization and copolymerization method (550 °C, 2 h)	C_2H_3N	$\lambda > 400$ nm (400 W Hg); HCOOH: 2.0 μmol	[235]
g-C_3N_4 (Zr MOF)	Self-assembly synthesis (550 °C, 4 h and 120 °C, 48 h)	Water	800 nm $> \lambda > 400$ nm (300 W Xe); CO: 59.4 μmol g^{-1}; Stability: decrease	[236]
	($C_3H_6N_6$, $ZrCl_4$, $C_{16}H_{22}O_4$ and C_3H_7NO)			
C_3N_4 (Co-porphyrin)	Thermal treating method (550 °C, 4 h)	MeCN	800 nm $> \lambda > 400$ nm (300 W Xe); CO: 17 μmol g^{-1}; AQY@420 nm: 0.8%; Stability: decrease	[237]
	($C_3N_6H_6$, $MgSO_4$ and $CoCl_2$)			
g-C_3N_4 (boron imidazolate framework)	Electrostatic self-assembly approach (550 °C, 4 h)	MeCN	800 nm $> \lambda > 400$ nm (300 W Xe); CO: 53.87 μmol g^{-1} h^{-1}; Stability: decrease	[238]
	($C_3N_6H_6$, KBH(mim)$_3$, Zn(NO_3)$_2$·$6H_2O$, and 4,4'-oxybisbenzoic acid)			
g-C_3N_4 (Ir complex)	Thermal treating method (550 °C, 4 h)	Water	$\lambda > 400$ nm (300 W Xe); CH_3OH: 9934 μmol g^{-1}	[231]
	($C_2H_4N_4$ and [(bpy)2Ir(μ-Cl)]2, 2-(1 H-tetrazol-5-yl) pyridine)			
g-C_3N_4 (FeTCPP)	Thermal polymerization and mechanical mix method (550 °C, 4 h)	Water	780 nm $> \lambda > 420$ nm (300 W Xe, 220 mW cm^{-2}); CO: 6.52 mmol g^{-1}; Stability: decrease	[239]
	($C_2H_4N_4$, tetra(4-carboxyphenyl) porphyrin and $FeCl_3$)			
C_3N_4 (Fe Quaterpyridine)	Thermal polymerization method (550 °C, 4 h)	Water	$\lambda > 400$ nm (400 W Hg); CO: 54 μmol; AQY@400 nm: 4.2%; Stability: decrease	[240]
	(CH_2N_2, NH_4HF_2, and $FeCl_3$)			
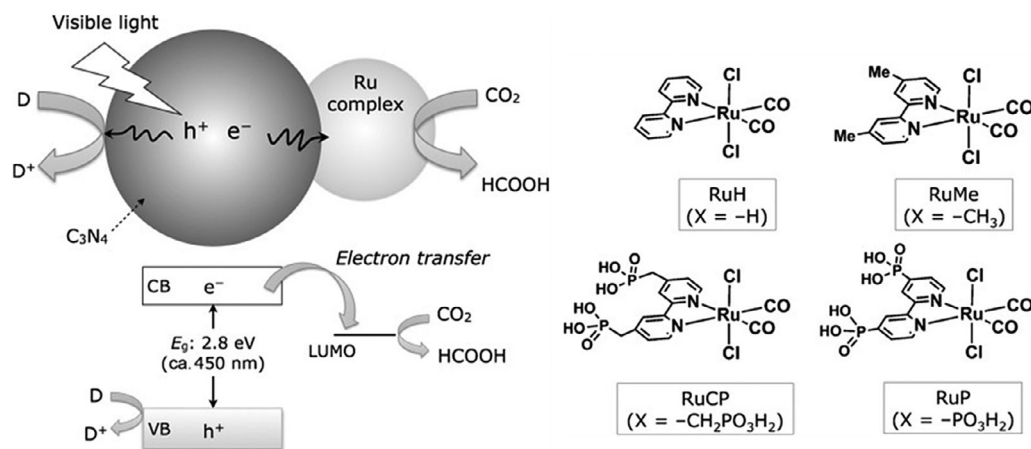
Figure 12. CO_2 reduction using a Ru complex/C_3N_4 hybrid photocatalyst, along with structures of the Ru complexes used. Reproduced with permission.[234] Copyright 2015, WILEY-VCH.
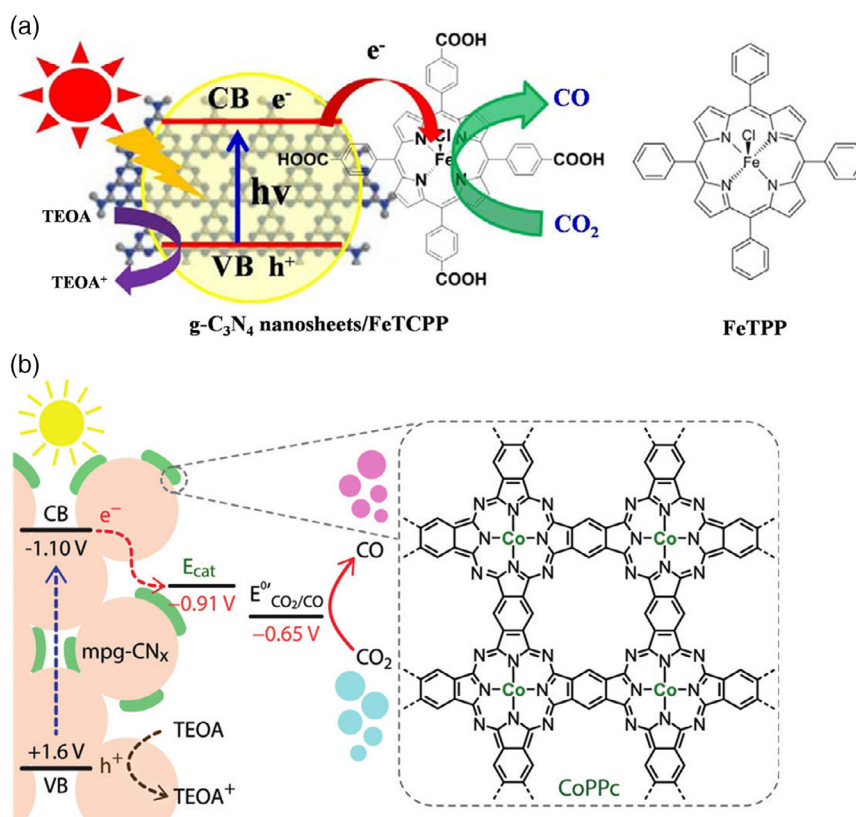
Figure 13. a) Structure of g-C$_3$N$_4$/FeTCPP and FeTPP. Reproduced with permission.[239] Copyright 2018, Elsevier. b) Schematic illustration of light-driven CO$_2$ reduction catalyzed by mpg-CNx/CoPPc (potentials reported against NHE). Reproduced with permission.[241] Copyright 2019, WILEY-VCH.

good capability for photocatalytic CO$_2$ reduction to generate hydrocarbons, which could be mainly formed from the intimate interfacial contact at the 2D/2D heterostructure, which inhibited recombination of charge carriers and improved their transfer and separation.

4.6. Z-Scheme

An artificial Z-scheme structure tends to increase the photocatalytic performance because of multiple merits, including extended light-harvesting range, effective electron/hole pair separation efficiency, simultaneous preservation of sufficient redox capability as well as unique charge transfer.[279] **Table 8** presents the recent work on metal-free-based Z-scheme photocatalysis of CO$_2$ reduction. Z-scheme photocatalysts are mainly divided into three categories, as shown in **Figure 17**. In conventional Z-scheme photocatalysts, a redox ionic couple (e.g., Fe^{3+}/Fe^{2+}, IO^{3-}/I$^-$, and [Co-(bpy)$_3$]$^{3+/2+}$/[Co(phen)$_3$]$^{3+/2+}$) is used to serve as an electron mediator. In all-solid-state Z-scheme photocatalysts, an electron conductor (e.g., Au, Ag) is utilized to promote charge carrier transport. In direct Z-scheme photocatalysts, the close contact between two semiconductors can ensure an internal electric field to accelerate charge carrier transfer.[305] In the following, special attention is given to direct Z-scheme and all-solid-state Z-scheme

in photocatalytic CO$_2$ reduction using metal-free-based photocatalysts.

4.6.1. Direct Z-Scheme

The concept of direct Z-scheme dates back to 2013. Since then, a number of metal-free material-based Z-scheme photocatalysts were constructed and utilized in the field of CO$_2$ reduction.[306] Self-assembly of MoS$_2$ monolayer onto the surface of SiC NPs resulted in a marigold-like SiC@MoS$_2$ nanoflower heterostructure (**Figure 18**).[293] The as-obtained photocatalyst gave a high CH$_4$ yield rate (323 μL g^{-1} h^{-1}) (Figure 18f). It was proposed that the Z-scheme charge transfer resulting from the combination of the electrons in MoS$_2$ and the holes in SiC ensured efficient utilization of photoinduced electrons in SiC (Figure 18g).

Hybridization of a Ru(II) binuclear complex (RuRu′) containing photosensitizer with mesoporous g-C$_3$N$_4$ enabled an artificial Z-scheme system, which was reported to drive visible-light photocatalytic reduction of CO$_2$ to yield HCOOH.[294] The RuRu′/Ag/C$_3$N$_4$ hybrid showed a turnover number >3000 (based on the mass of RuRu′) with a selectivity in the range 87–99% for HCOOH production. Notably, although g-C$_3$N$_4$ is intrinsically hydrophobic and CO$_2$ has low solubility in water, the hybrid catalyst still exhibited reasonable aqueous photocatalytic efficiency with addition of a proper electron donor.
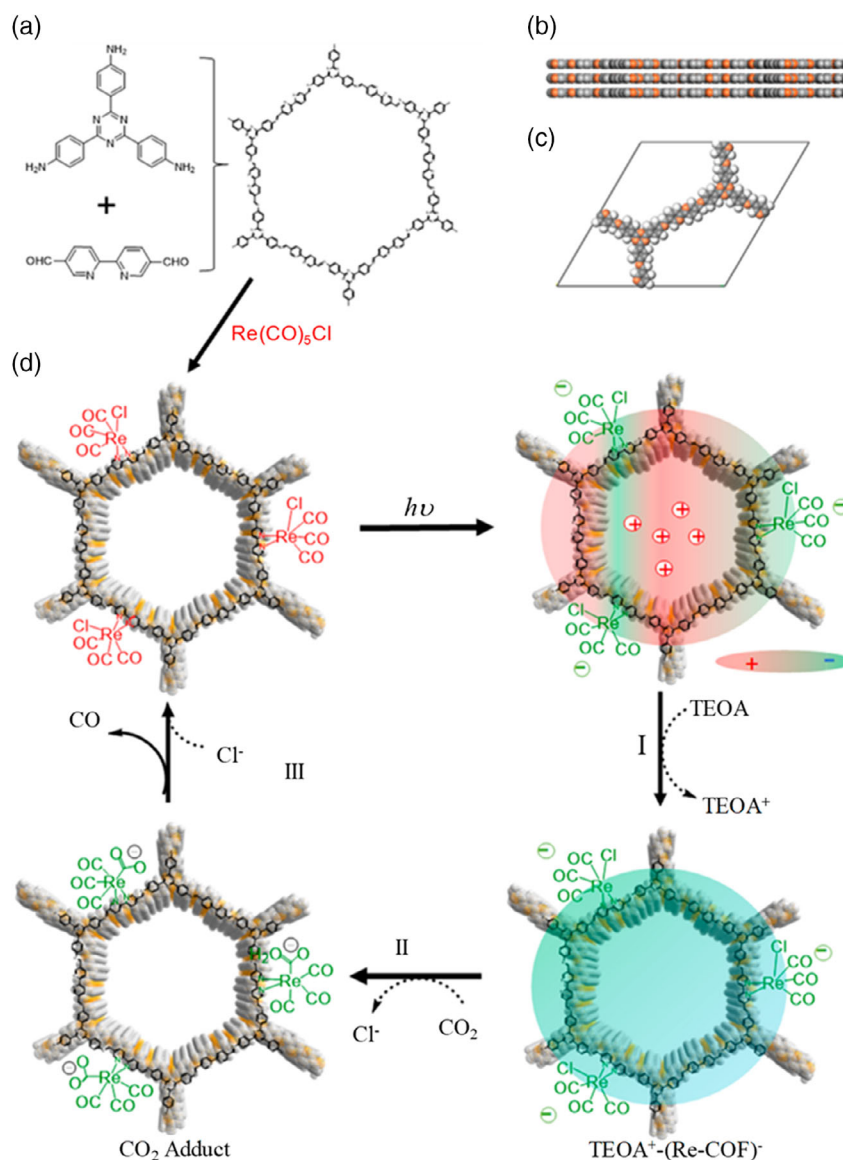
ADVANCED
SCIENCE NEWS
www.advancedsciencenews.com

Solar
RRL
www.solar-rrl.com

Figure 14. a) Synthesis of COF and Re-COF. b) Side view and c) unit cell of AA stacking COF. d) Proposed catalytic mechanism for CO_2 reduction. Reproduced with permission.[164] Copyright 2019, American Chemical Society.

4.6.2. All-Solid-State Z-Scheme

In an all-solid-state Z-scheme photocatalytic structure, the electron mediator is crucial because it can promote migration of charge carriers and simultaneouly increase the photocatalytic stability. For instance, an Au@g-C_3N_4/SnS Z-scheme yolk-shell photocatalyst was designed and synthesized using Au as a charge transport bridge through a template-assisted method.[297] Au in the photocatalyst also behaved as an ET mediator to boost CO_2 reduction. Specifically, the electrons in the CB of SnS recombined with the holes in the VB of g-C_3N_4 in the metallic Au, thus effectively promoting their separation (**Figure 19**a). A g-C_3N_4/α-Fe_2O_3 Z-scheme nanocomposite was also synthesized for efficient photocatalytic CO_2 reduction.[299] The remarkable performance was explained by the enhanced charge carrier transport and separation as a result of the formation of g-C_3N_4/α-Fe_2O_3 heterojunction and the Al-O bridges (Figure 19b).

Apart from metal NPs, reduced graphene oxide (rGO) is also an alternative electron mediator to construct a Z-scheme structure.[301,302] For example, an urchin-like Z-scheme photocatalyst (LDH/RGO/CN) was fabricated by hydrothermal synthesis of CoZnAl-LDH with in situ incorporation of g-C_3N_4 and rGO (**Figure 20**a–c).[303] The resulting LDH/RGO/CN-enabled effective photocatalytic CO_2 reduction selectively to CO (Figure 20d). Photoexcited electrons from the CB of LDH migrated to the rGO layer and were further transferred to the VB of g-C_3N_4, thereby enhancing charge carrier separation (Figure 20e).

Table 7. Summary of the photocatalytic CO_2 reduction activity of metal-free-based heterojunction photocatalysts.

Photocatalyst	Synthetic method [Precursor]	Reaction medium	Illumination [Performance]	Ref.
Red phosphorus/ g-C_3N_4	Thermal polymerization and annealing method (550 °C, 4 h and 380 °C, 2 h)	Water	Simulated sunlight (500 W Xe);	[242]
	(CH_4N_2O and red phosphor)		CH_4: 295 µmol h^{-1} g^{-1} (0.5 wt% Pt)	
BP/g-C_3N_4	Electrostatic attraction approach (500 °C, 3 h)	Water vapor	Simulated sunlight (300 W Xe);	[153]
	(CH_4N_2S and black phosphorus)		CO: 6.54 µmol h^{-1} g^{-1} (0.5 wt% Pt)	
B_4C/g-C_3N_4	Solvent evaporation method (550 °C, 4 h and 90 °C, 2 h)	Water	723 nm $> \lambda >$ 405 nm (300 W Xe); CH_4: 0.84 µmol h^{-1} g^{-1} (0.8 wt% Pt);	[243]
	(CH_4N_2O and B_4C)		Stability: decrease	
In_2O_3/g-C_3N_4	Thermal polymerization and hydrothermal method (500 °C, 2 h and 180 °C, 12 h)	Water	Simulated sunlight (500 W Xe, 1200 mW cm^{-2});	[244]
	($C_3N_6H_6$ and $In(Ac)_3$)		CH_4: 159.2 ppm (0.5 wt% Pt);	
			Stability: >16 h	
Mg-Al-LDH/ g-C_3N_4	Thermal polymerization and self-assembly method (550 °C, 4 h)	Water	Simulated sunlight (500 W Xe);	[245]
	(CH_4N_2O, $Mg(NO_3)_2 \cdot 6H_2O$, $Al(NO_3)_3 \cdot 9H_2O$, and Na_2CO_3)		CH_4: 6.5 µmol (0.5 wt% Pd); AQY@420 nm: 0.093%	
CeO_2/g-C_3N_4	Hard-template route (550 °C, 3 h)	Water vapor	Simulated sunlight (300 W Xe);	[246]
	(CH_4N_2O, $Ce(NO_3)_3 \cdot 6H_2O$)		CH_4: 2.3 µmol h^{-1} g^{-1}	
ZnO/g-C_3N_4	Impregnation method (550 °C, 4 h)	Water	Simulated sunlight (500 W Xe, 175 mW cm^{-2});	[247]
	(CH_4N_2O, $Zn(OOCCH_3)_2 \cdot 2H_2O$)		CO: 45.6 µmol h^{-1} g^{-1};	
			Stability: decrease	
AgCl/g-C_3N_4	Deposition-precipitation method (520 °C, 2.5 h)	Water	650 nm $> \lambda >$ 400 nm (15 W daylight lamp, 8.5 mW cm^{-2});	[248]
	(CH_4N_2O, NaCl, and $AgNO_3$)		CH_4: 0.525 µmol g^{-1};	
			AQY@420 nm: 0.085%;	
			Stability: decrease	
AgX/g-C_3N_4	Sonication-assisted deposition-precipitation method (520 °C, 2.5 h)	Water	$\lambda >$ 400 nm (15 W daylight lamp, 8.5 mW cm^{-2});	[249]
(X = Cl and Br)	(CH_4N_2O, $AgNO_3$, and NaCl or NaBr)		CH_4: 10.92 µmol g^{-1} h^{-1};	
			Stability: >40 h	
TiO_2/g-C_3N_4	Mechanical mixing method (520 °C, 2 h and 450 °C, 2 h)	Water	$\lambda =$ 254 nm (8 W Hg, 0.5 mW cm^{-2});	[250]
	($C_3N_6H_6$ and P25)		CH_4: 9 µmol g^{-1} h^{-1}	
TiO_2/g-C_3N_4	Thermal polymerization and calcination method (500 °C, 4 h and 450 °C, 2 h)	Water	$\lambda \geq$ 420 nm (300 W Xe);	[251]
	($C_2H_4N_4$, $Ti(OBu)_4$ and HNO_3)		CH_4: 175 µmol h^{-1} g^{-1} (1 mM Pt)	
TiO_2/g-C_3N_4	Hydrothermal in-situ growth method (560 °C, 4 h and 180 °C, 24 h)	Water vapor	$\lambda >$ 325 nm (150 W Xe);	[252]
	($C_3N_6H_6$, $Ti(OBu)_4$ and HF)		CO: 2.06 µmol h^{-1} g^{-1};	
			Stability: decrease	
TiO_{2-x}/g-C_3N_4	In-situ pyrolysis method (550 °C, 3 h and 150 °C, 24 h)	MeCN	$\lambda >$ 400 nm (300 W Xe);	[253]
	($C_3N_6H_6$, NH_2-BDC, and $C_{12}H_{28}O_4Ti$)		CO: 77.8 µmol h^{-1} g^{-1};	
			Stability: decrease	

Table 7. Continued.

Photocatalyst	Synthetic method [Precursor]	Reaction medium	Illumination [Performance]	Ref.
TiO_2/B-g-C_3N_4	Ionic liquids method (550 °C, 3 h, 350 °C, 2 h, and 550 °C, 4 h) ($C_2H_4N_4$ and $BmimBF_4$)	MeCN	$\lambda > 400$ nm (300 W Xe); CH_4: 66.25 µmol g^{-1} h^{-1}	[254]
$CdMoO_4/g$-C_3N_4	Mixing-calcination method (520 °C, 4 h and 400 °C, 2 h) ($C_3N_6H_6$, $Na_2MoO_4\cdot2H_2O$, $Cd(NO_3)_2\cdot4H_2O$)	Water	Simulated sunlight (500 W Xe); CO: 25.8 µmol h^{-1} g^{-1}	[255]
$LaPO_4/g$-C_3N_4	In-situ hydrothermal method (520 °C, 4 h and 160 °C, 20 h) ($C_3H_6N_6$, $La(NO_3)_3\cdot6H_2O$, and $(NH_4)_2HPO_4$)	Water vapor	Simulated sunlight (300 W Xe); CO: 14.4 µmol g^{-1} h^{-1}; Stability: decrease	[90]
$CdIn_2S_4/g$-C_3N_4	Hard-template and hydrothermal method (550 °C, 4 h and 160 °C, 16 h) (Silica SBA-15, CH_2N_2, $CdCl_2\cdot2.5H_2O$, and $InCl_3\cdot4H_2O$)	NaOH	$\lambda \geq 420$ nm (300 W Xe); CH_3OH: 42.7 µmol g^{-1} h^{-1}; AQY@420 nm: 0.14%; Stability: decrease	[256]
$CdSe/g$-C_3N_4	Impregnation and calcination method (550 °C, 4 h and 80 °C, 24 h) ($CdCl_2$, $C_3H_6O_2S$, $C_2H_4N_4$, and Se)	KHCO$_3$	$\lambda \geq 420$ nm (300 W Xe, 0.42 mW cm^{-2}); CH_3OH: 186.4 µmol h^{-1} g^{-1}; AQY@420 nm: 0.91%; Stability: decrease	[257]
Co4@g-C_3N_4	Thermal polymerization and hydrothermal method (550 °C, 2.5 h and 150 °C, 12 h) (CH_4N_2O)	MeCN	$\lambda \geq 420$ nm (300 W Xe); CO: 107 µmol g^{-1} h^{-1}; Stability: decrease	[258]
$CsPbBr_3/g$-C_3N_4	Thermal polymerization and self-assembly method (550 °C, 2 h) ($C_3H_6N_6$, $PbBr_2$, and $CsCO_3$)	Water	$\lambda \geq 420$ nm (300 W Xe); CO: 149 µmol h^{-1} g^{-1}; Stability: decrease	[259]
NiO/g-C_3N_4	Hydrothermal deposition and calcination method (520 °C, 4 h and 180 °C, 12 h) (CH_4N_2O and $Ni(NO_3)_2\cdot6H_2O$)	Water	Simulated sunlight (300 W Xe); CO: 4.17 µmol h^{-1} g^{-1}; Stability: decrease	[260]
ZnV_2O_6/g-C_3N_4	Thermal treatment and solvothermal method (550 °C, 3 h and 200 °C, 24 h) ($C_3H_6N_6$, C_3H_7NO, NH_4VO_3 and $Zn(O_2CCH_3)_2$)	NaOH	Simulated sunlight (35 W HID Xe, 20 mW cm^{-2}); CH_3OH: 374.2 µmol h^{-1} g^{-1}; AQY@420 nm: 0.081%; Stability: >32 h	[261]
C-$Cu_{2-x}S/g$-C_3N_4	Calcination and solvothermal method (700 °C, 2 h and 150 °C, 12 h) (CH_3CSNH_2, HKUST-1 and CH_4N_2O)	Water vapor	$\lambda \geq 420$ nm (300 W Xe); CO: 88.5 µmol h^{-1} g^{-1}; Stability: decrease	[262]
Sb-SnO_2/g-C_3N_4	Thermal treatment method (550 °C, 4 h and 400 °C, 2 h) ($SnCl_4\cdot2H_2O$, $SbCl_3\cdot2H_2O$, and $C_3H_6N_6$)	MeCN	$\lambda \geq 420$ nm (300 W Xe); CO: 4.49 µmol g^{-1} h^{-1}; Stability: decrease	[263]

Table 7. Continued.

Photocatalyst	Synthetic method [Precursor]	Reaction medium	Illumination [Performance]	Ref.
Cu-TiO$_2$/g-C$_3$N$_4$	NaBH$_4$ reduction and calcination method (550 °C, 4 h and 400 °C, 2 h) (NaBH$_4$, Cu(Ac)$_2$·H$_2$O, P25, and CH$_4$N$_2$O)	Water vapor	$\lambda > 400$ nm (300 W Xe, 197 mW cm^{-2}); CH$_4$: 23.88 μmol h^{-1} g^{-1}; Stability: decrease	[264]
Cu-CNTs/pCN	Sonicated assisted chemical method (550 °C, 2 h) (C$_3$H$_6$N$_6$, Carbon nanotubes, and Cu(NO$_3$)$_2$·3H$_2$O)	Water	Simulated sunlight (solar simulator, 100 mW cm^{-2}); CO: 560 μmol h^{-1} g^{-1}; Stability: decrease	[265]
CN/rGO	Ionothermal method (500 °C, N$_2$ atmosphere, 4 h and 550 °C, 4 h) (C$_3$H$_6$N$_6$, GO, KCl, and LiCl)	Water vapor	Simulated sunlight (350 W Xe, AM 1.5 filter); CO: 12.63 μmol h^{-1} g^{-1}; AQY@420 nm: 0.254%; Stability: decrease	[266]
g-C$_3$N$_4$@CeO$_2$	Thermal treatment method (550 °C, 4 h and 500 °C, 6 h) (CH$_2$N$_2$, Ce (NO$_3$)$_3$·6H$_2$O, and C$_6$H$_{12}$N$_4$)	Water vapor	$\lambda \geq 420$ nm (300 W Xe); CO: 5.6 μmol h^{-1} g^{-1}; AQY@420 nm: 17.1%	[267]
g-C$_3$N$_4$/NiAl-LDH	In situ hydrothermal method (550 °C, 4 h and 120 °C, 24 h) (C$_3$H$_6$N$_6$, Ni(NO$_3$)$_2$·6H$_2$O, and Al(NO$_3$)$_3$·9H$_2$O)	Water vapor	$\lambda \geq 420$ nm (300 W Xe); CO: 8.2 μmol h^{-1} g^{-1}; AQY@420 nm: 0.21%; Stability: decrease	[268]
g-C$_3$N$_4$/NaNbO$_3$	Hydrothermal and calcination method (200 °C, 24 h and 520 °C, 4 h) (EO$_{20}$PO$_{70}$EO$_{20}$, Nb(OC$_2$H$_5$)$_5$, and C$_3$H$_6$N$_6$)	Water	Simulated sunlight (300 W Xe); CH$_4$: 6.4 μmol h^{-1} g^{-1} (0.5% Pt)	[269]
PC$_3$N$_4$/ZnIn$_2$S$_4$	Thermal treatment and hydrothermal method (550 °C, 4 h and 80 °C, 1 h) (CH$_4$N$_2$O, ZnCl$_2$, InCl$_3$·3H$_2$O, and CH$_3$CSNH$_2$)	Water	$\lambda \geq 420$ nm (300 W Xe); CO: 892 μmol h^{-1} g^{-1}; AQY@420 nm: 2.4%; Stability: >40 h	[270]
g-C$_3$N$_4$/Cu$_2$O	Thermal treatment and photodeposition method (550 °C, 4 h and 300 W Hg, 3 h) (C$_3$H$_6$N$_6$ and CuSO$_4$·5H$_2$O)	Water	780 nm $\geq \lambda \geq$ 350 nm (300 W Xe); CO: 8.18 μmol h^{-1} g^{-1}; Stability: decrease	[271]
g-C$_3$N$_4$/CoPc-COOH	Thermal polymerization and mechanical mix method (550 °C, 4 h) (C$_9$H$_4$0$_5$, CH$_4$N$_2$O, CoCl$_2$, and (NH$_4$)$_2$MoO$_4$)	Water	$\lambda > 400$ nm (20 W LED); CH$_3$OH: 538.8 μmol h^{-1} g^{-1}; AQY@515 nm: 1.232%; Stability: decrease	[272]
g-C$_3$N$_4$-N-TiO$_2$	Thermal treatment method (550 °C, 3 h and 580 °C, 3 h) (CH$_4$N$_2$O, Ti(OH)$_4$, and Ti(SO$_4$)$_2$)	Water vapor	Simulated sunlight (300 W Xe); CO: 12.3 μmol h^{-1} g^{-1}; AQY@420 nm: 0.91%; Stability: > 36 h	[273]
g-C$_3$N$_4$/Ag-TiO$_2$	Solvent evaporation and calcination method (550 °C, 2.5 h and 400 °C, 1 h) (CH$_4$N$_2$O, P25, AgNO$_3$, and NaBH$_4$)	Water vapor	Simulated sunlight (300 W Xe); CH$_4$: 9.33 μmol g^{-1} h^{-1}	[274]

1900546 (24 of 41)

Table 7. Continued.

| Photocatalyst	Synthetic method [Precursor]	Reaction medium	Illumination [Performance]	Ref.
g-C$_3$N$_4$/(Cu/TiO$_2$)	Thermal treatment method (550 °C, 3 h and 400 °C, 1 h)	NaOH	Simulated sunlight (500 W Xe);	[275]
	(C$_3$H$_6$N$_6$, Cu(NO$_3$)$_2$·3H$_2$O and TiO$_2$)		HCOOH: 633.6 μmol g^{-1} h^{-1};	
			Stability: decrease	
g-C$_3$N$_4$/Bi$_2$O$_2$CO$_3$/ CoFe$_2$O$_4$	Thermal treatment and hydrothermal method (520 °C, 3 h and 180 °C, 12 h) (CH$_4$N$_2$O, Na$_2$CO$_3$, Bi(NO$_3$)H$_2$O, Co(NO$_3$)$_2$, and Fe(NO$_3$)$_3$)	Water	λ ≥ 400 nm (880 W Xe); CO: 16.38 μmol h^{-1} g^{-1}; Stability: >36 h	[276]
CdS/boron carbon nitride (BCN)	Thermal treatment and photodeposition method (1250 °C, 5 h and 180 °C, 12 h)	Water	λ ≥ 420 nm (300 W Xe);	[144]
	(H$_3$BO$_3$, H$_2$NCONH$_2$, S$_8$, and CdCl$_2$·2.5H$_2$O)		CO: 250 μmol h^{-1} g^{-1}; Stability: decrease	
Bi$_4$N$_b$O$_8$Cl/g-C$_3$N$_4$	Ball-milling and calcination method (400 °C, 3 h)	NaHCO$_3$ and H$_2$SO$_4$	Simulated sunlight (300 W Xe);	[277]
	(Bi$_2$O$_3$, Nb$_2$O$_5$, BiOCl, KCl, NaCl, and melamine)		CO: 2.26 μmol g^{-1} h^{-1}; Stability: >4 h	
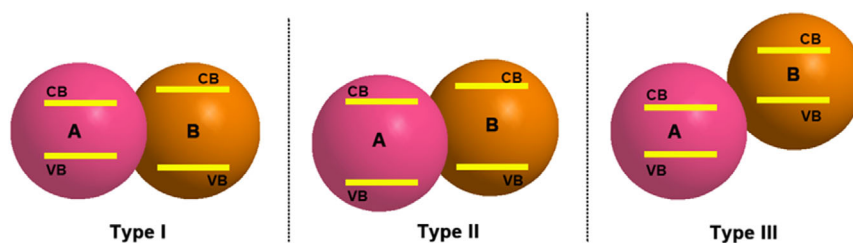
Figure 15. Different types of semiconductor heterojunctions.[278]

5. Mechanistic Insight into Photocatalytic CO$_2$ Reduction over Metal-Free Catalysts

Mechanistic understanding of photocatalytic CO$_2$ conversion facilitates insights into the complex reaction kinetics and also aid rational design of active and selective photocatalysts. To this end, the development of advanced characterization techniques is believed to provide useful information to unveil molecular structure–performance relationships during the photocatalytic reaction. In addition, isotope labelling and DFT calculations also help to clarify reaction pathways and mechanisms.

5.1. Isotope Labeling

Isotope labeling provides an effective approach to deduce plausible reaction pathways and identify origin of reaction products, aiding mechanistic understanding. Isotopic experiments using ^{13}CO$_2$, D$_2$O or H$_2$^{18}O, together with gas chromatography/mass spectrometry (GC–MS) need be monitored to corroborate the source of produced monoxide, alcohols or hydrocarbons.[307] This technique is significant especially to those photocatalysts derived from carbon-containing precursors. Isotope labeling

has been applied to explore the carbon origin of HCOOH product during photocatalytic CO$_2$ reduction over copolymerized carbon nitride (NS-C$_3$N$_4$) with Ru(II) complex as a photosensitizer and TEOA as a hole scavenger.[235] Using ^{13}CO$_2$ as a feed gas, a doublet ($J^{13}$$_{CH}$ = 188 Hz) appeared at 8.63 and 8.16 ppm, suggesting the yied of H^{13}COOH, as opposed to a singlet at 8.40 ppm originating from H^{12}COOH when using ^{12}CO$_2$ as a feed gas (**Figure 21**a). These results indicated that reaction products were evolved from CO$_2$ reduction. CO generated during the reaction was confirmed to originate from CO$_2$ by GC-MS measurements (Figure 21b). Similarly, CH$_4$ was corroborated as a product from CO$_2$ reduction over C$_3$N$_4$ (Figure 21c,d)[194] and boron (B)-doped C$_3$N$_4$ photocatalysts[308] based on isotope labeling measurements.

5.2. In situ Characterization

In situ/operando techniques enable one to detect reaction intermediates, identify predominant active centers, and monitor atomically the dynamic evolution of a catalyst's geometric structure and electronic environment, which gain increasing attention in catalysis.[309,310]
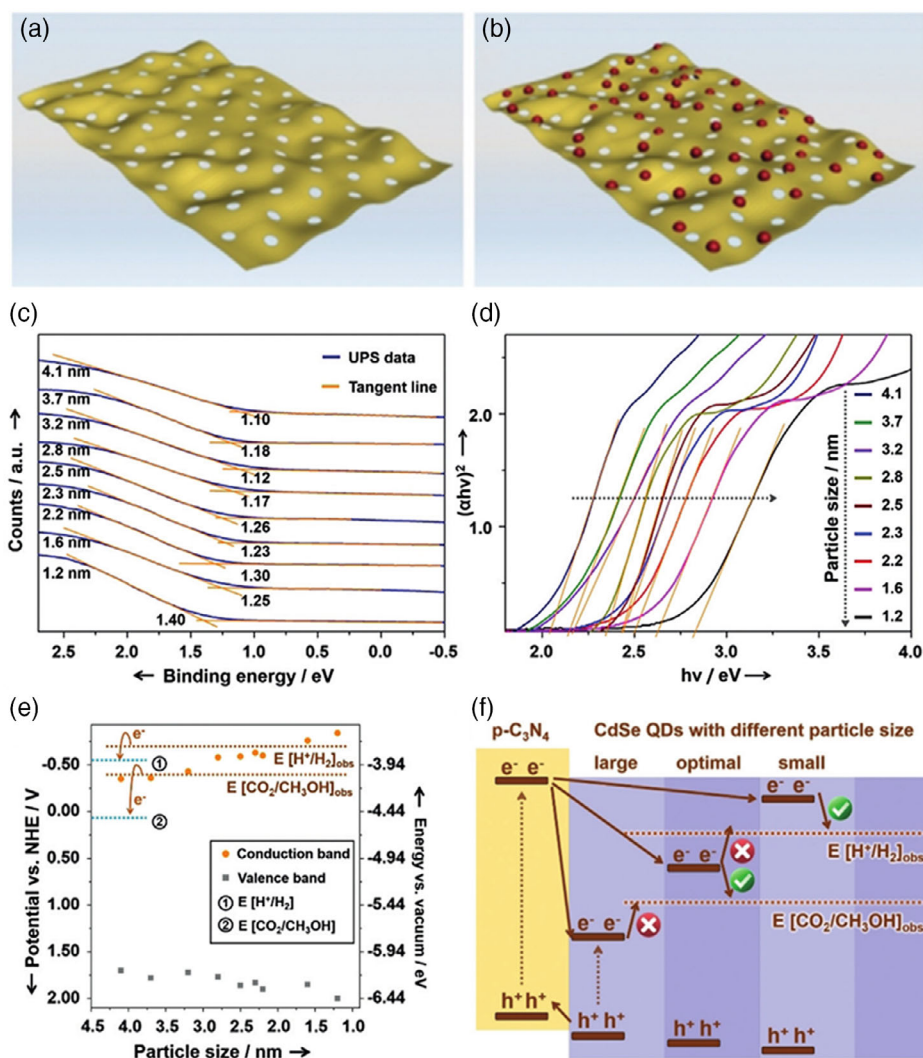
Figure 16. Model of a) p-C$_3$N$_4$ and b) p-CNCS. c) UPS data of CdSe QDs with different particle sizes. d) Relationship between (ahν)^2 and hν. e) Relative position of the reactive electrode potential and the energy band of the CdSe QDs with different particle sizes. f) Illustration of the variation tendencies of different p-CNCS. Reproduced with permission.[257] Copyright 2019, Wiley-VCH.

5.2.1. In situ DRIFTS

In situ DRIFTS can provide solid and decisive evidences on reaction-intermediate products and pathways during the CO$_2$ conversion, which helps one to explore reaction mechanisms. As shown in **Figure 22**a,b, for photocatalytic CO$_2$ reduction on g-C$_3$N$_4$ nanosheets (NS-CN),[185] the Fourier transform infrared (FTIR) bands at 1512, 1438, 1631, 1265, and 1048 cm^{-1} can be assigned to carbonate species, which originated from CO$_2$ and H$_2$O coadsorbed on NS-CN atomic layers, resulting in the formation of carbonates (CO$_3{}^{2-}$). Formate (bands at 1286, 1326, 1386, 1532, 1558, 1641, and 1695 cm^{-1}) and formaldehyde (bands at 1419, 1458, 1607, and 1657 cm^{-1}) appeared upon irradiation, and their amounts steadily increased along with decrease in carbonate species. Note that CH$_4$ molecules were detectable due to its nonpolar character and weak binding at the NS-CN surface. Furthermore, bands at 1732 and 1103 cm^{-1} matched well with

the vibration frequency of methoxy species arisng from methanol. All these results pointed to the possibility that the photocatalytic reduction of CO$_2$ to CH$_4$ and CH$_3$OH over NS-CN proceeded via multi-steps, encompassing intermediates of formic acid and for maldehyde.

Adsorbed and formed species over Ag$_2$CrO$_4$/g-C$_3$N$_4$/graphene nanocomposite in the process of CO$_2$ photoreduction were also investigated using in situ DRIFTS.[285] Bicarbonate (HCO$_3{}^-$, 1635 and 1420 cm^{-1}), bidentate carbonate (b-CO$_3{}^{2-}$, 1560 and 1310 cm^{-1}), and monodentate carbonate (m-CO$_3{}^{2-}$, 1510 and 1350 cm^{-1}) corresponding to adsorbed CO$_2$ species (Figure 22c) were detected in the dark. After being subjected to 60 min of irradiation, the peaks attributed to the adsorbed CO$_2$ species became weakened and multiple peaks were seen in the DRIFTS spectra, which could be ascribed to the bidentate formate species (COO$^-$) with bands at 1582, 1385, and 1353 cm^{-1}. The band intensity increased with extending irradiation time

Table 8. Summary of the photocatalytic CO_2 reduction activity of metal-free-based Z-scheme photocatalysts.

Photocatalyst	Synthetic method [Precursor]	Reaction medium	Illumination [Performance]	Ref.
Ag_3PO_4/g-C_3N_4	In situ deposition method (550 °C, 4 h and 500 W Xe, 1 h)	Water	$\lambda \geq 420$ nm (500 W Xe, 170 mW cm^{-2});	[280]
	(CH_4N_2O, $AgNO_3$, and Na_2HPO_4)		CO: 57.5 µmol h^{-1} g^{-1};	
			Stability: decrease	
SnO_{2-x}/g-C_3N_4	Thermal treatment method (520 °C, 4 h and 400 °C, 12 h, N_2)	Water vapor	Simulated sunlight (500 W Xe);	[281]
	($C_3H_6N_6$, $SnCl_2$, and KOH)		CO: 22.7 µmol h^{-1} g^{-1}	
$BiOI/g$-C_3N_4	Thermal treatment and deposition method (550 °C, 4 h)	Water vapor	$\lambda \geq 400$ nm (300 W Xe);	[282]
	(CH_4N_2O, $Bi(NO_3)_3$, and KI)		CO: 3.58 µmol h^{-1} g^{-1};	
			Stability: decrease	
MnO_2/g-C_3N_4	In-situ redox reaction (550 °C, 2 h and 40 °C, 12 h)	Water vapor	Simulated sunlight (300 W Xe, 230 mW cm^{-2});	[283]
	(CH_4N_2O, $KMnO_4$, and $MnSO_4 \cdot H_2O$)		CO: 9.6 µmol h^{-1} g^{-1};	
			Stability: >18 h	
α-Fe_2O_3/g-C_3N_4	Thermal treatment and hydrothermal method (550 °C, 4 h and 150 °C, 4 h)	Water	$\lambda \geq 420$ nm (300 W Xe, 0.42 mW cm^{-2});	[284]
	($C_2H_4N_4$ and $Fe(NO_3)_3 \cdot 9H_2O$)		CH_3OH: 5.63 µmol h^{-1} g^{-1}	
α-Fe_2O_3/g-C_3N_4	Impregnation-hydrothermal method (150 °C, 12 h)	$NaHCO_3$ and H_2SO_4	$\lambda \geq 420$ nm (300 W Xe, 0.21 W cm^{-2});	[93]
	(g-C_3N_4, $FeSO_4 \cdot 7H_2O$)		CO: 27.2 µmol h^{-1} g^{-1};	
			AQY@420 nm: 0.963%;	
			Stability: decrease	
Ag_2CrO_4/g-C_3N_4	Self-assembly precipitation method (520 °C, 2 h)	$NaHCO_3$ and HCl	$\lambda \geq 420$ nm (300 W Xe);	[285]
	(CH_4N_2O, GO, K_2CrO_4, and $AgNO_3$)		CH_4: 1.03 µmol h^{-1} g^{-1};	
			Stability: decrease	
$Cu_2V_2O_7/g$-C_3N_4	Calcination method (450 °C, 4 h)	Water	$700 \geq \lambda \geq 400$ nm (20 W white bulbs, 0.05 W cm^{-2});	[286]
	($C_3H_6N_6$, $Cu(NO_3)_2$, and NH_4VO_3)		CH_4: 305 µmol h^{-1} g^{-1}	
Nb-TiO_2/g-C_3N_4	Calcination method (500 °C, 5 h and 500 °C, 2 h)	Water	Simulated sunlight (30 W white bulbs);	[287]
	($C_{12}H_{28}O_4Ti$, ($Nb(OCH_2CH_3)_5$, $CH_3COCH_2COCH_3$, and $C_3H_6N_6$)		HCOOH: 698 µmol h^{-1} g^{-1}	
g-C_3N_4/SnS_2	Thermal treatment and hydrothermal method (550 °C, 2 h and 140 °C, 12 h)	$NaHCO_3$ and H_2SO_4	$\lambda \geq 420$ nm (300 W Xe);	[288]
	($C_3H_6N_6$, $SnCl_4 \cdot 5H_2O$, and $C_3H_7NO_2S$)		CH_3OH: 2.3 µmol h^{-1} g^{-1}	
g-C_3N_4/Bi_2WO_6	Thermal treatment and hydrothermal method (550 °C, 2 h)	Water vapor	$\lambda \geq 420$ nm (300 W Xe);	[289]
	(CH_4N_2O, $Bi(NO_3)_3 \cdot 5H_2O$ and $Na_2WO_4 \cdot 2H_2O$)		CO: 5.19 µmol h^{-1} g^{-1};	
			Stability: decrease	
g-C_3N_4/Sn_2S_3-DETA	Thermal treatment and hydrothermal method (550 °C, 2 h and 180 °C, 12 h)	HCl and $NaHCO_3$	$\lambda \geq 420$ nm (300 W Xe);	[290]
	(CH_4N_2O, $SnCl_4 \cdot 5H_2O$, CH_3CSNH_2, and DETA)		CH_4: 4.84 µmol h^{-1} g^{-1};	
			AQY@420 nm: 2.8%;	
			Stability: decrease	
g-C_3N_4/ZnO	Thermal treatment method (550 °C, 2 h)	HCl and $NaHCO_3$	$\lambda \geq 420$ nm (300 W Xe);	[291]
	(CH_4N_2O, $Zn(NO_3)_2 \cdot 6H_2O$)		CH_3OH: 0.6 µmol h^{-1} g^{-1}	

Table 8. Continued.

| Photocatalyst	Synthetic method [Precursor]	Reaction medium	Illumination [Performance]	Ref.
g-C$_3$N$_4$/FeWO$_4$	Wet chemical method (550 °C, 4 h and 400 °C, 2 h) (C$_3$H$_6$N$_6$, NH$_4$Cl, Na$_2$WO$_4$·2H$_2$O, and (NH$_4$)$_2$Fe(SO$_4$)$_2$·6H$_2$O)	Water	Simulated sunlight (300 W Xe, 100 mW cm^{-2}); CO: 6 µmol h^{-1} g^{-1}; AQY@420 nm: 0.3%; Stability: decrease	[292]
SiC@MoS$_2$	Self-assembling method (1450 °C, 5 h and 200 °C, 24 h) (C$_8$H$_{20}$O$_4$Si, C$_6$H$_{12}$O$_6$, C$_2$H$_5$NS, and Na$_2$MoO$_4$·2H$_2$O)	Water	λ ≥ 420 nm (300 W Xe); CH$_4$: 323 µmol h^{-1} g^{-1}; AQY@420 nm: 1.75%; Stability: >40 h	[293]
RuRu′/Ag/g-C$_3$N$_4$	Thermal treatment and adsorption method (550 °C, 4 h) (CH$_2$N$_2$, AgNO$_3$, and RuRu′)	Water	λ > 400 nm (400 W Hg); HCOOH: 2115 µmol h^{-1} g^{-1}; AQY@400 nm: 5.2%	[294]
RuRu′/Ag/mp g-C$_3$N$_4$	Thermal treatment and adsorption method (550 °C, 4 h) (CH$_2$N$_2$, AgNO$_3$, and RuRu′)	Water	λ > 400 nm (400 W Hg); HCOOH: 68.3 µmol h^{-1} g^{-1}; AQY@400 nm: 0.2%	[295]
g-C$_3$N$_4$/Bi$_4$O$_5$I$_2$	Thermal treatment and hydrolytic method (550 °C, 4 h and 160 °C, 16 h) (C$_3$H$_6$N$_6$, Bi(NO$_3$)$_3$·5H$_2$O, and KI)	H$_2$SO$_4$ and NaHCO$_3$	λ > 400 nm (300 W Xe); CO: 45.6 µmol h^{-1} g^{-1}; Stability: decrease	[296]
Au@Void@ g-C$_3$N$_4$/SnS	Hydrothermal method (550 °C, 2 h and 200 °C, 10 h) (HAuCl$_4$·3H$_2$O, SnCl$_2$·2H$_2$O Na$_3$C$_6$H$_5$O$_7$·2H$_2$O, and Na$_2$S)	Water	λ ≥ 420 nm (300 W Xe); CO: 5.7 µmol h^{-1} g^{-1}; Stability: decrease	[297]
g-C$_3$N$_4$/BiOBr/Au	Thermal treatment and photodeposition method (550 °C, 3 h and 300 W Xe, 2 h) (CH$_4$N$_2$S, Bi(NO$_3$)$_3$·5H$_2$O, CTAB and AuCl$_3$)	H$_2$SO$_4$ and NaHCO$_3$	Simulated sunlight (300 W Xe); CO: 6.67 µmol h^{-1} g^{-1}	[298]
g-C$_3$N$_4$/α-Fe$_2$O$_3$	Wet-chemical method (550 °C, 4 h and 400 °C, 1 h) (Fe(NO$_3$)$_3$·9H$_2$O, AlCl$_3$ and CH$_4$N$_2$O)	Water	λ ≥ 420 nm (300 W Xe); CO: 24 µmol h^{-1} g^{-1}	[299]
g-C$_3$N$_4$/Ag/AgCl/ BiVO$_4$	Hydrothermal method (550 °C, 4 h and 180 °C, 12 h) (C$_3$H$_6$N$_6$, BiCl$_3$, NH$_4$VO$_3$, and AgNO$_3$)	NaOH	750 ≥ λ ≥ 380 nm (8 W fluorescent); CH$_4$: 205 µmol h^{-1} g^{-1}	[300]
Bi$_2$WO$_6$/RGO/g-C$_3$N$_4$	Thermal treatment and hydrothermal method (550 °C, 2 h and 160 °C, 6 h) (C$_3$H$_6$N$_6$, Bi(NO$_3$)$_3$·5H$_2$O, Na$_2$WO$_4$·2H$_2$O, and graphite)	Water	λ ≥ 420 nm (300 W Xe); CO: 15.96 µmol h^{-1} g^{-1}; Stability: decrease	[301]
ZnV$_2$O$_6$/RGO/ g-C$_3$N$_4$	Solvothermal method (550 °C, 2 h and 200 °C, 24 h) (NH$_4$VO$_3$, Zn(O$_2$CCH$_3$)$_2$, graphite, and C$_3$H$_6$N$_6$)	NaOH	λ ≥ 420 nm (35 W Xe, 20 mW cm^{-2}); CH$_3$OH: 1862 µmol h^{-1} g^{-1}; AQY@450 nm: 0.2830%; Stability: decrease	[302]
CoZnAl-LDH/RGO/g-C$_3$N$_4$	Hydrothermal method (550 °C, 4 h and 180 °C, 6 h) (C$_3$H$_6$N$_6$, Co(NO$_3$)$_2$·6H$_2$O, Zn(NO$_3$)$_2$·6H$_2$O, graphite, and Al(NO$_3$)$_3$·9H$_2$O)	Water	Simulated sunlight (300 W Xe); CO: 3.9 µmol h^{-1} g^{-1}; AQY@385 nm: 0.45%; Stability: decrease	[303]
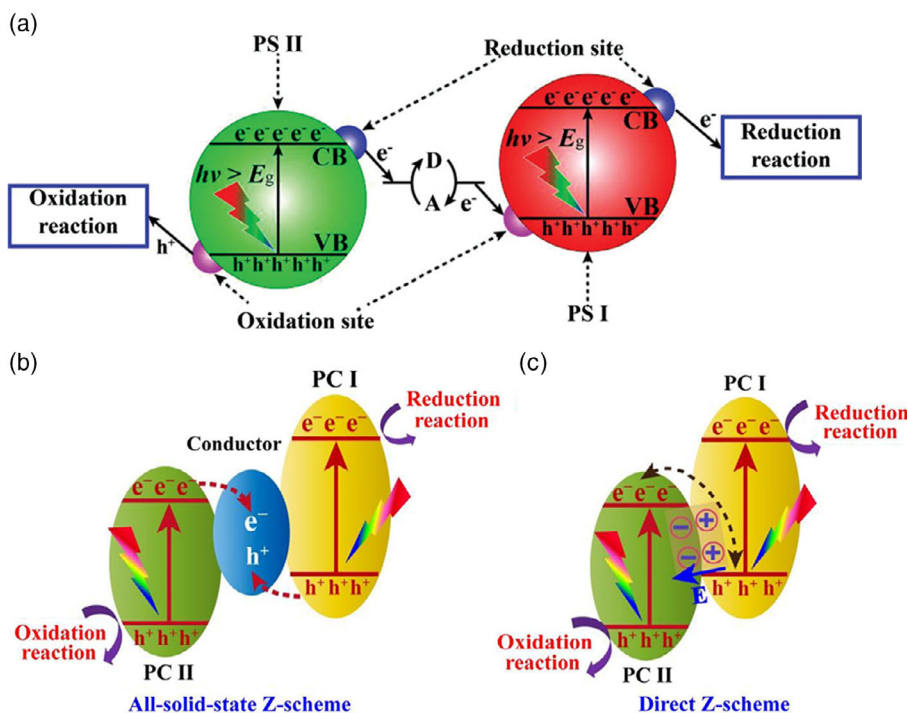
Figure 17. a) Scheme of the Z-scheme photocatalytic mechanism. Reproduced with permission.[304] Copyright 2014, WILEY-VCH. Schematic illustration of charge carrier transfer in b) all-solid-state and c) direct Z-scheme photocatalysts. Reproduced with permission.[305] Copyright 2018, Elsevier.

(Figure 22d). It was thus inferred that the reduction process likely occurred through a multi-electron pathway with adsorbed formate as reaction intermediates. HCOOH, HCHO, CH_3OH, and CH_4 were formed requiring 2, 4, 6, and 8 electrons, respectively.

As opposed to the formate multi-electron path proposed for the formation of hydrocarbons from CO_2 reduction, HCOOH was supposed to be a critical intermediate for CO generation during the photocatalytic CO_2 reduction. This conclusion has been corroborated by in situ DRIFTS measurements which showed the increase in surface HCOOH with bands at 1705 and 1726 cm^{-1} for CO_2 reduction over Ni/NiO/g-C_3N_4 upon light illumination (**Figure 23**).[219]

5.2.2. In Situ Diffuse Reflectance UV-Visible Spectroscopy

In situ diffuse reflectance (DR) UV-visible spectroscopy was conducted to gain mechanistic insight into photocatalytic CO_2 reduction on Re-COF (Re complex Re(bpy)(CO)$_3$Cl).[164] A prominent absorption in the 550–800 nm range akin to the wide absorption of the ICT band in transient absorption (TA) was seen (**Figure 24**a), indicating the emergence of an excited ICT state. The strength of the ICT peak increased in the initial 15 min, while the absorption at 400–500 nm decreased with an isosbestic point at 539 nm (Step I, Figure 24a). During the induction period, the absorption at 550–800 nm was found to decrease markedly after 3 h, whereas the feature at <430 nm grew and a new isosbestic point was identified at 430 nm (Step II, Figure 24b), suggesting the generation of a new intermediate. Following Step II, the spectra remained almost constant (Step III, Figure 24b), matching the time window for steady

CO production, an indication that the reaction system reached an equilibrium.

The complex FeTCPP was observed to exhibit three typical absorption peaks at 410 (Soret band), 568 and 610 nm (Q band), corresponding to the Fe^{III} porphyrin state.[241] The band signal at 410 nm declined for the g-C_3N_4/FeTCPP upon visible light illumination in Ar (Figure 24c). A new peak evolved at 428 nm with intensity increasing after illumination, attributable to Fe^{II} TCPP (Soret band) stemming from the change of Fe^{III} to Fe^{II}. After irradiation for 5 min, two peaks appeared at 533 and 649 nm, corresponding to Fe^{II} TCPP and Fe^{I} TCPP (Q band), attributed to the transformation of Fe^{III} to Fe^{II} and Fe^{I}. Under CO_2 atmosphere, the peak at 410 nm was observed to blue-shift with intensity increasing slightly (Figure 24d), implying the yield of a Fe^{II} TCPP···CO_2 complex. A new peak emerged at 428 nm with intensity increasing rather slowly at the start, whereas the peak signal at 410 nm started to drop after 15 min of irradiation. The absorption at 428 nm increased more rapid, whereas the increase rate was significantly slower than that in Ar. Similar to those in Ar, two additional peaks evolved at 528 and 649 nm, and the Q bands at 568 and 610 nm blue-shifted to 564 and 605 nm, respectively. These results suggested the conversion of Fe^{III} to Fe^{II} and Fe^{I}.

5.2.3. In situ Electron Paramagnetic Resonance

The first ET process to form Fe^{I} TCPP intermediate was proposed for CO_2 photoreduction over g-C_3N_4/FeTCPP based on electron paramagnetic resonance (EPR) analysis.[239] Broad resonance with g values at 5.8465 and 4.9988 (**Figure 25**a)
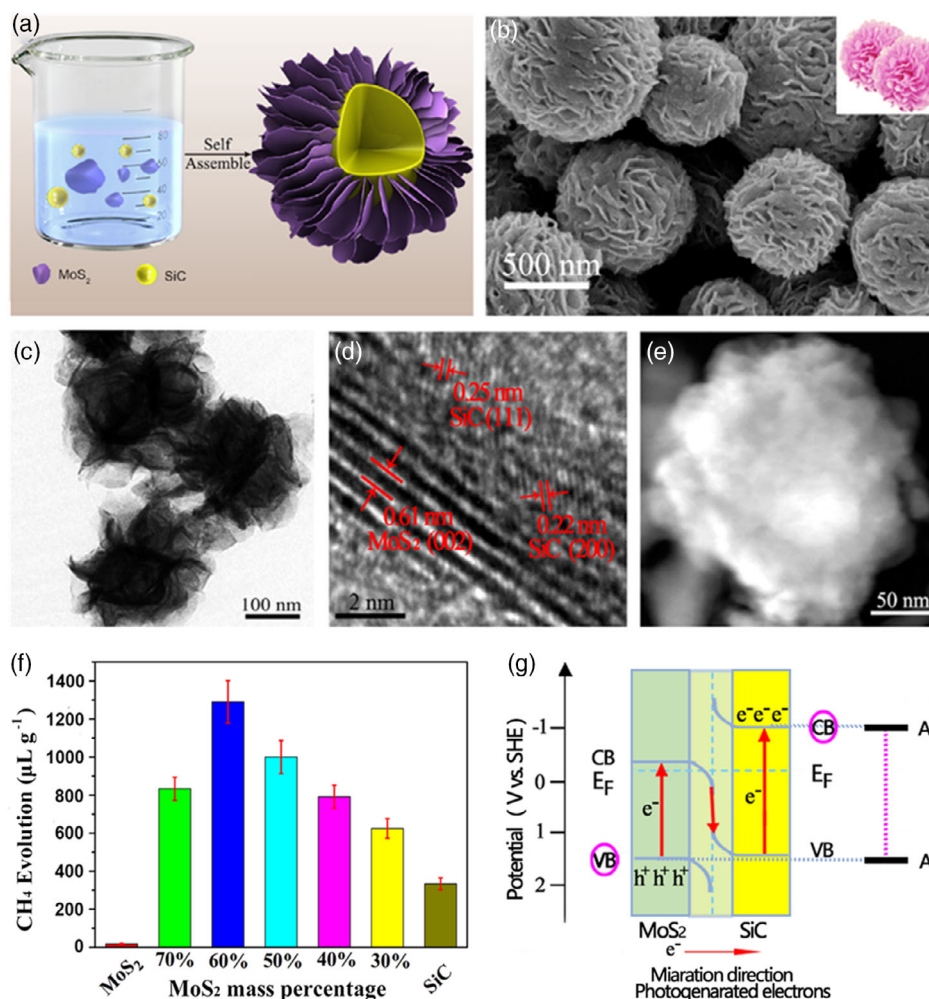
Figure 18. a) Schematically synthetic process of SiC@MoS$_2$ nanoflower. b) SEM, c) TEM, d) high-resolution transmission electron microscopy (HRTEM), and e) scanning transmission electron microscopy (STEM) images. f) CH$_4$ evolution on SiC@MoS$_2$ with different MoS$_2$ contents for 4 h reaction. g) Z-scheme model of SiC@MoS$_2$ photocatalyst and its charge transfer process under light irradiation. Reproduced with permission.[293] Copyright 2018, American Chemical Society.
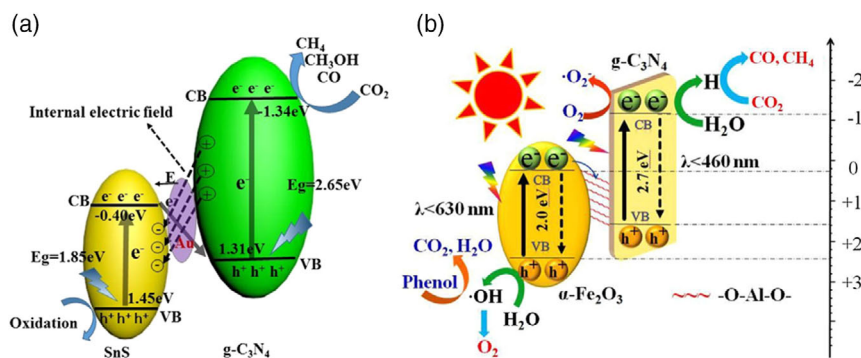

Figure 19. a) Schematic illustration of band structure diagram and photoinduced carrier transfer of yolk-shell Au@g-C$_3$N$_4$/SnS under visible light irradiation. Reproduced with permission.[297] Copyright 2018, American Chemical Society. b) Schematic on the charge transfer and separation in the fabricated Al–O-bridged g-C$_3$N$_4$/α-Fe$_2$O$_3$ and the induced photochemical reactions. Reproduced with permission.[299] Copyright 2017, Elsevier.

and a pronounced peak at about 2.0035 (Figure 25b) were identified typical of the high spin Fe^{III} tetraphenylporphyrin.

The photoinduced electrons in 2D g-C$_3$N$_4$ were transferred to Fe^{III} TCPP upon irradiation, generating Fe^{II}, Fe^{I}, and Fe^0
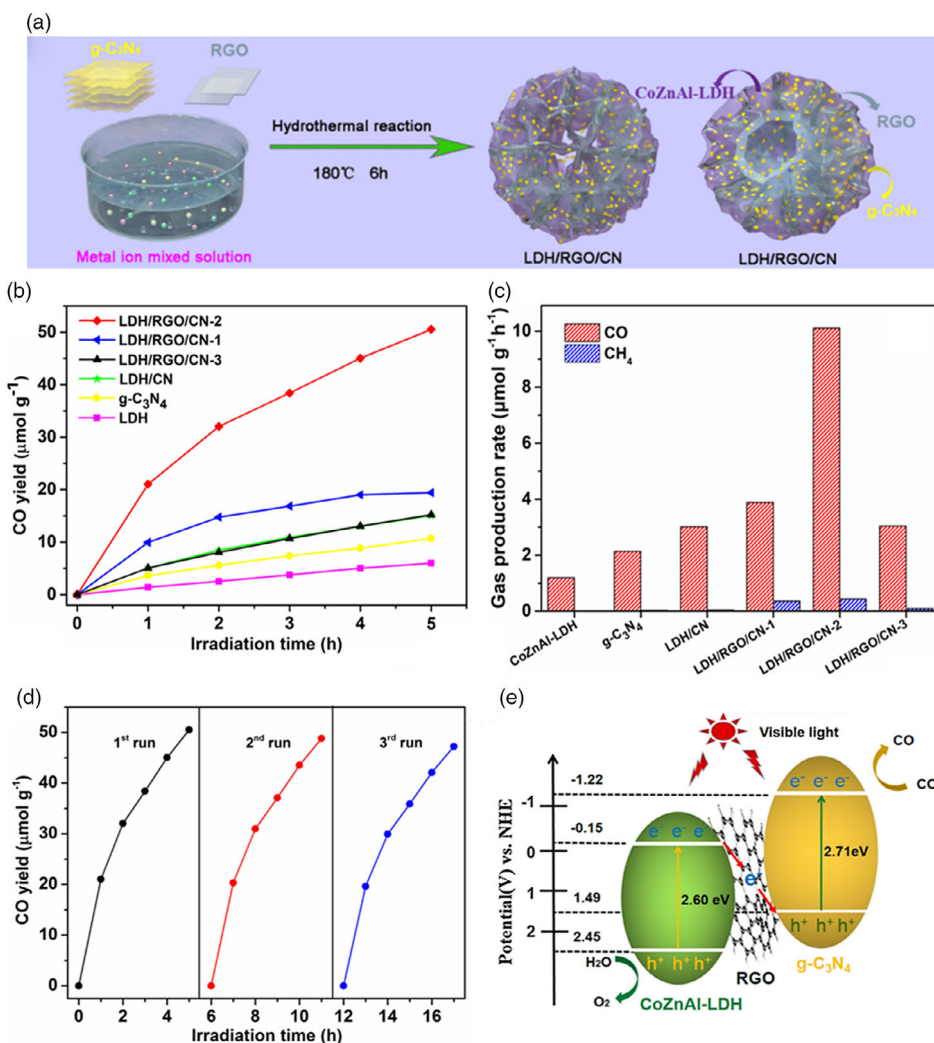
Figure 20. a) Illustration for the synthesis of urchin-like CoZnAl-LDH/RGO/g-C$_3$N$_4$. b,c) Time evolutions of CO and average gas production rates over different catalysts; d) Recycling test of photocatalytic CO production over LDH/RGO/CN-2. e) Schematic diagram of the possible photocatalytic mechanism for LDH/RGO/CN. Reproduced with permission.[303] Copyright 2019, Elsevier.

TCPP intermediates. Fe^{II} and Fe^0 TCPP exhibited marginal EPR signal, whereas the Fe^I TCPP showed a sharp peak at $g = 2.0033$. The Fe^I TCPP intermediate was remarkably more apparent under CO$_2$ atmosphere. A distinct EPR peak at $g = 2.009$ originating from CO$_2$ adsorption was also observed (Figure 25b).

5.2.4. In Situ Raman Spectroscopy

In situ Raman spectroscopy allows one to monitor CO$_2$ structure variation with vibration spectrum, detect intermediates, and identify possible major catalytic active sites, being beneficial to reaction mechanism exploration.[311,312] This technique has been used for electrochemical CO$_2$ reduction to offer fingerprint-type information about reduction intermediates and catalyst surface state.[313] Typical Raman peaks for adsorbed *CO and C≡O on catalyst surface were detected to be located at 282 and 2057 – 2092 cm^{-1}, respectively.[314] The vibration of C—H in

the region from 2700 to 3000 cm^{-1} was also observed, which originates from possible intermediates such as *CHO and *C$_2$H$_2$O for the formation of hydrocarbons. However, a more precise assignment of these peaks is rather challenging due to the complexity of reaction intermediates that contain C—H bonds. Note that in situ Raman spectroscopy has been seldom used for exploration of CO$_2$ photocatalysis to date, which deserves future research in this regard.

5.3. DFT Calculations

DFT calculations can help understand the band structure of a photocatalyst and possible reaction paths of CO$_2$ reduction. Mechanistic understanding of the CO$_2$ reduction process over Ni-TpBpy (2,2′-bipyridine-based COF-coordinated single Ni sites) was examined by DFT calculations. The adsorption of CO$_2$ onto the catalyst appears to be the rate-limiting step during
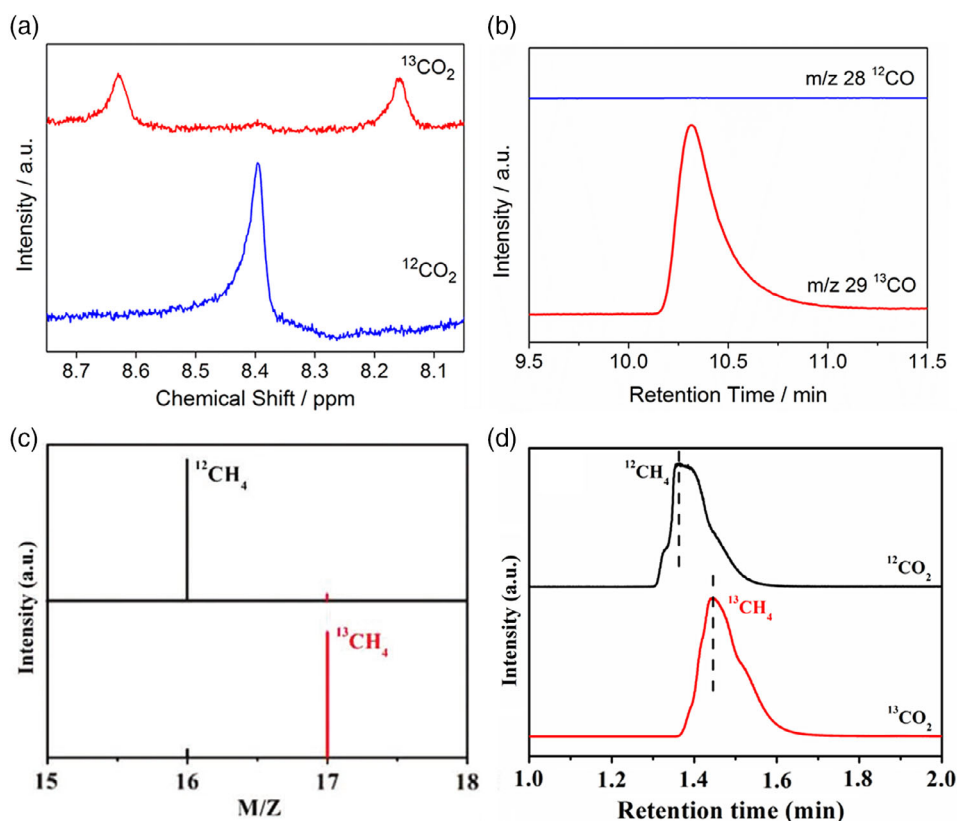
1900546 (31 of 41)

Figure 21. a) No deuterium NMR spectra of a reacted solution containing 8 mg of RuP ($1.5\,\mu mol\,g^{-1}$)/NS-C_3N_4-NPU90. b) GC-MS results of the gas-phase products after the $^{13}CO_2$ isotope tracer experiments. Reproduced with permission.[235] Copyright 2018, American Chemical Society. GC-MS analyses of CH_4 c) labeled by ^{13}C and ^{12}C from photocatalytic CO_2 reduction over CCN and d) from CO_2 reduction over CCN after irradiation for several hours with different carbon sources. Reproduced with permission.[194] Copyright 2019, WILEY-VCH.

the reduction process. As shown in **Figure 26**a, it unlikely ocurrs to add H^+ into $[L_2Ni]^0$ to form L_2Ni-H^+ as this reaction is end-ergonic by $141.4\,kcal\,mol^{-1}$ compared with the $[L_2Ni]^0$.[214] An L_2Ni-CO_2 adduct was formed at $\Delta G = 3.2\,kcal\,mol^{-1}$, indicating the more favorable binding of $[L_2Ni]^0$ with CO_2. Introducing model compound of the keto unit in TpBpy apparently lowered the ΔG of the key intermediate to favor the generation of the Ni–CO_2 adduct, hence improving the CO selectivity. The ΔG of CO_2 on Ni-TpBpy was found to be larger than that of Co-TpBpy, whereas the ΔG of H_2O on Ni-TpBpy was smaller than that of Ni-TpBpy (Figure 26b). This indicated that Ni-TpBpy had higher activity and selectivity than Co-TpBpy (2,2′-bipyridine-based COF-coordinated single Co sites) which only increased reduction activity due to the competing H_2 evolution reaction, matching with the experimental observation. Further calculations on the reduction path through a carboxyl intermediate were performed over an optimized building unit. It was calculated to be thermodynamically possible for the protonation of Ni–CO_2 adduct to form a Ni–COOH adduct (Figure 26c). Subseqent conversion of Ni–COOH to Ni–CO with H^+ proceeded readily and demanded low barrier to desorb CO from Ni–CO. The ΔG required for COF–Ni adducts was substantially lower than that for L_2Ni adducts. This suggests that it is kinetically more likely to produce CO over Ni-TpBpy. By combining experiments and DFT results, a possible reaction mechanism for the

photocatalytic CO_2 reduction by Ni-TpBpy was put forth (Figure 26d). Specifcaly, $Ru(bpy)_3^{2+}$ was subjected to excitation under visible light illumination, which then transferred electrons to the adsorbed CO_2 molecules enabing their reduction over Ni-TpBpy. The binding of CO_2 on Ni sites over H^+ was essential to suppress H_2 evolution. The CO_2 bound to COF-Ni exhibited a bending structure, suggesting activation of CO_2 over single Ni sites. After elongation of bond length, one of the C–O bonds in Ni–COOH transformed to a C–O single bond, but the other C–O bond retained a double bond. The strikingly lowered ΔG of the COF–Ni–CO_2H intermediate was most probably due to hydrogen bonding formed between COOH and the keto moiety, hence increasing stabilization of the key intermediate and improving the CO_2 conversion. The calculations suggested that the single Ni sites in TpBpy were the major active centers to coordinate CO_2 molecules followed by their activation and reduction. The TpBpy played a role in hosting CO_2 molecules and the single metal sites, and also made contributions to the catalytic performance for CO_2 reduction to CO, in accordance with experimental results.

The photocatalytic CO_2 reduction on a range of porphyrin-tetrathiafulvalene COFs was also calculated.[161] As shown in **Figure 27**a, the photoinduced electron transfer (PET) process takes place from the tetrathiafulvalene (TTF) species (HOMO center) to the metalloporphyrin (TAPP) species (LUMO center)
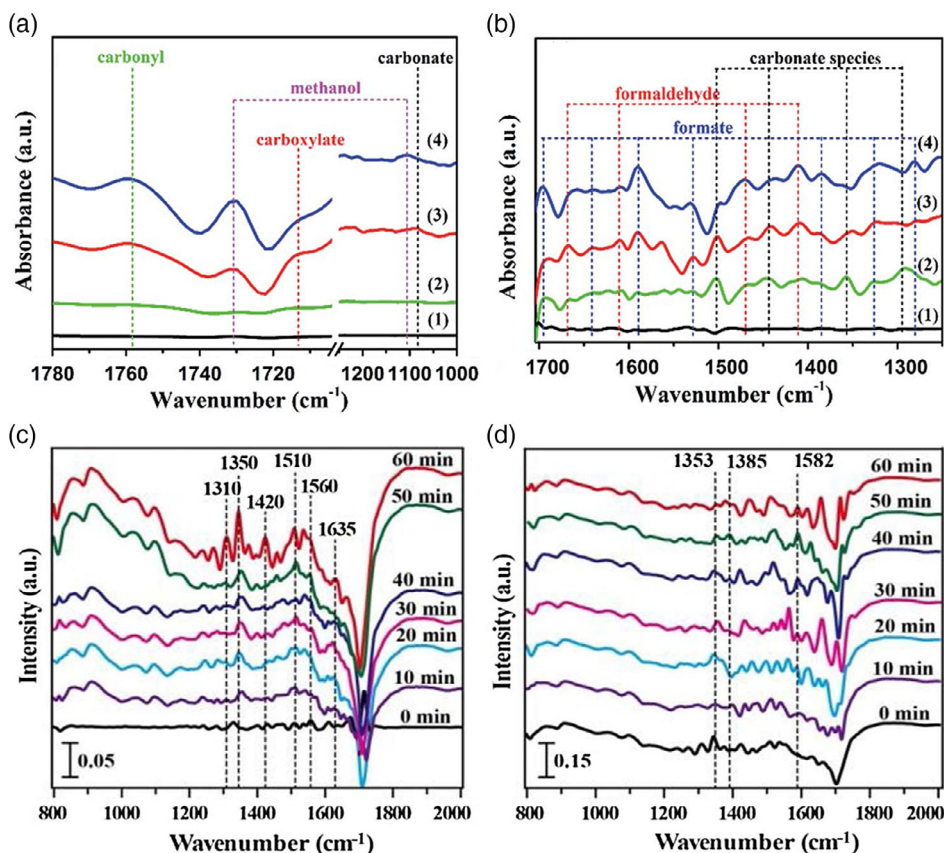
Figure 22. a,b) The in-situ FTIR spectra of NS-CN in different wavenumber ranges: (1) without CO_2 gas and irradiation, (2) with flowing CO_2 gas for 30 min without irradiation, and (3) irradiation for 30 min and (4) 60 min. Reproduced with permission.[185] Copyright 2017, Royal Society of Chemistry. c) In-situ FTIR spectra of CO_2 adsorption in the dark and d) CO_2 reduction under 420 nm light irradiation on the CAG composites. Reproduced with permission.[285] Copyright 2018, Elsevier.
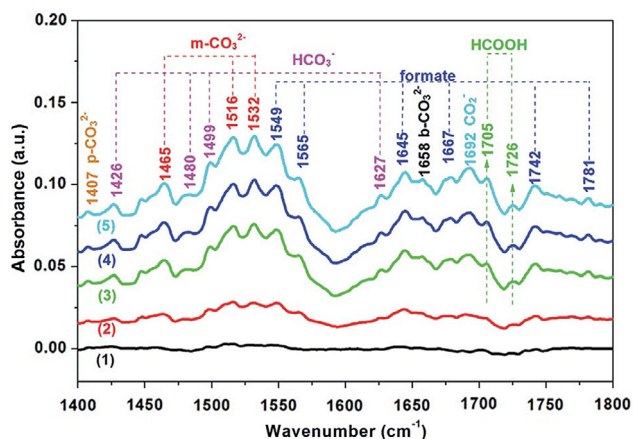

Figure 23. In-situ FT-IR spectra of the reaction of CO_2 and H_2O on 3 wt% Ni/NiO/g-C_3N_4: (1) without CO_2 gas and irradiation, (2) with flowing CO_2 gas for 30 min without irradiation, and with irradiation for (3) 20 min, (4) 40 min, and (5) 60 min. Reproduced with permission.[219] Copyright 2019, Royal Society of Chemistry.

after absorbing photons. In the following, the excited electrons migrate to active centers (Zn/Cu in TAPP) to initiate CO_2 reduction. At the same time, the photoinduced holes in TTF can oxidize H_2O to O_2, giving rise to electrons to keep charge balance. To check if this would be the case, DFT calculations were performed. The low-lying electronic transitions in the COF structure were shown in Figure 27b with an inset demonstrating the initial excitation contribution (from HOMO to LUMO). The TTF part that donated electrons dominated HOMO, whereas TAPP part predominantly contributed to LUMO. This indicates that the PET process took place upon light illumination to generate electrons on the TAPP-M (TAPP-M$^-$) and holes at the TTF unit (TTF$^+$). In the cases of the hole-doped TTF$^+$, the spin density mainly located on C=C linker and the S atoms, suggesting that the oxidation of H_2O could be carried out on the aforementioned sites. In the case of electron-enriched TAPP-M$^-$, CO_2 reduction tended to ocurr on metal ion centers.

The energy necessary for CO_2 adsorption and CO desorption could be determined by DFT calculations. TCN(NH_3) was calculated to have a larger energy for CO_2 adsorption (-0.358 eV) and thus stronger CO_2 adsorption performance than unmodified TCN (**Figure 28**a).[89] The NeH···O separation in TCN(NH_3) was found to be 2.445 Å, falling in the range of hydrogen bonding interactions, which led to enhancement of CO_2 adsorption energy. Nevertheless, the energy required for CO desorption (0.032 eV) in TCN(NH_3) was calculated to be lower than that of TCN (0.148 eV) (Figure 28b) based on a C-terminated CO
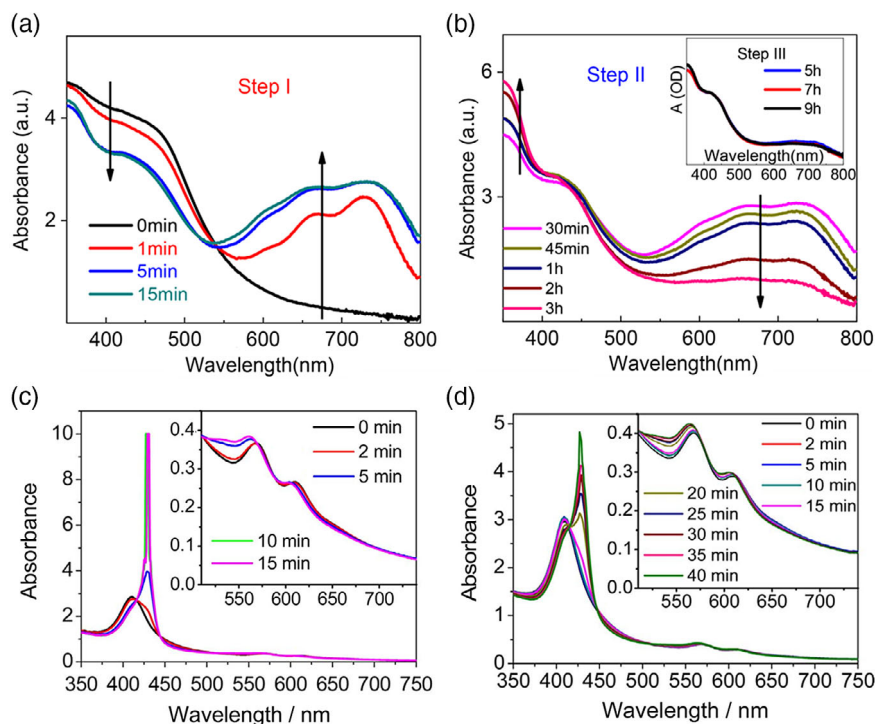
Figure 24. In situ diffuse reflectance UV–vis spectra of Re-COF under photocatalytic conditions within a) 15 min and b) 3 h.[164] Copyright 2018, American Chemical Society. Quasi in situ UV–vis absorption spectra of g-C_3N_4/FeTCPP under visible light irradiation purged with c) Ar and d) CO_2. Reproduced with permission.[239] Copyright 2018, Elsevier.
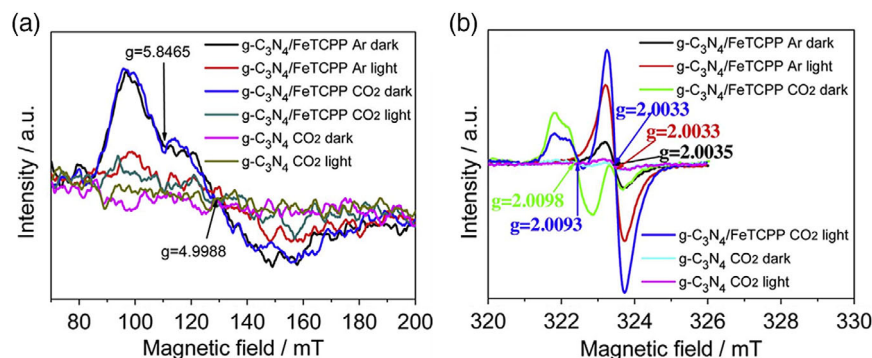

Figure 25. Quasi in situ EPR spectra of g-C_3N_4/FeTCPP and pure g-C_3N_4 nanosheets in Ar and CO_2 atmosphere under dark and visible-light irradiation (420 nm $< \lambda <$ 780 nm), respectively: a) low-field and b) high-field part. Reproduced with permission.[239] Copyright 2018, Elsevier.

adsorption model. This was supposed to be due to the weaker NeH···C interaction than the NeH···O interaction. Therefore, DFT calculations disclosed that the introduction of amino groups effectively enhanced CO_2 adsorption and also facilitated CO desorption, benefiting photocatalytic CO_2 reduction.

6. Conclusions and Future Perspectives

Photocatalytic CO_2 reduction appears to be a promising and clean approach in mitigating and converting CO_2 into value-added chemicals and fuels. The last decades have witnessed significant progresses in photocatalytic CO_2 reduction, including

construction of efficient photocatalysts, development of advanced characterization techniques, and study of underlying mechanism. However, there are still major issues that need to be faced and addressed, including: 1) the research achievements cannot satisfy large-scale industrial implementations; 2) the mechanism behind this reaction remains elusive, and some important intermediates cannot be exactly captured or identified; 3) the efficiency and selectivity for target products are still insufficient for industrial implementation in the future.

Metal-free materials show promise for the photocatalytic CO_2 reduction as they are earth-abundant, cost-effective, and environmental-friendly, suitable for industry or commercialization. Nevertheless, from the material synthesis point of view,
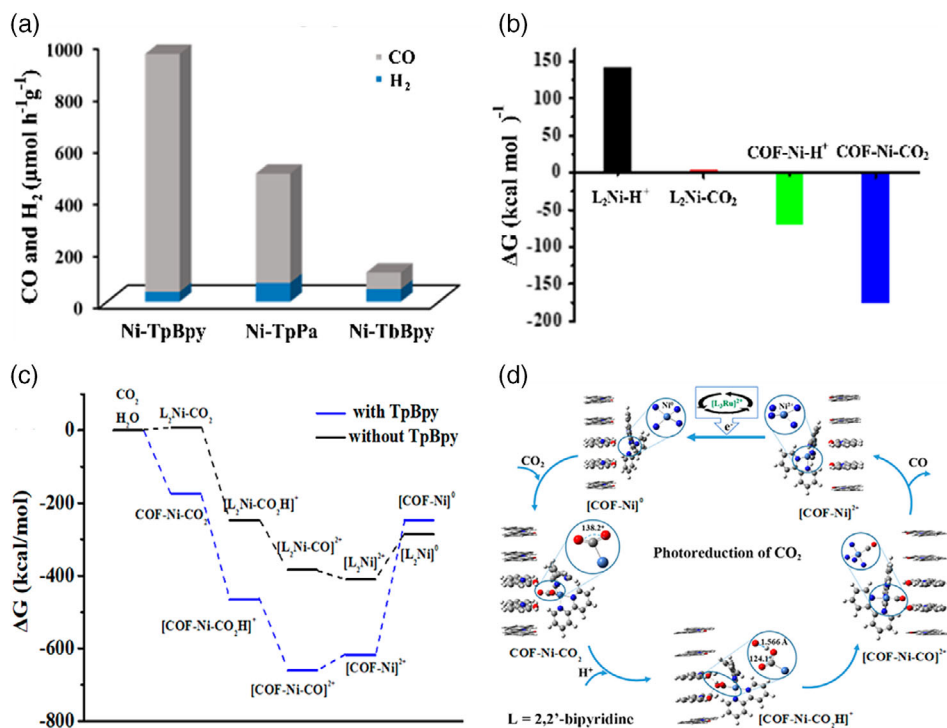
Figure 26. DFT-calculated relative Gibbs free energy (ΔG) with zero-point correction of CO_2 and H^+ a) with and without the optimized building block of TpBpy. L is 2,2′-bipyridine and b) with the optimized building block of Ni-TpBpy and Co-TpBpy. c) DFT-calculated ΔG profiles with zero-point correction (ZPE) included for the conversion of CO_2 into CO with and without the optimized building block of TpBpy. d) Proposed reaction mechanism for the photoconversion of CO_2 into CO on Ni-TpBpy. Reproduced with permission.[214] Copyright 2019, American Chemical Society.
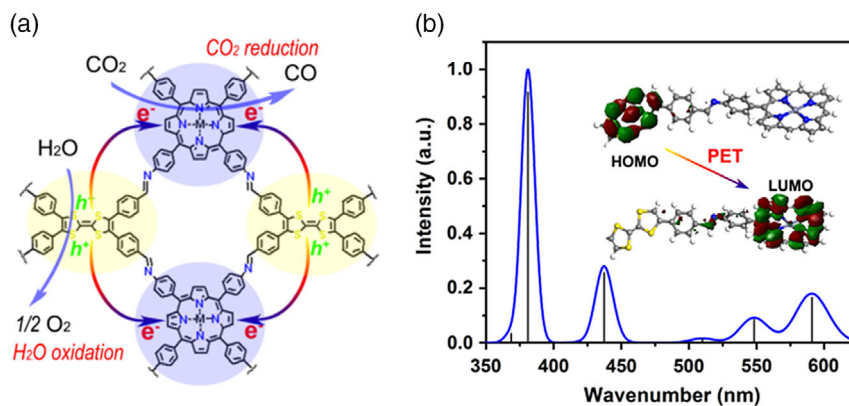
Figure 27. a) Schematic of the mechanism of TTCOF-M CO_2 RR with H_2O oxidation. b) Theoretical simulation UV–vis DRS of TTCOF-Zn with an inset showing scheme PET route under light excitation. Reproduced with permission.[161] Copyright 2019, WILEY-VCH.

it remains a challenge to realize mass production of metal-free photocatalysts. Further, in addition to throughput, yield, manufacturing volume and cost, control of the composition, morphology, and defect density is highly desirable.

The design and development of hierarchic structures with multiple active sites can be the focus of future research to facilitate CO_2 photocatalysis. Construction of 3D hollow structures with micro-mesoporosity can afford abundant surface active sites. Tuning of band structure by surface modification or Z-scheme enables one to enhance efficiency of light harvesting and

charge carrier separation while preserving strong redox ability. Combination of the two strategies is preferred.

At present, most CO_2 photoconversion studies have paid attention to the reduction half-reaction, whereas the oxidation half-reaction, such as H_2O oxidation, have rarely been considered. It is thus of significance to develop new and effective ways to accelerate this oxidation half-reaction and enhance photocatalytic CO_2 reduction. Equally important, the back reactions of photocatalytic CO_2 reduction remain to be further explored.
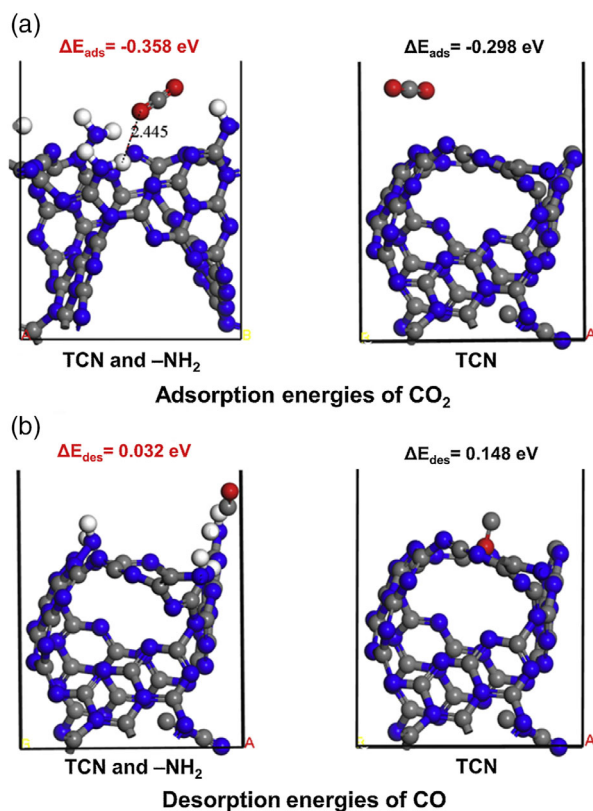
Figure 28. a) Adsorption energies of CO_2 and b) desorption energies of CO on various TCN catalysts. Reproduced with permission.[89] Copyright 2019, Elsevier.

ex-situ and in-situ techniques is needed. This can in turn favor optimization of catalyst configurations and other uncovered properties to develop superior CO_2 photocatalytic systems.

Acknowledgements

Conflict of Interest

The authors declare no conflict of interest.

Keywords

To suppress the parasitic HER and enhance photocatalytic CO_2 reduction, construction of a three-phase catalyst by surface-wettability modification appears useful.[315] Such a strategy allows sufficient contact of gaseous CO_2, water, and solid catalyst, imparting higher CO_2 and lower proton surface concentrations. This can overcome the sluggish mass transfer of CO_2 and simultaneously inhibit the competitive proton reduction.

The photo-recyclability of metal-free-based materials is a critical parameter for wide range of practical applications. Most of the stability tests reported in the literature were conducted for only a few hours, far below the timescale required in industry. In addition, the cause of catalyst deactivation needs further elucidation.

Even though substantial advances have been achieved in converting CO_2 into C_1 chemicals such as CH_4 and CO using metal-free materials, the production of multi-carbon hydrocarbons with larger energy densities and higher economic values per unit mass remains less explored. Further research in this direction would be more attractive. To this end, the design of photocatalysts with different active sites to afford synergistic cascade catalysis would be key.

Despite recent progress in understanding reaction intermediates and pathways for CO_2 reduction, the exact reaction mechanism, durability, and catalytic active centers for different metal-free photocatalysts need to be further elucidated. To this end, the development of more accurate DFT models and advanced

[1] EIA-International Energy Outlook, https://www.eia.gov/outlooks/ieo/ (accessed: November 15).

[2] L. Gustavsson, S. Haus, M. Lundblad, A. Lundström, C. A. Ortiz, R. Sathre, N. L. Truong, P. E. Wikberg, *Renewable Sustainable Energy Rev.* **2017**, *67*, 612.

[3] a) P. Tans, NOAA/ESRL. www.esrl.noaa.gov/gmd/ccgg/trends/; b) R. Keeling, Scripps Institution of Oceanography. scrippsco2.ucsd.edu/, **2019**.

[4] R. W. Miller, D. Rice, Carbon dioxide levels hit landmark at 415 ppm, highest in human history, https://www.usatoday.com/story/news/world/2019/05/13/climate-change-co-2-levels-hit-415-parts-per-million-human-first/1186417001/ (accessed: May 2019).

[5] K. Li, X. Q. An, K. H. Park, M. Khraisheh, J. W. Tang, *Catal. Today* **2014**, *224*, 3.

[6] P. M. Vitousek, H. A. Mooney, J. Lubchenco, J. M. Melillo, *Science* **1997**, *277*, 494.

[7] W. H. Wang, Y. Himeda, J. T. Muckerman, G. F. Manbeck, E. Fujita, *Chem. Rev.* **2015**, *115*, 12936.

[8] G. Yisilamu, H. Maimaiti, A. Awati, D. D. Zhang, F. C. Sun, B. Xu, *Energy Technol.* **2018**, *6*, 1168.

[9] M. Meinshausen, N. Meinshausen, W. Hare, S. C. B. Raper, K. Frieler, R. Knutti, D. J. Frame, M. R. Allen, *Nature* **2009**, *458*, 1158.

[10] M. Vermeer, S. Rahmstorf, *Proc. Natl. Acad. Sci. U. S. A.* **2009**, *106*, 21527.

[11] A. Kudo, Y. Miseki, *Chem. Soc. Rev.* **2009**, *38*, 253.

[12] M. W. Jia, C. Choi, T.-S. Wu, C. Ma, P. Kang, H. C. Tao, Q. Fan, S. Hong, S. Z. Liu, Y.-L. Soo, Y. Jung, J. S. Qiu, Z. Y. Sun, *Chem. Sci.* **2018**, *9*, 8775.

[13] Y. N. Gao, S. Z. Liu, Z. Q. Zhao, H. C. Tao, Z. Y. Sun, *Acta Phys. -Chim. Sin.* **2018**, *34*, 858.

[14] C. D. Windle, R. N. Perutz, Coord., *Chem. Rev.* **2012**, *256*, 2562.

[15] Y. Q. Qu, X. F. Duan, *J. Mater. Chem.* **2012**, *22*, 16171.

[16] T. F. Hurst, T. T. Cockerill, N. H. Florin, *Energy Environ. Sci.* **2012**, *5*, 7132.

[17] S. Y. Lee, J. U. Lee, I. B. Lee, J. Han, *Appl. Energy* **2017**, *189*, 725.

[18] B. J. Xu, Y. Bhawe, M. E. Davis, *Chem. Mater.* **2013**, *25*, 1564.

[19] C. Y. Xu, Y. W. Zhang, F. Q. Pan, W. H. Huang, B. W. Deng, J. Z. Liu, Z. H. Wang, M. J. Ni, K. F. Cen, *Nano Energy* **2017**, *41*, 308.

[20] F. Y. Gong, H. W. Zhu, Y. P. Zhang, Y. Li, *J. CO₂ Util.* **2018**, *28*, 221.

[21] J. C. Cardoso, S. Stulp, J. F. de Brito, J. B. S. Flor, R. C. G. Frem, M. V. B. Zanoni, *Appl. Catal., B* **2018**, *225*, 563.

[22] J. Cheng, M. Zhang, G. Wu, X. Wang, J. H. Zhou, K. F. Cen, *Environ. Sci. Technol.* **2014**, *48*, 7076.

[23] W. Wang, L. Shang, G. J. Chang, C. Y. Yan, R. Shi, Y. X. Zhao, G. I. N. Waterhouse, D. J. Yang, T. R. Zhang, *Adv. Mater.* **2019**, *31*, 1808276.

[24] Z. Y. Sun, T. Ma, H. C. Tao, Q. Fan, B. X. Han, *Chem* **2017**, *3*, 560.

[25] Q. Fan, P. F. Hou, C. Choi, T.-S. Wu, S. Hong, F. Li, Y.-L. Soo, P. Kang, Y. Jung, Z. Y. Sun, *Adv. Energy Mater.* **2019**, 1903068. https://doi.org/10.1002/aenm.201903068.

[26] H. L. Wu, X. B. Li, C. H. Tung, L. Z. Wu, *Adv. Mater.* **2019**, *31*, 1900709.

[27] K. Sekizawa, S. Sato, T. Arai, T. Morikawa, *ACS Catal.* **2018**, *8*, 1405.

[28] S. C. Lian, M. S. Kodaimati, E. A. Weiss, *ACS Nano* **2018**, *12*, 568.

[29] C. L. Wang, Z. X. Sun, Y. Zheng, Y. H. Hu, *J. Mater. Chem. A* **2019**, *7*, 865.

[30] M. Dilla, N. G. Moustakas, A. E. Becerikli, T. Peppel, A. Springer, R. Schlogl, J. Strunk, S. Ristig, *Phys. Chem. Chem. Phys.* **2019**, *21*, 13144.

[31] F. E. Osterloh, *ACS Energy Lett.* **2017**, *2*, 445.

[32] S. S. Zhu, D. W. Wang, *Adv. Energy Mater.* **2017**, *7*, 1700841.

[33] W. G. Tu, Y. Zhou, Z. G. Zou, *Adv. Mater.* **2014**, *26*, 4607.

[34] K. Li, B. S. Peng, T. Y. Peng, *ACS Catal.* **2016**, *6*, 7485.

[35] T. Inoue, A. Fujishima, S. Konishi, K. Honda, *Nature* **1979**, *277*, 637.

[36] D. I. Won, J. S. Lee, J. M. Ji, W. J. Jung, H. J. Son, C. Pac, S. O. Kang, *J. Am. Chem. Soc.* **2015**, *137*, 13679.

[37] S. J. Woo, S. Choi, S. Y. Kim, P. S. Kim, J. H. Jo, C. H. Kim, H. J. Son, C. Pac, S. O. Kang, *ACS Catal.* **2019**, *9*, 2580.

[38] J. F. Liu, B. Liu, Y. Ren, Y. K. Yuan, H. Zhao, H. Q. Yang, S. Z. Liu, *J. Mater. Chem. A* **2019**, *7*, 14761.

[39] N. G. Moustakas, J. Strunk, *Chem. Eur. J.* **2018**, *24*, 12739.

[40] M. F. Ehsan, M. N. Ashiq, T. He, *RSC Adv.* **2015**, *5*, 6186.

[41] H. Pang, X. G. Meng, H. Song, W. Zhou, G. L. Yang, H. W. Zhang, Y. Izumi, T. Takei, W. Jewasuwan, N. Fukata, J. H. Ye, *Appl. Catal., B* **2019**, *244*, 1013.

[42] Q. Q. Bi, J. W. Wang, J. X. Lv, J. Wang, W. Zhang, T. B. Lu, *ACS Catal.* **2018**, *8*, 11815.

[43] Y. H. Qi, Q. Xu, Y. Wang, B. Yan, Y. M. Ren, Z. M. Chen, *ACS Nano* **2016**, *10*, 2903.

[44] L. J. Cheng, L. Q. Liu, D. F. Wang, F. Yang, J. H. Ye, *J. CO₂ Util.* **2019**, *29*, 196.

[45] J. Di, X. X. Zhao, C. Lian, M. X. Ji, J. X. Xia, J. Xiong, W. Zhou, X. Z. Cao, Y. B. She, H. L. Liu, K. P. Loh, S. J. Pennycook, H. M. Li, Z. Liu, *Nano Energy* **2019**, *61*, 54.

[46] Z. Y. Jiang, X. Z. Liang, H. L. Zheng, Y. Y. Liu, Z. Y. Wang, P. Wang, X. Y. Zhang, X. Y. Qin, Y. Dai, M. H. Whangbo, B. B. Huang, *Appl. Catal., B* **2017**, *219*, 209.

[47] J. H. Kim, G. Magesh, H. J. Kang, M. Banu, J. H. Kim, J. Lee, J. S. Lee, *Nano Energy* **2015**, *15*, 153.

[48] K. Teramura, S. Iguchi, Y. Mizuno, T. Shishido, T. Tanaka, *Angew. Chem. Int. Ed.* **2012**, *51*, 8008.

[49] T. Ye, W. M. Huang, L. M. Zeng, M. L. Li, J. L. Shi, *Appl. Catal., B* **2017**, *210*, 141.

[50] H. Y. Jiang, K. Katsumata, J. Hong, A. Yamaguchi, K. Nakata, C. Terashima, N. Matsushita, M. Miyauchi, A. Fujishima, *Appl. Catal., B* **2018**, *224*, 783.

[51] J. G. Hou, S. Y. Cao, Y. Z. Wu, F. Liang, L. Ye, Z. S. Lin, L. C. Sun, *Nano Energy* **2016**, *30*, 59.

[52] X. H. Lin, Y. L. Gao, M. Jiang, Y. F. Zhang, Y. D. Hou, W. X. Dai, S. B. Wang, Z. X. Ding, *Appl. Catal., B* **2018**, *224*, 1009.

[53] J. Chen, J. Yin, X. P. Zheng, H. A. Ahsaine, Y. Zhou, C. W. Dong, O. F. Mohammed, K. Takanabe, O. M. Bakr, *ACS Energy Lett.* **2019**, *4*, 1279.

[54] Z. P. Zeng, Y. B. Yan, J. Chen, P. Zan, Q. H. Tian, P. Chen, *Adv. Funct. Mater.* **2019**, *29*, 1806500.

[55] S. W. Cao, B. J. Shen, T. Tong, J. W. Fu, J. G. Yu, *Adv. Funct. Mater.* **2018**, *28*, 1800136.

[56] K. M. Choi, D. Kim, B. Rungtaweevoranit, C. A. Trickett, J. T. D. Barmanbek, A. S. Alshammari, P. D. Yang, O. M. Yaghi, *J. Am. Chem. Soc.* **2017**, *139*, 356.

[57] Y. Wang, N. Y. Huang, J. Q. Shen, P. Q. Liao, X. M. Chen, J. P. Zhang, *J. Am. Chem. Soc.* **2018**, *140*, 38.

[58] N. Li, J. Liu, J. J. Liu, L. Z. Dong, Z. F. Xin, Y. L. Teng, Y. Q. Lan, *Angew. Chem. Int. Ed.* **2019**, *58*, 5226.

[59] C. G. Hu, L. M. Dai, *Adv. Mater.* **2019**, *31*, 1804672.

[60] L. M. Dai, Y. H. Xue, L. T. Qu, H. J. Choi, J. B. Baek, *Chem. Rev.* **2015**, *115*, 4823.

[61] A. Erdemir, G. Ramirez, O. L. Eryilmaz, B. Narayanan, Y. Liao, G. Kamath, S. K. R. S. Sankaranarayanan, *Nature* **2016**, *536*, 67.

[62] R. M. Izatt, S. R. Izatt, R. L. Bruening, N. E. Izatta, B. A. Moyer, *Chem. Soc. Rev.* **2014**, *43*, 2451.

[63] C. G. Hu, Y. Lin, J. W. Connell, H. M. Cheng, Y. Gogotsi, M. M. Titirici, L. M. Dai, *Adv. Mater.* **2019**, *31*, 1806128.

[64] S. Liu, H. B. Yang, X. Su, J. Ding, Q. Mao, Y. Q. Huang, T. Zhang, B. Liu, *J. Energy Chem.* **2019**, *36*, 95.

[65] M. L. Zhang, C. Choi, R. P. Huo, G. H. Gu, S. Hong, C. Yan, S. Y. Xu, A. W. Robertson, J. S. Qiu, Y. Jung, Z. Y. Sun, *Nano Energy* **2020**, *68*, 104323.

[66] J. X. Low, B. Cheng, J. G. Yu, M. Jaroniec, *Energy Storage Mater.* **2016**, *3*, 24.

[67] J. X. Low, J. G. Yu, W. K. Ho, *J. Phys. Chem. Lett.* **2015**, *6*, 4244.

[68] R. Kuriki, K. Maeda, *Phys. Chem. Chem. Phys.* **2017**, *19*, 4938.

[69] Z. X. Sun, H. Q. Wang, Z. B. Wu, L. Z. Wang, *Catal. Today* **2018**, *300*, 160.

[70] S. Ali, A. Razzaq, S. I. In, *Catal. Today* **2019**, *335*, 39.

[71] J. Mao, K. Li, T. Y. Peng, *Catal. Sci. Technol.* **2013**, *3*, 2481.

[72] H. Tong, S. X. Ouyang, Y. P. Bi, N. Umezawa, M. Oshikiri, J. H. Ye, *Adv. Mater.* **2012**, *24*, 229.

[73] K. Maeda, *Adv. Mater.* **2019**, *31*, 1808205.

[74] Y. Sohn, W. X. Huang, F. Taghipour, *Appl. Surf. Sci.* **2016**, *396*, 1696.

[75] H. H. Chen, C. E. Nanayakkara, V. H. Grassian, *Chem. Rev.* **2012**, *112*, 5919.

[76] R. Shi, G. I. N. Waterhouse, T. Zhang, *Sol. RRL* **2017**, *1*, 1700126.

[77] X. C. Duan, J. T. Xu, Z. X. Wei, J. M. Ma, S. J. Guo, S. Y. Wang, H. K. Liu, S. X. Dou, *Adv. Mater.* **2017**, *29*, 1701784.

[78] W. Leitner, Coord., *Chem. Rev.* **1996**, *153*, 257.

[79] L. Zhang, Z. J. Zhao, J. L. Gong, *Angew. Chem., Int. Ed.* **2017**, *38*, 11326.

[80] Z. Y. Sun, N. Talreja, H. C. Tao, J. Texter, M. Muhler, J. Strunk, J. F. Chen, *Angew. Chem., Int. Ed.* **2018**, *57*, 7610.

[81] S. N. Habisreutinger, L. Schmidt-Mende, J. K. Stolarczyk, *Angew. Chem., Int. Ed.* **2013**, *52*, 7372.

[82] W. J. Yin, M. Krack, B. Wen, S. Y. Ma, L. M. Liu, *J. Phys. Chem. Lett.* **2015**, *6*, 2538.

[83] X. G. Meng, S. X. Ouyang, T. Kako, P. Li, Q. Yu, T. Wang, J. H. Ye, *Chem. Commun.* **2014**, *50*, 11517.

[84] V. P. Indrakanti, J. D. Kubicki, H. H. Schobert, *Energy Environ. Sci.* **2009**, *2*, 745.

[85] X. X. Chang, T. Wang, J. L. Gong, *Energy Environ. Sci.* **2016**, *9*, 2177.

1900546 (37 of 41)

[86] J. L. White, M. F. Baruch, J. E. Pander III, Y. Hu, I. C. Fortmeyer, J. E. Park, T. Zhang, K. Liao, J. Gu, Y. Yan, T. W. Shaw, E. Abelev, A. B. Bocarsly, *Chem. Rev.* **2015**, *115*, 12888.

[87] J. Y. Choi, C. K. Lim, B. Park, M. Kim, A. Jamalb, H. Song, *J. Mater. Chem. A* **2019**, *7*, 15068.

[88] B. Tahir, M. Tahir, N. A. S. Amin, *Appl. Surf. Sci.* **2017**, *419*, 875.

[89] Z. Mo, X. W. Zhu, Z. F. Jiang, Y. H. Song, D. B. Liu, H. P. Li, X. F. Yang, Y. B. She, Y. C. Lei, S. Q. Yuan, H. M. Li, L. Song, Q. Y. Yan, H. Xu, *Appl. Catal., B* **2019**, *256*, 117854.

[90] M. L. Li, L. X. Zhang, X. Q. Fan, M. Y. Wu, M. Wang, R. L. Cheng, L. L. Zhang, H. L. Yao, J. L. Shi, *Appl. Catal., B* **2017**, *201*, 629.

[91] W. Y. Chen, B. Han, C. Tian, X. M. Liu, S. J. Liang, H. Deng, Z. Lin, *Appl. Catal., B* **2019**, *244*, 996.

[92] Z. Y. Sun, Q. Fan, M. L. Zhang, S. Z. Liu, H. C. Tao, J. Texter, *Adv. Sci.* **2019**, *6*, 1901084.

[93] Z. F. Jiang, W. M. Wan, H. M. Li, S. Q. Yuan, H. J. Zhao, P. K. Wong, *Adv. Mater.* **2018**, *30*, 1706108.

[94] Y. Wang, S. B. Wang, X. W. (David) Lou, *Angew. Chem., Int. Ed.* **2019**, *58*, 17236.

[95] M. Wang, M. Shen, X. X. Jin, J. J. Tian, M. L. Li, Y. J. Zhou, L. X. Zhang, Y. S. Li, J. L. Shi, *ACS Catal.* **2019**, *9*, 4573.

[96] B. B. Hu, M. C. Hu, Q. Guo, K. Wang, X. T. Wang, *Appl. Catal., B* **2019**, *253*, 77.

[97] C. T. Campbell, C. H. F. Peden, *Science* **2005**, *309*, 713.

[98] J. Di, C. Zhu, M. X. Ji, M. L. Duan, R. Long, C. Yan, K. Z. Gu, J. Xiong, Y. B. She, J. X. Xia, H. M. Li, Z. Liu, *Angew. Chem., Int. Ed.* **2018**, *130*, 15063.

[99] J. Wu, X. D. Li, W. Shi, P. Q. Ling, Y. F. Sun, X. C. Jiao, S. Gao, L. Liang, J. Q. Xu, W. S. Yan, C. M. Wang, Y. Xie, *Angew. Chem., Int. Ed.* **2018**, *57*, 8719.

[100] E. Karamian, S. Sharifnia, *J. CO₂ Util.* **2016**, *16*, 194.

[101] N. Sasirekha, S. J. S. Basha, K. Shanthi, *Appl. Catal., B* **2006**, *62*, 169.

[102] K. Mori, H. Yamashita, M. Anpo, *RSC Adv.* **2012**, *2*, 3165.

[103] I. A. Shkrob, T. W. Marin, H. Y. He, P. Zapol, *J. Phys. Chem. C* **2012**, *116*, 9450.

[104] F. Fresno, I. J. Villar-García, L. Collado, E. Alfonso-González, P. Reñones, M. Barawi, V. A. de la Peña O'Shea, *J. Phys. Chem. Lett.* **2018**, *9*, 7192.

[105] A. Corma, H. Garcia, *J. Catal.* **2013**, *308*, 168.

[106] N. N. Vu, S. Kaliaguine, T. O. Do, *Adv. Funct. Mater.* **2019**, *29*, 1901825.

[107] J. W. Fu, K. X. Jiang, X. Q. Qiu, J. G. Yu, M. Liu, *Mater. Today* **2019**, https://doi.org/10.1016/j.mattod.2019.06.009.

[108] J. D. Hong, W. Zhang, J. Ren, R. Xu, *Anal. Methods* **2013**, *5*, 1086.

[109] A. Pougin, M. Dilla, J. Strunk, *Phys. Chem. Chem. Phys.* **2016**, *18*, 10809.

[110] G. G. Liu, X. G. Meng, H. B. Zhang, G. X. Zhao, H. Pang, T. Wang, P. Li, T. Kako, J. H. Ye, *Angew. Chem., Int. Ed.* **2017**, *56*, 5570.

[111] K. S. Novoselov, A. K. Geim, S. V. Morozov, D. Jiang, Y. Zhang, S. V. Dubonos, I. V. Grigorieva, A. A. Firsov, *Science* **2004**, *306*, 666.

[112] Q. J. Xiang, J. G. Yu, M. Jaroniec, *Chem. Soc. Rev.* **2012**, *41*, 782.

[113] T. Ma, Q. Fan, X. Li, J. S. Qiu, T. B. Wu, Z. Y. Sun, *J. CO₂ Util.* **2019**, *30*, 168.

[114] H. Q. Sun, S. B. Wang, *Energy Fuels* **2014**, *28*, 22.

[115] B. Luo, G. Liu, L. Z. Wang, *Nanoscale* **2016**, *8*, 6904.

[116] J. X. Low, S. W. Cao, J. G. Yu, S. Wageh, *Chem. Commun.* **2014**, *50*, 10768.

[117] Q. J. Xiang, B. Cheng, J. G. Yu, *Angew. Chem. Int. Ed.* **2015**, *54*, 11350.

[118] W. G. Tu, Y. Zhou, Z. G. Zou, *Adv. Funct. Mater.* **2013**, *23*, 4996.

[119] Y. T. Liang, B. J. K. Vijayan, K. A. Gray, M. C. Hersam, *Nano Lett.* **2011**, *11*, 2865.

[120] L. Wibmer, L. M. O. Lourenco, A. Roth, G. Katsukis, M. G. P. M. S. Neves, J. A. S. Cavaleiro, J. P. C. Tome, T. Torres, D. M. Guldi, *Nanoscale* **2015**, *7*, 5674.

[121] C. B. Bie, B. C. Zhu, F. Y. Xu, L. Y. Zhang, J. G. Yu, *Adv. Mater.* **2019**, *31*, 1902868.

[122] Z. Y. Wang, Y. Pu, D. Wang, J. X. Wang, J. F. Chen, *Front. Chem. Sci. Eng.* **2018**, *12*, 855.

[123] X. Jiang, J. Nisar, B. Pathak, J. J. Zhao, R. Ahuja, *J. Catal.* **2013**, *299*, 204.

[124] H. C. Hsu, I. Shown, H. Y. Wei, Y. C. Chang, H. Y. Du, Y. G. Lin, C. A. Tseng, C. H. Wang, L. C. Chen, Y. C. Lin, K. H. Chen, *Nanoscale* **2013**, *5*, 262.

[125] I. Shown, H. C. Hsu, Y. C. Chang, C. H. Lin, P. K. Roy, A. Ganguly, C. H. Wang, J. K. Chang, C. I. Wu, L. C. Chen, K. H. Chen, *Nano Lett.* **2014**, *14*, 6097.

[126] Y. Zhao, J. Zhang, L. T. Qu, *ChemNanoMat* **2015**, *1*, 298.

[127] A. Zambon, J. M. Mouesca, C. Gheorghiu, P. A. Bayle, J. Pécaut, M. Claeys-Bruno, S. Gambarelli, L. Dubois, *Chem. Sci.* **2016**, *7*, 945.

[128] K. Maeda, X. C. Wang, Y. Nishihara, D. L. Lu, M. Antonietti, K. Domen, *J. Phys. Chem. C* **2009**, *113*, 4940.

[129] X. C. Wang, K. Maeda, A. Thomas, K. Takanabe, G. Xin, J. M. Carlsson, K. Domen, M. Antonietti, *Nat. Mater.* **2009**, *8*, 76.

[130] S. Z. Liu, S. B. Wang, Y. Jiang, Z. Q. Zhao, G. Y. Jiang, Z. Y. Sun, *Chem. Eng. J.* **2019**, *373*, 572.

[131] W. Yan, Y. Yu, H. H. Zou, X. F. Wang, P. Li, W. Y. Gao, J. Z. Wang, S. M. Wu, K. J. Ding, *Sol. RRL* **2018**, *2*, 1800058.

[132] P. Niu, Y. Q. Yang, J. C. Yu, G. Liu, H. M. Cheng, *Chem. Commun.* **2014**, *50*, 10837.

[133] L. H. Lin, H. H. Ou, Y. F. Zhang, X. C. Wang, *ACS Catal.* **2016**, *6*, 3921.

[134] M. S. Khan, F. K. Zhang, M. Osada, S. S. Mao, S. H. Shen, *Sol. RRL* **2019**, *1900435*. https://doi.org/10.1002/solr.201900435.

[135] P. H. Li, F. Wang, S. Q. Wei, X. Y. Li, Y. Zhou, *Phys. Chem. Chem. Phys.* **2017**, *19*, 4405.

[136] G. Mamba, A. K. Mishra, *Appl. Catal., B* **2016**, *198*, 347.

[137] C. Y. Liu, H. W. Huang, L. Q. Ye, S. X. Yu, N. Tian, X. Du, T. R. Zhang, Y. H. Zhang, *Nano Energy* **2017**, *41*, 738.

[138] F. Ding, D. Yang, Z. W. Tong, Y. H. Nan, Y. J. Wang, X. Y. Zou, Z. Y. Jiang, *Environ. Sci. Nano* **2017**, *4*, 1455.

[139] G. C. Xie, K. Zhang, B. D. Guo, Q. Liu, L. Fang, J. R. Gong, *Adv. Mater.* **2013**, *25*, 3820.

[140] Q. H. Weng, X. B. Wang, X. Wang, Y. Bando, D. Golberg, *Chem. Soc. Rev.* **2016**, *45*, 3989.

[141] R. Shankar, M. Sachs, L. Francàs, D. Lubert-Perquel, G. Kerherve, A. Regoutz, C. Petit, *J. Mater. Chem. A* **2019**, *7*, 23931.

[142] K. X. Zhang, H. Su, H. H. Wang, J. J. Zhang, S. Y. Zhao, W. W. Lei, X. Wei, X. H. Li, J. S. Chen, *Adv. Sci.* **2018**, *5*, 1800062.

[143] C. J. Huang, C. Chen, M. W. Zhang, L. H. Lin, X. X. Ye, S. Lin, M. Antonietti, X. C. Wang, *Nat. Commun.* **2015**, *6*, 7698.

[144] M. Zhou, S. B. Wang, P. J. Yang, C. J. Huang, X. C. Wang, *ACS Catal.* **2018**, *8*, 4928.

[145] M. Steenackers, I. D. Sharp, K. Larsson, N. A. Hutter, M. Stutzmann, R. Jordan, *Chem. Mater.* **2010**, *22*, 272.

[146] M. A. Gondal, M. A. Ali, X. F. Chang, K. Shen, Q. Y. Xu, Z. H. Yamani, *J. Environ. Sci. Health Part A Tox. Hazard. Subst. Environ. Eng.* **2012**, *47*, 1571.

[147] Y. Wang, L. N. Zhang, X. Y. Zhang, Z. Z. Zhang, Y. C. Tong, F. Y. Li, J. C. S. Wu, X. X. Wang, *Appl. Catal., B* **2017**, *206*, 158.

[148] H. Liu, A. T. Neal Z. Zhu, Z. Luo, X. F. Xu, D. Tománek, P. D. Ye, *ACS Nano* **2014**, *8*, 4033.

[149] B. Radisavljevic, A. Radenovic, J. Brivio, V. Giacometti, A. Kis, *Nat. Nanotechnol.* **2011**, *6*, 147.

[150] H. T. Yuan, X. G. Liu, F. Afshinmanesh, W. Li, G. Xu, J. Sun, B. Lian, A. G. Curto, G. J. Ye, Y. Hikita, Z. X. Shen, S. C. Zhang, X. H. Chen, M. Brongersma, H. Y. Hwang, Y. Cui, *Nat. Nanotechnol.* **2015**, *10*, 707.

[151] G. Hu, T. Albrow-Owen, X. Jin, A. Ali, Y. Hu, R. C. T. Howe, K. Shehzad, Z. Yang, X. Zhu, R. I. Woodward, T. C. Wu,

H. Jussila, J. B. Wu, P. Peng, P. H. Tan, Z. Sun, E. J. R. Kelleher, M. Zhang, Y. Xu, T. Hasan, *Nat. Commun.* **2017**, *8*, 278.

[152] J. Shao, H. Xie, H. Hang, Z. Li, Z. Sun, Y. Xu, X. F. Yu, Y. Zhao, H. Zhang, H. Wang, P. K. Chu, *Nat. Commun.* **2016**, *7*, 12967.

[153] C. Q. Han, J. Li, Z. Y. Ma, H. Q. Xie, G. I. N. Waterhouse, L. Q. Ye, T. R. Zhang, *Sci. China. Mater.* **2018**, *61*, 1159.

[154] P. J. Waller, F. Gándara, O. M. Yaghi, *Acc. Chem. Res.* **2015**, *48*, 3053.

[155] Y. Z. Liu, Y. H. Ma, Y. B. Zhao, X. X. Sun, F. Gándara, H. Furukawa, Z. Liu, H. Y. Zhu, C. H. Zhu, K. Suenaga, P. Oleynikov, A. S. Alshammari, X. Zhang, O. Terasaki, O. M. Yaghi, *Science* **2016**, *351*, 365.

[156] Z. H. Xiang, D. P. Cao, L. M. Dai, *Polym. Chem.* **2015**, *6*, 1896.

[157] N. Li, J. J. Du, D. Wu, J. C. Liu, N. Li, Z. W. Sun, G. L. Li, Y. N. Wu, *Trends Anal. Chem.* **2018**, *108*, 154.

[158] N. Chaoui, M. Trunk, R. Dawson, J. Schmidt, A. Thomas, *Chem. Soc. Rev.* **2017**, *46*, 3302.

[159] S. Y. Ding, W. Wang, *Chem. Soc. Rev.* **2013**, *42*, 548.

[160] N. Huang, P. Wang, D. L. Jiang, *Nat. Rev. Mater.* **2016**, *1*, 16068.

[161] M. Lu, J. Liu, Q. Li, M. Zhang, M. Liu, J. L. Wang, D. Q. Yuan, Y. Q. Lan, *Angew. Chem., Int. Ed.* **2019**, *131*, 12522.

[162] Z. P. Li, Y. F. Zhi, P. P. Shao, H. Xia, G. S. Li, X. Feng, X. Chen, Z. Shi, X. M. Liu, *Appl. Catal., B* **2019**, *245*, 334.

[163] E. Q. Jin, Z. A. Lan, Q. H. Jiang, K. Y. Geng, G. S. Li, X. C. Wang, D. L. Jiang, *Chem* **2019**, *5*, 1632.

[164] S. Z. Yang, W. H. Hu, X. Zhang, P. L. He, B. Pattengale, C. M. Liu, M. Cendejas, I. Hermans, X. Y. Zhang, J. Zhang, J. E. Huang, *J. Am. Chem. Soc.* **2018**, *140*, 14614.

[165] Y. H. Fu, X. L. Zhu, L. Huang, X. C. Zhang, F. M. Zhang, W. D. Zhu, *Appl. Catal., B* **2018**, *239*, 46.

[166] S. E. Guo, H. Y. Zhang, Y. Chen, Z. H. Liu, B. Yu, Y. F. Zhao, Z. Z. Yang, B. X. Han, Z. M. Liu, *ACS Catal.* **2018**, *8*, 4576.

[167] Z. F. Jiang, H. L. Sun, T. Q. Wang, B. Wang, W. Wei, H. M. Li, S. Q. Yuan, A. C. An, H. J. Zhao, J. G. Yu, P. K. Wong, *Energy Environ. Sci.* **2018**, *11*, 2382.

[168] Y. J. Ren, D. Q. Zeng, W. J. Ong, *Chin. J. Catal.* **2019**, *40*, 289.

[169] J. W. Fu, B. C. Zhu, C. J. Jiang, B. Cheng, W. You, J. G. Yu, *Small* **2017**, *13*, 1603938.

[170] B. Liu, L. Q. Ye, R. Wang, J. F. Yang, Y. X. Zhang, R. Guan, L. H. Tian, X. B. Chen, *ACS Appl. Mater. Interfaces* **2018**, *10*, 4001.

[171] K. Wang, Q. Li, B. S. Liu, B. Cheng, W. K. Ho, J. G. Yu, *Appl. Catal., B* **2015**, *176–177*, 44.

[172] F. S. Xing, Q. W. Liu, M. X. Song, C. J. Huang, *ChemCatChem* **2018**, *10*, 5270.

[173] K. Wang, J. L. Fu, Y. Zheng, *Appl. Catal., B* **2019**, *254*, 270.

[174] S. P. Wan, M. Ou, X. M. Wang, Y. N. Wang, Y. Q. Zeng, J. Ding, S. L. Zhang, Q. Zhong, *Dalton Trans.* **2019**, *48*, 12070.

[175] Y. G. Wang, Y. L. Xu, Y. Z. Wang, H. F. Qin, X. Li, Y. H. Zuo, S. F. Kang, L. F. Cui, *Catal. Commun.* **2016**, *75*, 74.

[176] Z. X. Sun, S. C. Wang, Q. Li, M. Q. Lyu, T. Butburee, B. Luo, H. Q. Wang, J. M. T. A. Fischer, C. Zhang, Z. B. Wu, L. Z. Wang, *Adv. Sustainable Syst.* **2017**, *1*, 1700003.

[177] J. Y. Tang, R. T. Guo, W. G. Pan, W. G. Zhou, C. Y. Huang, *Appl. Surf. Sci.* **2019**, *467–468*, 206.

[178] M. Lu, Q. Li, J. Liu, F. M. Zhang, L. Zhang, J. L. Wang, Z. H. Kang, Y. Q. Lan, *Appl. Catal., B* **2019**, *254*, 624.

[179] J. S. Zhang, J. H. Sun, K. Maeda, K. Domen, P. Liu, M. Antonietti, X. Z. Fu, X. C. Wang, *Energy Environ. Sci.* **2011**, *4*, 675.

[180] N. Sagara, S. Kamimura, T. Tsubota, T. Ohno, *Appl. Catal., B* **2016**, *192*, 193.

[181] K. S. Lakhi, D. H. Park, K. A. Bahily, W. Cha, B. Viswanathan, J. H. Choy, A. Vinu, *Chem. Soc. Rev.* **2017**, *46*, 72.

[182] B. X. Zhou, S. S. Ding, B. J. Zhang, L. Xu, R. S. Chen, L. Luo, W. Q. Huang, Z. Xie, A. L. Pan, G. F. Huang, *Appl. Catal., B* **2019**, *254*, 321.

[183] X. Y. Qian, X. Q. Meng, J. W. Sun, L. L. Jiang, Y. N. Wang, J. L. Zhang, X. M. Hu, M. Shalom, J. W. Zhu, *ACS Appl. Mater. Interfaces* **2019**, *11*, 27226.

[184] N. Tian, H. W. Huang, X. Du, F. Dong, Y. H. Zhang, *J. Mater. Chem. A* **2019**, *7*, 11584.

[185] P. F. Xia, B. C. Zhu, J. G. Yu, S. W. Cao, M. Jaroniec, *J. Mater. Chem. A* **2017**, *5*, 3230.

[186] S. P. Wan, M. Ou, Q. Zhong, W. Cai, *Carbon* **2018**, *138*, 465.

[187] M. J. Liu, S. Wageh, A. A. Al-Ghamdi, P. F. Xia, B. Cheng, L. Y. Zhang, J. G. Yu, *Chem. Commun.* **2019**, *55*, 14023.

[188] J. Wang, S. W. Cao, J. G. Yu, *Sol. RRL* **2019**, 1900469. https://doi.org/10.1002/solr.201900469.

[189] G. H. Dong, D. L. Jacobs, L. Zang, C. Y. Wang, *Appl. Catal., B* **2017**, *218*, 515.

[190] P. J. Yang, H. Y. Zhuzhang, R. R. Wang, W. Lin, X. C. Wang, *Angew. Chem., Int. Ed.* **2019**, *131*, 1146.

[191] H. N. Shi, S. R. Long, J. G. Hou, L. Ye, Y. W. Sun, W. J. Ni, C. S. Song, K. Y. Li, G. G. Gurzadyan, X. W. Guo, *Chem. Eur. J.* **2019**, *25*, 5028.

[192] W. G. Tu, Y. Xu, J. J. Wang, B. W. Zhang, T. H. Zhou, S. M. Yin, S. Y. Wu, C. M. Li, Y. Z. Huang, Y. Zhou, Z. G. Zou, J. Robertson, M. Kraft, R. Xu, *ACS Sustainable Chem. Eng.* **2017**, *5*, 7260.

[193] M. Shen, L. X. Zhang, M. Wang, J. J. Tian, X. X. Jin, L. M. Guo, L. Z. Wang, J. L. Shi, *J. Mater. Chem. A* **2019**, *7*, 1556.

[194] P. F. Xia, M. Antonietti, B. C. Zhu, T. Heil, J. G. Yu, S. W. Cao, *Adv. Funct. Mater.* **2019**, *29*, 1900093.

[195] J. N. Qin, S. B. Wang, H. Ren, Y. D. Hou, X. C. Wang, *Appl. Catal., B* **2015**, *179*, 1.

[196] L. M. Wang, W. L. Chen, D. D. Zhang, Y. P. Du, R. Amal, S. Z. Qiao, J. B. Wu, Z. Y. Yin, *Chem. Soc. Rev.* **2019**, *48*, 5310.

[197] Q. Huang, J. G. Yu, S. W. Cao, C. Cui, B. Cheng, *Appl. Surf. Sci.* **2015**, *358*, 350.

[198] X. L. Liu, P. Wang, H. S. Zhai, Q. Q. Zhang, B. B. Huang, Z. Y. Wang, Y. Y. Liu, Y. Dai, X. Y. Qin, X. Y. Zhang, *Appl. Catal., B* **2018**, *232*, 521.

[199] X. Li, J. G. Yu, M. Jaroniec, X. B. Chen, *Chem. Rev.* **2019**, *119*, 3962.

[200] J. R. Ran, M. Jaroniec, S. Z. Qiao, *Adv. Mater.* **2018**, *30*, 1704649.

[201] S. Bai, X. J. Wang, C. Y. Hu, M. L. Xie, J. Jiang, Y. J. Xiong, *Chem. Commun.* **2014**, *50*, 6094.

[202] S. W. Cao, Y. Li, B. C. Zhu, M. Jaroniec, J. G. Yu, *J. Catal.* **2017**, *349*, 208.

[203] Q. Q. Lang, W. L. Hu, P. H. Zhou, T. L. Huang, S. X. Zhong, L. N. Yang, J. R. Chen, S. Bai, *Nanotechnology* **2017**, *28*, 484003.

[204] W. J. Ong, L. L. Tan, S. P. Chai, S. T. Yong, *Dalton Trans.* **2015**, *44*, 1249.

[205] X. Li, C. Y. Liu, D. Y. Wu, J. Z. Li, P. W. Huo, H. Q. Wang, *Chin. J. Catal.* **2019**, *40*, 928.

[206] M. Humayun, Q. Y. Fu, Z. P. Zheng, H. L. Li, W. Luo, *Appl. Catal., A* **2018**, *568*, 139.

[207] J. L. Lin, Z. M. Pan, X. C. Wang, *ACS Sustainable Chem. Eng.* **2014**, *2*, 353.

[208] G. D. Shi, L. Yang, Z. W. Liu, X. Chen, J. Q. Zhou, Y. Yu, *Appl. Surf. Sci.* **2018**, *427*, 1165.

[209] J. Y. Tang, W. G. Zhou, R. T. Guo, C. Y. Huang, W. G. Pan, *Catal. Commun.* **2018**, *107*, 92.

[210] Q. Li, Z. X. Sun, H. Q. Wang, Z. B. Wu, *J. CO₂ Util.* **2018**, *28*, 126.

[211] R. Y. Zhang, P. H. Li, F. Wang, L. Q. Ye, A. Gaur, Z. A. Huang, Z. Y. Zhao, Y. Bai, Y. Zhou, *Appl. Catal., B* **2019**, *250*, 273.

[212] H. H. Ou, C. Tang, Y. F. Zhang, A. M. Asiri, M. M. Titirici, X. C. Wang, *J. Catal.* **2019**, *375*, 104.

[213] P. P. Huang, J. H. Huang, S. A. Pantovich, A. D. Carl, T. G. Fenton, C. A. Caputo, R. L. Grimm, A. I. Frenkel, G. H. Li, *J. Am. Chem. Soc.* **2018**, *140*, 16042.

[214] W. F. Zhong, R. J. Sa, L. Y. Li, Y. J. He, L. Y. Li, J. H. Bi, Z. Y. Zhuang, Y. Yu, Z. G. Zou, *J. Am. Chem. Soc.* **2019**, *141*, 7615.

[215] F. Raziq, Y. Qu, M. Humayun, A. Zada, H. T. Yu, L. Q. Jing, *Appl. Catal., B* **2017**, *201*, 486.

[216] H. J. W. Li, H. M. Zhou, K. J. Chen, K. Liu, S. Li, K. X. Jiang, W. H. Zhang, Y. B. Xie, Z. Cao, H. M. Li, H. Liu, X. W. Xu, H. Pan, J. H. Hu, D. S. Tang, X. Q. Qiu, J. W. Fu, M. Liu, *Sol. RRL* **2019**, 1900416. https://doi.org/10.1002/solr.201900416.

[217] X. X. Zhang, K. Hu, X. L. Zhang, W. Ali, Z. J. Li, Y. Qu, H. Wang, Q. Y. Zhang, L. Q. Jing, *Appl. Surf. Sci.* **2019**, *492*, 125.

[218] S. F. Tang, X. P. Yin, G. Y. Wang, X. L. Lu, T. B. Lu, *Nano Res.* **2019**, *12*, 457.

[219] C. Q. Han, R. M. Zhang, Y. H. Ye, L. Wang, Z. Y. Ma, F. Y. Su, H. Q. Xie, Y. Zhou, P. K. Wong, L. Q. Ye, *J. Mater. Chem. A* **2019**, *7*, 9726.

[220] L. H. Zhao, F. Ye, D. M. Wang, X. T. Cai, C. C. Meng, H. S. Xie, J. L. Zhang, S. Bai, *ChemSusChem* **2018**, *11*, 3524.

[221] W. J. Ong, L. L. Tan, S. P. Chai, S. T. Yong, *Chem. Commun.* **2015**, *51*, 858.

[222] M. Rakibuddin, H. Kim, *Beilstein J. Nanotechnol.* **2019**, *10*, 448.

[223] C. Han, Y. P. Lei, B. Wang, Y. D. Wang, *ChemSusChem* **2018**, *11*, 4237.

[224] W. J. Ong, L. K. Putri, Y. C. Tan, L. L. Tan, N. Li, Y. H. Ng, X. M. Wen, S. P. Chai, *Nano Res.* **2017**, *10*, 1673.

[225] H. J. Feng, Q. Q. Guo, Y. F. Xu, T. Chen, Y. Y. Zhou, Y. G. Wang, M. Z. Wang, D. S. Shen, *ChemSusChem* **2018**, *11*, 4256.

[226] F. Y. Xu, K. Meng, B. C. Zhu, H. B. Liu, J. S. Xu, J. G. Yu, *Adv. Funct. Mater.* **2019**, *29*, 1904256.

[227] B. Kumar, M. Llorente, J. Froehlich, T. Dang, A. Sathrum, C. P. Kubiak, *Annu. Rev. Phys. Chem.* **2012**, *63*, 541.

[228] Y. R. Li, T. T. Kong, S. H. Shen, *Small* **2019**, *15*, 1900772.

[229] K. Maeda, K. Sekizawa, O. Ishitani, *Chem. Commun.* **2013**, *49*, 10127.

[230] K. Wada, C. S. K. Ranasinghe, R. Kuriki, A. Yamakata, O. Ishitani, K. Maeda, *ACS Appl. Mater. Interfaces* **2017**, *9*, 23869.

[231] A. Kumar, P. Kumar, R. Borkar, A. Bansiwal, N. Labhsetwar, S. L. Jain, *Carbon* **2017**, *123*, 371.

[232] K. Maeda, R. Kuriki, M. W. Zhang, X. C. Wang, O. Ishitani, *J. Mater. Chem. A* **2014**, *2*, 15146.

[233] R. Kuriki, O. Ishitani, K. Maeda, *ACS Appl. Mater. Interfaces* **2016**, *8*, 6011.

[234] R. Kuriki, K. Sekizawa, O. Ishitani, *Angew. Chem., Int. Ed.* **2015**, *54*, 2406.

[235] C. Tsounis, R. Kuriki, K. Shibata, J. J. M. Vequizo, D. L. Lu, A. Yamakata, O. Ishitani, R. Amal, K. Maeda, *ACS Sustainable Chem. Eng.* **2018**, *6*, 15333.

[236] L. Shi, T. Wang, H. B. Zhang, K. Chang, J. H. Ye, *Adv. Funct. Mater.* **2015**, *25*, 5360.

[237] G. X. Zhao, H. Pang, G. G. Liu, P. Li, H. M. Liu, H. B. Zhang, L. Shi, J. H. Ye, *Appl. Catal., B* **2017**, *200*, 141.

[238] G. L. Xu, H. B. Zhang, J. Wei, H. X. Zhang, X. Wu, Y. Li, C. S. Li, J. Zhang, J. H. Ye, *ACS Nano* **2018**, *12*, 5333.

[239] L. Lin, C. C. Hou, X. H. Zhang, Y. J. Wang, Y. Chen, T. He, *Appl. Catal., B* **2018**, *221*, 312.

[240] C. Cometto, R. Kuriki, L. J. Chen, K. Maeda, T. C. Lau, O. Ishitani, M. Robert, *J. Am. Chem. Soc.* **2018**, *140*, 7437.

[241] S. Roy, E. Reisner, *Angew. Chem., Int. Ed.* **2019**, *58*, 12180.

[242] Y. P. Yuan, S. W. Cao, Y. S. Liao, L. S. Yin, C. Xue, *Appl. Catal., B* **2013**, *140–141*, 164.

[243] X. J. Zhang, L. Wang, Q. C. Du, Z. Y. Wang, S. G. Ma, M. Yu, *J. Colloid Interface Sci.* **2016**, *464*, 89.

[244] S. W. Cao, X. F. Liu, Y. P. Yuan, Z. Y. Zhang, Y. S. Liao, J. Fang, S. C. J. Loo, T. C. Sum, C. Xue, *Appl. Catal., B* **2014**, *147*, 940.

[245] J. D. Hong, W. Zhang, Y. B. Wang, T. H. Zhou, R. Xu, *ChemCatChem* **2014**, *6*, 2315.

[246] M. L. Li, L. X. Zhang, M. Y. Wu, Y. Y. Du, X. Q. Fan, M. Wang, L. L. Zhang, Q. L. Kong, J. L. Shi, *Nano Energy* **2016**, *19*, 145.

[247] Y. M. He, Y. Wang, L. H. Zhang, B. T. Teng, M. H. Fan, *Appl. Catal., B* **2015**, *168–169*, 1.

[248] L. K. Putri, W. J. Ong, W. S. Chang, S. P. Chai, *Catal. Sci. Technol.* **2016**, *6*, 744.

[249] W. J. Ong, L. K. Putri, L. L. Tan, S. P. Chai, S. T. Yong, *Appl. Catal., B* **2016**, *180*, 530.

[250] M. Reli, P. W. Huo, M. Šihor, N. Ambrožová, I. Troppová, L. Matějová, J. Lang, L. Svoboda, P. Kuśtrowski, M. Ritz, P. Praus, K. Kočí, *J. Phys. Chem. A* **2016**, *120*, 8564.

[251] A. Zada, N. Ali, F. Subhan, N. Anwar, M. I. A. Shah, M. Ateeq, Z. Hussain, K. Zaman, M. Khan, *Prog. Nat. Sci. Mater.* **2019**, *29*, 138.

[252] A. Crake, K. C. Christoforidis, R. Godin, B. Moss, A. Kafizas, S. Zafeiratos, J. R. Durrant, C. Petit, *Appl. Catal., B* **2019**, *242*, 369.

[253] H. N. Shi, S. R. Long, S. Hu, J. G. Hou, W. J. Ni, C. S. Song, K. Y. Li, G. G. Gurzadyan, X. W. Guo, *Appl. Catal., B* **2019**, *245*, 760.

[254] F. Raziq, Y. Qu, X. L. Zhang, M. Humayun, J. Wu, A. Zada, H. T. Yu, X. J. Sun, L. Q. Jing, *J. Phys. Chem. C* **2016**, *120*, 98.

[255] L. H. Zhao, L. H. Zhang, H. J. Lin, Q. Y. Nong, M. Cui, Y. Wu, Y. M. He, *J. Hazard. Mater.* **2015**, *299*, 333.

[256] H. Liu, Z. Zhang, J. C. Meng, J. Zhang, *Mol. Catal.* **2017**, *430*, 9.

[257] A. Li, T. Wang, C. C. Li, Z. Q. Huang, Z. B. Luo, J. L. Gong, *Angew. Chem., Int. Ed.* **2019**, *131*, 3844.

[258] J. Zhou, W. C. Chen, C. Y. Sun, L. Han, C. Qin, M. M. Chen, X. L. Wang, E. Wang, Z. M. Su, *ACS Appl. Mater. Interfaces* **2017**, *9*, 11689.

[259] M. Ou, W. G. Tu, S. M. Yin, W. N. Xing, S. Y. Wu, H. J. Wang, S. P. Wan, Q. Zhong, R. Xu, *Angew. Chem., Int. Ed.* **2018**, *130*, 13758.

[260] J. Y. Tang, R. T. Guo, W. G. Zhou, C. Y. Huang, W. G. Pan, *Appl. Catal., B* **2018**, *237*, 802.

[261] A. Bafaqeer, M. Tahir, N. A. S. Amin, *Appl. Catal., B* **2019**, *242*, 312.

[262] C. Y. Hu, J. Zhou, C. Y. Sun, M. M. Chen, X. L. Wang, Z. M. Su, *Chem. Eur. J.* **2019**, *25*, 379.

[263] L. Q. Yang, J. F. Huang, L. Shi, L. Y. Cao, H. M. Liu, Y. Y. Liu, Y. X. Li, H. Song, Y. N. Jie, J. H. Ye, *Appl. Catal., B* **2018**, *221*, 670.

[264] B. B. Jin, G. D. Yao, F. M. Jin, Y. H. Hu, *Catal. Today* **2018**, *316*, 149.

[265] M. Tahir, B. Tahir, M. G. M. Nawawi, M. Hussain, A. Muhammad, *Appl. Surf. Sci.* **2019**, *485*, 450.

[266] Y. Xia, Z. H. Tian, T. Heil, A. Y. Meng, B. Cheng, S. W. Cao, J. G. Yu, M. Antonietti, *Joule* **2019**, *3*, 2792.

[267] M. F. Liang, T. Borjigin, Y. H. Zhang, B. H. Liu, H. Liu, H. Guo, *Appl. Catal., B* **2019**, *243*, 566.

[268] S. Tonda, S. Kumar, M. Bhardwaj, P. Yadav, S. Ogale, *ACS Appl. Mater. Interfaces* **2018**, *10*, 2667.

[269] H. F. Shi, G. Q. Chen, C. L. Zhang, Z. G. Zou, *ACS Catal.* **2014**, *4*, 3637.

[270] M. Zhou, S. B. Wang, P. J. Yang, Z. S. Luo, R. S. Yuan, A. M. Asiri, M. Wakeel, X. C. Wang, *Chem. Eur. J.* **2018**, *24*, 18529.

[271] Z. M. Sun, W. Fang, L. Zhao, H. Chen, X. He, W. X. Li, P. Tian, Z. H. Huang, *Environ. Int.* **2019**, *130*, 104898.

[272] A. Kumar, P. K. Prajapati, M. S. Aathira, A. Bansiwal, R. Boukherroub, S. L. Jain, *J. Colloid Interface Sci.* **2019**, *543*, 201.

[273] S. Zhou, Y. Liu, J. M. Li, Y. J. Wang, G. Y. Jiang, Z. Zhao, D. X. Wang, A. Duan, J. Liu, Y. C. Wei, *Appl. Catal., B* **2014**, *158–159*, 20.

[274] H. L. Li, Y. Gao, X. Y. Wu, P. H. Lee, K. Shih, *Appl. Surf. Sci.* **2017**, *402*, 198.

[275] D. O. Adekoya, M. Tahir, N. A. S. Amin, *J. CO2 Util.* **2017**, *18*, 261.

[276] A. Kumar, A. Kumar, G. Sharma, A. H. Al-Muhtaseb, M. Naushad, A. A. Ghfar, C. S. Guo, F. J. Stadler, *Chem. Eng. J.* **2018**, *339*, 393.

[277] Y. Xu, Y. You, H. W. Huang, Y. X. Guo, Y. H. Zhang, *J. Hazard. Mater.* **2020**, *381*, 121159.

[278] R. Marschall, *Adv. Funct. Mater.* **2014**, *24*, 2421.

[279] H. J. Li, W. G. Tu, Y. Zhou, Z. G. Zou, *Adv. Sci.* **2016**, *3*, 1500389.

[280] Y. M. He, L. H. Zhang, B. T. Teng, M. H. Fan, *Environ. Sci. Technol.* **2015**, *49*, 649.

[281] Y. M. He, L. H. Zhang, M. H. Fan, X. X. Wang, M. L. Walbridge, Q. Y. Nong, Y. Wu, L. H. Zhao, *Sol. Energy Mater. Sol. Cells* **2015**, *137*, 175.

[282] J. C. Wang, H. C. Yao, Z. Y. Fan, L. Zhang, J. S. Wang, S. Q. Zang, Z. J. Li, *ACS Appl. Mater. Interfaces* **2016**, *8*, 3765.

[283] M. Wang, M. Shen, L. X. Zhang, J. J. Tian, X. X. Jin, Y. J. Zhou, J. L. Shi, *Carbon* **2017**, *120*, 23.

[284] H. W. Guo, M. Q. Chen, Q. Zhong, Y. N. Wang, W. H. Ma, J. Ding, *J. CO$_2$ Util.* **2019**, *33*, 233.

[285] D. F. Xu, B. Cheng, W. K. Wang, C. J. Jiang, J. G. Yu, *Appl. Catal., B* **2018**, *231*, 368.

[286] N. T. T. Truc, N. T. Hanh, M. V. Nguyen, N. T. P. L. Chi, N. V. Noi, D. T. Tran, M. N. Ha, D. Q. Trung, T. D. Pham, *Appl. Surf. Sci.* **2018**, *457*, 968.

[287] N. T. T. Truc, L. G. Bach, N. T. Hanh, T. D. Pham, N. T. P. L. Chi, D. T. Tran, M. V. Nguyen, V. N. Nguyen, *J. Colloid Interface Sci.* **2019**, *540*, 1.

[288] T. M. Di, B. C. Zhu, B. Cheng, J. G. Yu, J. S. Xu, *J. Catal.* **2017**, *352*, 532.

[289] M. L. Li, L. X. Zhang, X. Q. Fan, Y. J. Zhou, M. Y. Wu, J. L. Shi, *J. Mater. Chem. A* **2015**, *3*, 5189.

[290] Y. Huo, J. F. Zhang, K. Dai, Q. Li, J. L. Lv, G. P. Zhu, C. H. Liang, *Appl. Catal., B* **2019**, *241*, 528.

[291] W. L. Yu, D. F. Xu, T. Y. Peng, *J. Mater. Chem. A* **2015**, *3*, 19936.

[292] R. Bhosale, S. Jain, C. P. Vinod, S. Kumar, S. Ogale, *ACS Appl. Mater. Interfaces* **2019**, *11*, 6174.

[293] Y. Wang, Z. Z. Zhang, L. N. Zhang, Z. B. Luo, J. N. Shen, H. X. Lin, J. L. Long, J. C. S. Wu, X. Z. Fu, X. X. Wang, C. Li, *J. Am. Chem. Soc.* **2018**, *140*, 14595.

[294] R. Kuriki, H. Matsunaga, T. Nakashima, K. Wada, A. Yamakata, O. Ishitani, K. Maeda, *J. Am. Chem. Soc.* **2016**, *138*, 5159.

[295] R. Kuriki, M. Yamamoto, K. Higuchi, Y. Yamamoto, M. Akatsuka, D. L. Lu, S. Yagi, T. Yoshida, O. Ishitani, K. Maeda, *Angew. Chem. Int. Ed.* **2017**, *56*, 4867.

[296] Y. Bai, L. Q. Ye, L. Wang, X. Shi, P. Q. Wang, W. Bai, P. K. Wong, *Appl. Catal., B* **2016**, *194*, 98.

[297] M. F. Liang, T. Borjigin, Y. H. Zhang, H. Liu, B. H. Liu, H. Guo, *ACS Appl. Mater. Interfaces* **2018**, *10*, 34123.

[298] Y. Bai, T. Chen, P. Q. Wang, L. Wang, L. Q. Ye, X. Shi, W. Bai, *Sol. Energy Mater. Sol. Cells* **2016**, *157*, 406.

[299] J. S. Wang, C. L. Qin, H. J. Wang, M. N. Chu, A. Zada, X. L. Zhang, J. D. Li, F. Raziq, Y. Qu, L. Q. Jing, *Appl. Catal., B* **2018**, *221*, 459.

[300] R. A. Rather, M. Khan, I. M. C. Lo, *J. Catal.* **2018**, *366*, 28.

[301] W. K. Jo, S. Kumar, S. Eslava, S. Tonda, *Appl. Catal., B* **2018**, *239*, 586.

[302] A. Bafaqeer, M. Tahir, A. A. Khan, N. A. S. Amin, *Ind. Eng. Chem. Res.* **2019**, *58*, 8612.

[303] Y. Yang, J. J. Wu, T. T. Xiao, Z. Tang, J. Y. Shen, H. J. Li, Y. Zhou, Z. G. Zou, *Appl. Catal., B* **2019**, *255*, 117771.

[304] P. Zhou, J. G. Yu, M. Jaroniec, *Adv. Mater.* **2014**, *26*, 4920.

[305] Q. L. Xu, L. Y. Zhang, J. G. Yu, S. Wageh, A. A. Al-Ghamdi, M. Jaroniec, *Mater. Today* **2018**, *21*, 1042.

[306] J. G. Yu, S. H. Wang, J. X. Low, W. Xiao, *Phys. Chem. Chem. Phys.* **2013**, *15*, 16883.

[307] S. Shoji, G. Yin, M. Nishikawa, D. Atarashi, E. Sakai, M. Miyauchi, *Chem. Phys. Lett.* **2016**, *658*, 309.

[308] J. W. Fu, K. Liu, K. X. Jiang, H. J. W. Li, P. An, W. Z. Li, N. Zhang, H. M. Li, X. W. Xu, H. Q. Zhou, D. S. Tang, X. M. Wang, X. Q. Qiu, M. Liu, *Adv. Sci.* **2019**, *6*, 1900796.

[309] X. N. Li, X. F. Yang, J. M. Zhang, Y. Q. Huang, B. Liu, *ACS Catal.* **2019**, *9*, 2521.

[310] A. D. Handoko, F. X. Wei, Jenndy, B. S. Yeo, Z. W. Seh, *Nat. Catal.* **2018**, *1*, 922.

[311] A. U. Pawar, C. W. Kim, M.-T. Nguyen-Le, Y. S. Kang, *ACS Sustainable Chem. Eng.* **2019**, *7*, 7431.

[312] B. Chazallon, C. Pirim, *Chem. Eng. J.* **2018**, *342*, 171.

[313] Y. Yang, S. Ajmal, Y. Q. Feng, K. J. Li, X. Z. Zheng, L. W. Zhang, *Chem. Eur. J.* **2019**, *25*, 1.

[314] J. Gao, H. Zhang, X. Y. Guo, J. S. Luo, S. M. Zakeeruddin, D. Ren, M. Grätzel, *J. Am. Chem. Soc.* **2019**, *141*, 18704.

[315] A. Li, Q. Cao, G. Y. Zhou, B. V. K. J. Schmidt, W. J. Zhu, X. T. Yuan, H. L. Huo, J. L. Gong, M. Antonietti, *Angew. Chem., Int. Ed.* **2019**, *58*, 14549.